RAMAN SCATTERING OF ORGANIC CHARGE TRANSFER COMPOUNDS

Derek Vermeulen

A dissertation submitted to the faculty of the University of North Carolina at Chapel Hill in partial fulfillment of the requirements for the degree of Doctor of Philosophy in the Department of Physics and Astronomy.

Chapel Hill
2015

Approved by:

Laurie E. McNeil

Andrew Moran

Rene Lopez

Kyle Brennaman

Reyco Henning

ABSTRACT

Derek Vermeulen: Raman Scattering of Organic Charge Transfer Compounds
(Under the direction of Laurie E. McNeil)

Understanding the intrinsic nature of charge transport in organic semiconductors is very important in the design of and creation of new organic electronic technology. In particular, charge transfer (CT) compounds offer an interesting sub-species of organic semiconductor, in which one-dimensional transport, ambipolar transport, and the effect of chemical and structural modification can be studied so that one day an organic electronic device can be designed from the molecule up. Electron-phonon (eph) coupling and the degree of charge transfer (ρ) in CT compounds are essential parameters to consider in studying charge transport in OS. Substantial theoretical research has been completed to determine the influence of both non-local and local eph coupling on electronic properties such as charge carrier mobility. However, very few experimental investigations have been completed to test the assertions of theory concerning eph coupling, especially non-local coupling. The aim of this project is to experimentally investigate eph coupling and ρ in organic semiconducting binary CT compounds using Raman spectroscopy, and to compare the results with theoretical calculations where possible.

The first part of this dissertation is focused on the PnT1 (Perylene$_n$-Tetracyanoquinomethane; n=1,2,3) CT compound system consisting of three compounds of differing stoichiometric ratios of perylene to TCNQ. In this project I show that ρ increases as the number of perylenes in the unit cell increases, due to greater electronic coupling resulting from a closer spacing of perylene and TCNQ, which is confirmed by theoretical calculations and X-ray

measurements. I also estimate the local eph coupling constants per phonon of PnT1 using resonance Raman spectroscopy and obtain polaron binding energies of perylene and TCNQ, which are consistent with theoretical calculations.

The last part of this dissertation is focused on anthracene-PMDA (Pyromellitic Dianhydride). Using resonance Raman spectroscopy I apply to this crystalline CT compound a method usually constrained to the study of excited electronic states of molecules in solution. From this technique I am able to extract eph constants, both local and non-local, for inter- and intramolecular phonons and show that both are equally influential in affecting charge transport in organic semiconductors, as predicted by theory.

To my dearest friends and family

ACKNOWLEDGEMENTS

I am extremely indebted to my adviser Dr. Laurie E. McNeil. She has patiently guided me in my graduate career and has taught me how to formulate useful scientific questions to pursue in research. She has been instrumental in me looking more at the big picture of how my research fits into the larger whole. Also, she has been the English and grammar teacher I wish I had growing up by graciously teaching me how to properly communicate in an effective and scientific manner. I am still learning that one. This dissertation would not have happened without her. You are a wonderful mentor and leader Dr. McNeil!

I am also extremely indebted to Dr. Andy Moran. The results from half of this dissertation would not be possible if not for his willingness and selflessness in teaching me about the time dependent resonance Raman spectroscopy model. No matter the question, he was always patient and thorough in answering, even though, I'm sure, he is a very busy man. He graciously gave me the computer program for the model and helped me modify it to apply to the system I was studying. Thank you Dr. Moran!

I have only thanksgiving to give to Dr. Kyle Brennaman. Dr. Brennaman's constant positive attitude and sharp scientific mind has been an amazing help over the years. He selflessly drops his own work, in order to help those around him. Dr. Brennaman was instrumental in helping me develop the method for taking absolute Raman measurements. There were many discouraging times, but Dr. Brennaman was always very encouraging and helpful. You are definitely a city on a hill and a lamp on a stand. Thank you Dr. Brennaman, and strive on brother!

There are many more people that I would like to acknowledge for their influence in the completion of this dissertation, forgive me if you are missed. I am thankful for committee members, Dr. Rene Lopez and Dr. Reyco Henning, whose thoughts and questions on my research have helped me think more deeply on my research and formulate a more developed dissertation. I can never forget my lab mates over the years, Rohan, Zaf, Tyle, Drew (2), Randy and Mary, who were always a great help in the lab and great people to discuss research. Thank you UNC for all of your resources in helping me succeed in my graduate school career.

It is hard to overstate how important my family, close friends, and girlfriend Casey have been to me over my graduate career. The Bible says that we are the body of Christ (1 Cor 12:27). Because of the love that you have showed me over the years, this verse rings loudly in my head as your love has continually pointed me to the bread of life, who famously said ‘For this is the will of my Father, that everyone who looks on the Son and believes in him should have eternal life, and I will raise him up on the last day.’ (ESV John 6:40) Amen.

TABLE OF CONTENTS

LIST OF TABLES

LIST OF FIGURES

LIST OF ABBREVIATIONS

APMDA	Anthracene-Pyromellitic Dianhyride compound
CT	Charge Transfer
DFT	Density Functional Theory
EPH	Electron-Phonon Coupling
HOMO	Highest Occupied Molecular Orbital
LUMO	Lowest Unoccupied Molecular Orbital
PnT1	Perylene$_n$-Tetracyanoquinodimethane compound
PMDA	Pyromellitic Dianhydride

CHAPTER 1: INTRODUCTION

1.1 Overview

Over the next 10 years the organic electronics (OE) industry is forecasted to increase from ~$24 billion globally in 2014 to about $70 billion in the year 2024[1]. Roughly 60% of the current OE market is focused on their use as light emitting diodes (OLEDs) in display and lighting technology. OEs are easier to process, more flexible, and consume less power than inorganic-based electronics[2]. The solubility of organic semiconductors, either small-molecule or polymeric, allows for large-scale and high-volume production on flexible substrates using ink jet or spray coating patterning techniques[3,4]. Furthermore, these patterning techniques make OEs very amenable to cheap roll-to-roll processing[5]. Low processing temperatures (<200 ^{o}C) as compared to silicon-based technology (~300 ^{o}C in amorphous silicon) allow most plastics to be used as substrates[6]. OEs can also be thin; organic thin film transistors (OTFTs) have successfully been printed on micron-thick parylene-C film with a field-effect mobility close to that of amorphous silicon[7]. The charge carrier mobility, which is the average drift velocity of a charge carrier per unit electric field, is a physical property of a material that directly influences device performance; the larger the mobility, the higher the performance for a transistor. There are many organic materials available to create organic semiconductors and their properties are highly tunable via chemical functionalization[8,9]. This is one key advantage of organic semiconductor technology: through chemical functionalization an organic semiconductor can be tailored to fit the needs of the application. These properties make OEs a very versatile and exciting area of fundamental research with many novel applications such as solid state lighting, photovoltaics,

thin film batteries, sensors[10], electronic paper, foldable displays[11], RFID tags[12], and electronic textiles.

The highest mobility reported to date of an OFET was that of a small molecule-polymer blend of C8 (2,7-dioxtyl[1]benzothieno[3,2,b][1]benzothiophene) and polystyrene with a maximum hole mobility of 43 $cm^2V^{-1}s^{-1}$ and an average of 25 $cm^2V^{-1}s^{-1}$ [13]. Prior to this measurement, p-type single-crystal rubrene held the record with a room temperature mobility of 20 $cm^2V^{-1}s^{-1}$ [14,15], which is on par with that of polysilicon[16], but much lower than that of pure crystalline silicon (~1400 $cm^2V^{-1}s^{-1}$ [electron], ~450 $cm^2V^{-1}s^{-1}$ [hole])[17,18]. In real-world applications, amorphous or polycrystalline organic polymeric or small-molecular solution-processed thin films are preferred, due to ease of processability and mechanical flexibility. Recently, donor-acceptor (D-A) polymers based on DPP (diketopyrrolopyrrole) and PCDTPT (poly[4-(4,4-dihexadecyl-4H-cyclopenta[1,2-b:5,4-b']dithiophen-2-yl)-alt-[1,2,5] thiadiazolo[3,4-c]pyridine]) have reached hole mobilities of 10 $cm^2V^{-1}s^{-1}$ [19] and 20 $cm^2V^{-1}s^{-1}$ [20], respectively. The goal of current organic-semiconductor-based device research is to reach or exceed the performance characteristics of standard polysilicon thin film transistors. Achieving this goal will greatly increase the value and desirability of using organic-semiconductor-based devices due to their low cost and flexible mechanical properties compared to inorganic–semiconductor-based devices. For instance, one lucrative application would be in replacing silicon as the active element in active-matrix thin-film transistor backplane display technology.[21] Understanding charge transport at the intrinsic level will be vital in unlocking the potential of organic semiconductor technology. This idea is aligned with the core of the overarching goal of this project, which is to explore the physical properties of organic semiconductors, such as the interaction of charge carriers with their environment, in order to identify the most-promising

organic semiconductors for use in transistors, LEDs, and solar cells, and other electronic devices.

In recent years there has been increased interest in organic charge transfer (CT) compounds due to their potential use in high-mobility OEs. A CT compound, composed of stacks of alternating electron-donating and -accepting small molecules, is an ideal platform for intrinsic charge transport studies in which intentional changes in molecular or crystal structure can cause large changes in charge transport. The interaction of charge carriers with phonons is very important in organic semiconductors, in which electron-phonon (eph) coupling energies are on the same order of magnitude as the electronic bandwidth (electronic coupling). Eph coupling, a type of dynamical disorder, tends to localize charge carrier wavefunctions and thereby reduce charge carrier mobility; however there are cases of phonon-mediated transport[22,23] in which the mobility is enhanced by eph coupling. The effect of eph coupling on charge transport is an important research area. Recently, much theoretical research using density functional theory (DFT)[24–28] has been completed, but experimental research is still needed to verify the values of microscopic parameters derived from the DFT results. In short, both electronic and eph coupling are functions of the crystal structure and this dissertation will experimentally determine their magnitudes with Raman spectroscopy and compare with theoretical values. Raman spectroscopy and its variant Resonance Raman Spectroscopy (RRS) are powerful tools for probing electronic and electron-phonon coupling in CT compounds. In the subsequent sections of the introduction, a basic overview of organic semiconductors and their optical, electronic, and charge transport properties is presented. In chapter two, the materials used in this project are presented with a discussion on any prior research that has been conducted on them. Chapter 3 presents the experimental techniques used to extract the charge transport coupling constants. The study of the Perylene$_n$-TCNQ (Tetracyanoquinodimethane) CT compound system is presented in chapter 4

and the Anthracene-PMDA (Pyromellitic Dianhydride) CT compound in chapter 5. Finally, chapter 6 concludes with a synopsis of this project and discussion of its main results.

1.3 Polymers

Organic semiconductors fall into two major categories, polymer- and small-molecule-based. The two classes can be blended to obtain solution-processed OTFTs with a mobility as high as 5 $cm^2V^{-1}s^{-1}$ [29]. This dissertation is focused on small-molecule-based charge transfer semiconducting crystals, but polymer-based materials will be mentioned here briefly for completeness and comparison. Since the Nobel Prize-winning discovery of conductive polymers of doped polyacetylene in 1977[30], extensive research has been conducted on polymers for their use in electronic and optoelectronic devices. Semiconducting polymeric materials are composed of collections of π-conjugated polymeric chains; charge transport occurs along the chains as well as between neighboring chains via π –π overlap. The most successful classes in terms of high mobility are pictured in Figure 1.1, these are polythiophenes, polyfluorenes, and donor-acceptor based copolymers such as those based on DPP.[31]

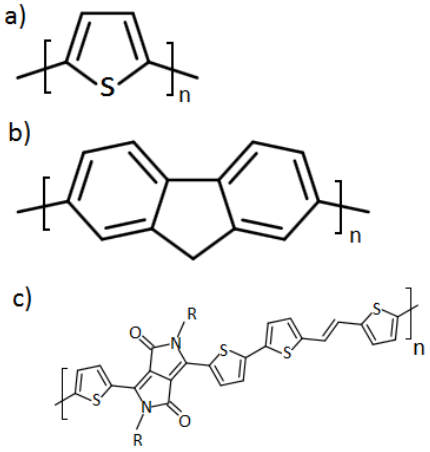

Figure 1.1: Representative polymers a) polythiophene b) polyfluroene c) DPP based.

In comparing polymeric-based and small-molecule-based organic semiconductor technology there is no *a priori* reason to choose one over the other as the choice would depend on the device application. Solution processing of polymer films for TFTs is in general more successful than for small-molecule films. Polymeric films are more smooth and uniform because there is more control over the rheological properties of the deposited solution, resulting in less device-to-device variation.[32,33,34] However, solution processing of small molecular films has been improved recently by using small molecules that have many conjugation units and suitable alkyl substitutions for more uniform solution deposition[35,36] and with the use of spin[37], slot-die coating[38], or continuous edge casting[39] techniques. In addition, small-molecule OSCs tend to have higher open-circuit voltages[40,41] and less batch-to-batch variation[42]. Polymer-based OLEDs have simpler device architecture than do those made from small molecules[43], but they do not perform as well.[44] The remainder of the dissertation will be concerned solely with small-molecule-based semiconductors.

1.4 Small molecule

1.4.1 Monomolecular

Small-molecule monomolecular organic semiconductors are materials composed of small organic molecules held together by attractive weak van der Waals forces. A few examples are pictured in Figure 1.2.

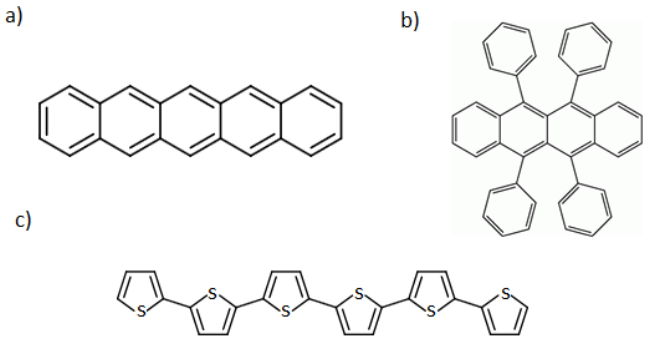

Figure 1.2: Representative small molecules a) pentacene and b) rubrene of the oligoacene family and c) hexathiophene of the oligothiophene family.

Oligoacene-based semiconductors and their derivatives have by far been the most successful in creating high mobility OFETs, with pentacene and rubrene as the forerunners. Since this project is focused on the intrinsic properties of organic semiconductors, only the crystalline phase will be considered. Numerous monographs[45,46] and reviews[47,48] on the subject are available, so only some general qualities of small-molecule semiconducting crystals will be presented here. Small molecules are defined as having masses less than 900 daltons[49]; those relevant to this project are composed of aromatic π-conjugated rings arranged in different patterns. As in polymers, in small molecules charge transport occurs via π-π orbital overlap from the sp^2 hybridized carbon atoms. In such systems the character of the molecule is largely retained in the solid state due to the weak intermolecular van der Waals interactions, which also gives them their mechanical flexibility. The van der Waals nature of intermolecular interactions stems from a composite of sources, namely, London dispersion forces[50], induction forces[51], and multipole-multipole interactions[51]. As a whole, these forces exhibit a distance dependence of $\sim r^{-6}$, compared to a $\sim r^{-2}$ coulombic dependence. The weakness of these forces is one of the defining qualities of molecular crystals and is made manifest in their optical and electronic properties. For instance, in UV-Vis absorption spectra of molecular crystals, local electronic molecular interactions are only shifted

in energy compared to their values in the free molecule due to solid state interaction, leaving their molecular character largely intact.[52] As a result, molecular properties such as the ionization potential, electron affinity, electronic structure, and polarizability are very important in determining the properties of molecular crystals. In the solid state, most molecular crystals are insulating or semiconducting and tend to be low in symmetry and optically biaxial. The low symmetry and planar nature of the small molecules relevant to this project create structures with very anisotropic electrical and optical properties[53,54]. Furthermore, small-molecule crystals have low dielectric constants: $\varepsilon \sim 3\text{-}6$[45,47,48], as compared to silicon with $\varepsilon = 11.9$[55]. For materials with a low dielectric constant, charge carriers will be more prone to localization around counter-ions due to lower electric-field screening (dielectric screening). Thus, in order to properly account for the optical and electrical characteristics of molecular crystals, polarization effects from the lattice, the molecular vibrations, and the valence and conduction electrons and holes are required.[56] Another consequence of the low dielectric constant is that the exciton (bound electron-hole pair) binding energy is high, ranging between ~0.5-1.0 eV[47,48]. A typical electronic energy level scheme for a molecular crystal system is shown in Figure 1.3.

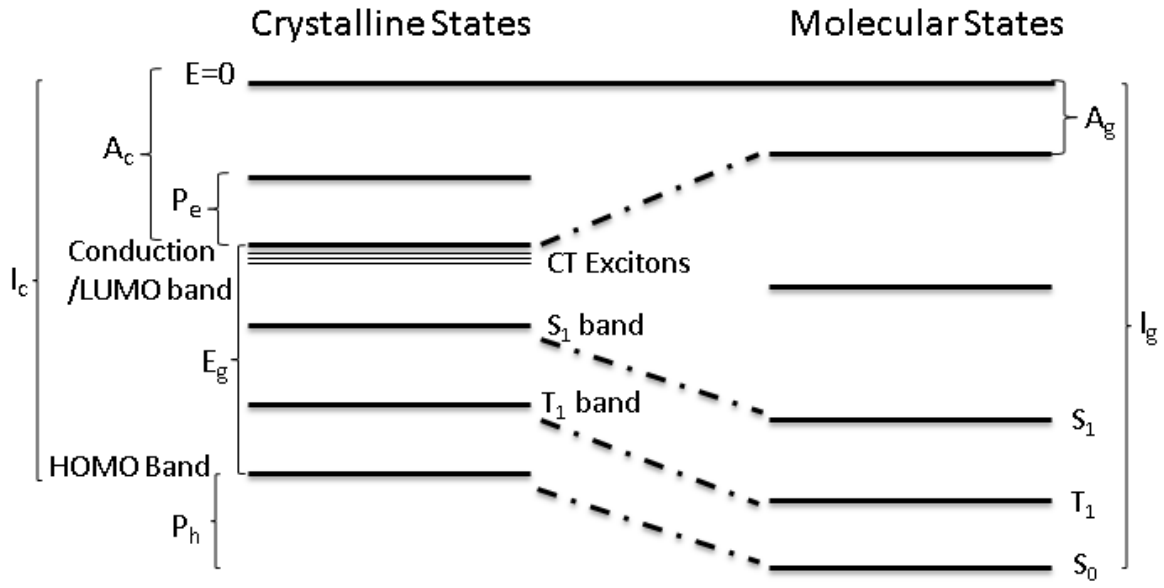

Figure 1.3: Molecular crystal energy level scheme: Symbols; A_g, A_c: Gas and crystal phase electron affinity; I_g, I_c: Gas and crystal phase ionization potential; E_g: band gap energy; P_e, P_h: Electron and hole polarization energy; S_0, S_1, T_1: Singlet and triplet states. Adapted from ref.[57]

Band gaps in molecular crystals typically range between 2-5 eV[46]. The weak van der Waals interaction between molecules implies narrow conduction and valence bands of widths less than or equal to 500 meV[48]. In anthracene for instance[46], the polarization energy contribution due to lattice and molecular phonons is nearly 300 meV, therefore electron-phonon coupling is needed to properly describe charge transport in molecular crystals. In oligoacene-type crystals the timescale of molecular relaxation is faster than that of the charge carrier hopping time, meaning that charge transport in these materials is polaronic in nature and thermally activated around room temeprature.[51] In polaronic transport, the molecule, and in some cases the lattice, has time to relax around the charge carrier before it proceeds to the next electronically-coupled molecule. A polaron is then a quasi-particle composed of a charge carrier and its accompanying molecular and lattice polarization moving in a potential well whose depth is called E_{pol}, the polaron binding

energy. This is not yet a complete description of the charge transport, however, as will be shown in section 1.5.

1.4.2 Charge transfer compounds/bimolecular organic semiconductors

The measurement of the high hole mobility of single-crystal rubrene was completed in 2004[15]. Since then, there has been only one measurement of a small-molecular organic semiconductor with a higher mobility: 25 $cm^2V^{-1}s^{-1}$ in a dioctyl-benzothiophene derivative[13]. A transition to materials with more than one molecular species is a logical next step in discovering the possibility of higher-mobility organic materials. Charge transfer (CT) compounds are unique in that they exhibit a wide range of physical properties due to their chemical and physical structure, for example, superconductivity[58], ferroelectricity, quasi-one dimensional transport, neutral-ionic transitions[59], and semi-conduction. Semiconducting CT compounds have garnered more attention recently due to their potential as active elements in ambipolar OFETs[60–63] and the prediction of low effective hole and electron masses[64,65]. Ambipolar transistors would reduce the cost of creating complementary-like inverters in CMOS (complementary metal oxide semiconductor) logic integrated circuits[66], among other advantages. Also, source and drain contacts made from the CT compound TTF-TCNQ (Tetrathiafulvalene-Tetracyanoquiondimethane) have been shown to improve n-type mobility by nearly an order of magnitude in single crystal DBTTF (Dibenzotetrathiafulvalene)-TCNQ OFETs, to 1 $cm^2V^{-1}s^{-1}$[67–70].

At its most basic level, a CT compound is a material with an electron-donating and an electron-accepting chemical or atomic species in any stoichiometric ratio. This study considers CT compounds composed of planar polycyclic aromatic π-conjugated oligoacene donors and acceptors. Charge transfer compounds have been studied for many years, with Mulliken laying

the theoretical groundwork for the material system in the early 1960s[71]. It was not until the discovery of metallic conductivity, a metal-insulator transition, and a charge density wave (CDW) in TTF-TCNQ in the 1970s that interest in CT compounds became greatly enhanced[72–74]. Unlike monomolecular organic compounds, CT compounds have an additional stabilizing interaction in the ground state called the CT interaction. Mulliken showed that the CT interaction strength is at a maximum when the overlap between donor and acceptor wavefunctions (HOMO/LUMO overlap) is maximized and the difference between the ionization potential (IP) of the donor and electron affinity (EA) of the acceptor is small. This type of electronic coupling is known as the transfer integral, t. The ground state wavefunction is now a superposition of neutral and CT wavefunctions resulting in the possibility of a partially-ionic ground state or intermediate degree of CT, ρ, whose value depends on IP, EA, and t. Having $\rho \sim 0$ means that there is no CT between the donor and acceptor molecule in the ground state, where $\rho \sim 1$ means that there is full CT between donor and acceptor so that the ground state is fully ionic. In strong CT compounds the lowest excited state is the CT state rather than a local molecular excitation. The CT state is an excitonic state in which an electron from the donor molecule has been transferred to the acceptor molecule.

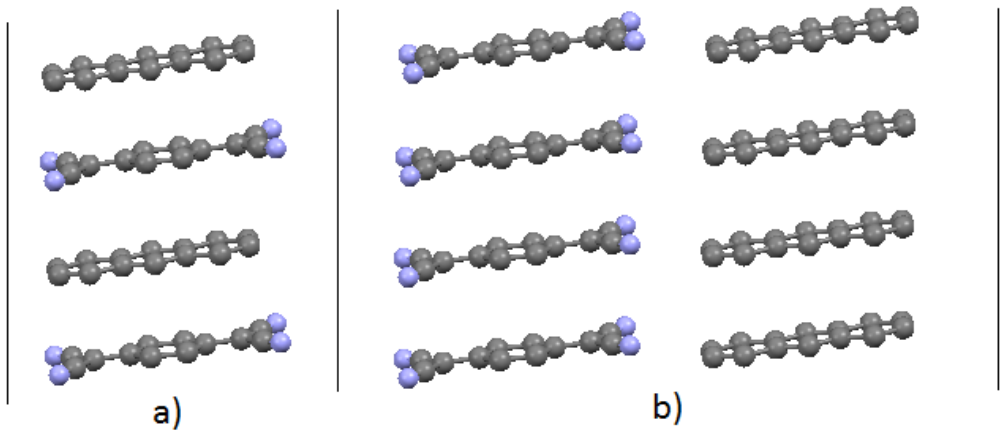

Figure 1.4: Idealized representations of a) mixed stack and b) segregated stack CT compounds.

CT compounds come in a variety of stacking arrangements as shown in Figure 1.4. Compounds that have a constant spacing between adjacent molecules are called regular stacked and compounds that alternate in distance between adjacent molecules are called dimerized stacked. Regular segregated stack (SS) CT compounds tend to be organic conductors, regular mixed stack (MS) CT compounds tend to be insulating or semiconducting[75], and dimerized SS and MS CT compounds are insulating with a CDW[76]. The electronic and optical properties of CT compounds are very sensitive to CT transitions and the parameters that define them, such as the transfer integral (t), ionization potential (IP) of the donor, electron affinity (EA) of the acceptor, and the degree of charge transfer (ρ), to name a few. Torrance[61,63] in studying TCNQ-based acceptor CT compounds discovered that when the difference in energy between the IP and EA of the donor and acceptor was similar to the Madelung energy (E_m) of the lattice, TCNQ-based CT compounds had metallic-like conductivity, were regular SS in structure, and had intermediate ρ (~0.5). If E_m was greater than the IP-EA difference, the compound was semiconducting, had a regular MS structure, and was either quasi-neutral (<0.4), or quasi-ionic (>0.6), however some intermediate regular MS cases exist, including TTF-Chloranil (ρ~0.6)[79] and TMD-TCNQ (ρ~0.6)[80]. Conversely, if the IP-EA difference was greater than E_m, the compound was ionic in

the ground state. This is what is known as the neutral-ionic boundary. Temperature and pressure both have a profound impact on ρ due to the large thermal expansion and high compressibility of these solids. In another study by Torrance[59], his group discovered that by applying pressure to neutral CT compounds close to the neutral-ionic boundary, a neutral-to-ionic transition was observed in over 10 CT compounds based on electron acceptors such as TCNQ, chloranil, and fluoranil. In addition, they observed that the pressure at the onset of the transition was proportional to the CT transition energy: higher pressure was needed to see the transition for compounds with higher-energy CT transitions. These observations demonstrate the tunable nature of CT compounds and identify some of the most important parameters in determining optical and electronic properties.

1.4.3 Spectroscopic effects in CT compounds

Spectroscopic effects due to CT interactions manifest themselves in electronic absorption and reflection spectra. CT compounds, both MS and SS, have a unique electronic fingerprint consisting of a low-energy CT transition with higher-energy molecular exciton transitions[81]. As mentioned earlier, the energy of the CT transition is dependent on the difference IP - EA of the donor and acceptor molecules and also on the transfer integral. In addition, the CT transition is highly anisotropic and is polarized mainly along the stacking axis of the donor and acceptor molecules. Overlaying the electronic spectra of CT compounds with the electronic spectra of their neutral donor or acceptor parent molecular crystals further reveals the van der Waals nature of these materials as seen in Figure 1.5.

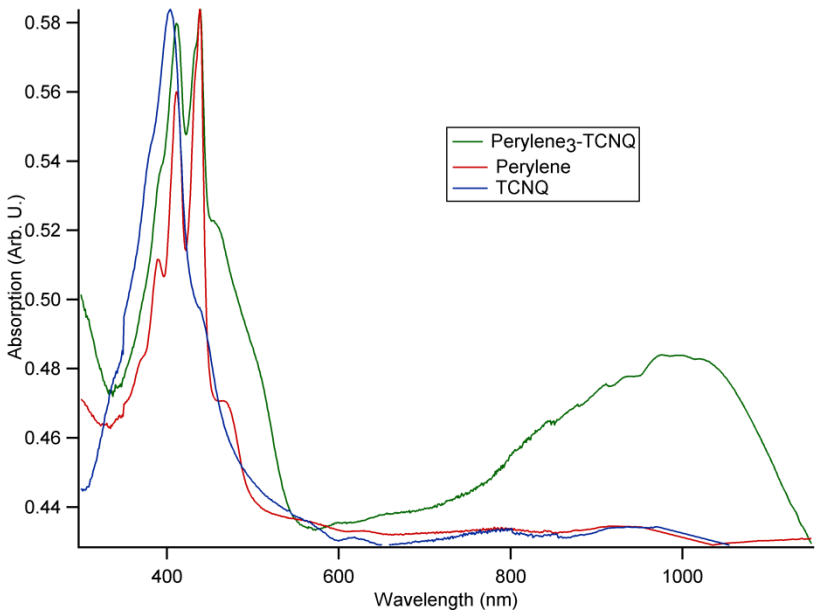

Figure 1.5: Absorption spectra of Perylene$_3$-TCNQ (Tetracyanoquinodimethane), perylene, and TCNQ. Data taken as described in section 3.7.2.

The CT spectrum is a superposition of the spectra of the parent molecules with slight shifts in local molecular exciton energies and with the additional lower-energy CT transition. It becomes apparent from this picture that a clear separation between internal (local) and external (non-local) electronic phenomena will also manifest itself in other physical properties of the material. In fact, the vibrational spectra of CT compounds and monomolecular crystals are separated into an external and internal regime. Low-frequency (<200 cm^{-1}) phonons are generally intermolecular in nature, where higher-frequency phonons are intramolecular. In the ground state, charge-sensitive intramolecular phonons are shifted from their neutral-state frequency according to the degree of CT, ρ [82–86]. The average charge on the molecule affects the equilibrium positions of the atoms and results in new bond lengths and angles, which therefore changes the frequencies of the intramolecular phonons from those when no excess charge is present. Since the excess charge is not distributed uniformly over the molecule, each phonon will shift in frequency by a different amount, or not at all. By comparing the phonon frequencies of

the CT compound with those of the neutral and ionized molecule an estimate of ρ can be made.[82,84] In general, only phonons with large frequency shifts are chosen for the determination of ρ in to order minimize any error resulting from frequency shifts due to changes in solid state environment, which are usually on the order of a few wavenumbers[87] for molecular crystals. The estimate can be made using either Raman-active or IR-active phonons. Depending on the structure of the CT compound (e.g. dimerized, regular, SS, MS), one type of spectroscopy may provide a more-accurate value than the other because of coupling of the phonon with CT electrons[88–90]. A linear relation between phonon frequency and ρ is usually assumed. This assumption has been experimentally[84,85] and theoretically[91] explored in TCNQ-based CT compounds and found to be sound. Additionally, ρ can be determined with other methods like X-ray diffraction[92,93] and diffuse X-ray scattering[94] and there is good agreement with values determined by vibrational spectroscopy.

Another factor in addition to ρ that can perturb the ground state intramolecular frequencies of the donor and acceptor species is the coupling of intramolecular phonons with the CT transition[87–89,95], i.e. electron-phonon (eph) coupling. This type of coupling stems from the modulation of the site energy, which is related to the IP and EA of the donor and acceptor, respectively, by an intramolecular phonon. In his seminal work, Rice showed that unknown IR absorptions polarized along the molecular stacking axis were actually perturbed Raman-active phonons that had coupled to the CT transition in dimerized SS ion-radical TCNQ systems [96]. He also showed that these phonons borrowed intensity from the CT transition and the strength of the vibronic enhancement was related to the frequency of the CT transition.[97] In MS CT compounds, which this project focuses on, such vibronic effects due to eph coupling with the CT transition are possible, but their behavior is expressed in different ways. As in SS CT compounds, only

fully-symmetric (A_g) intramolecular phonons will couple to a non-degenerate electronic CT state and have non-zero eph coupling constants.[98,99] Prior studies have shown[79,89,95,100] that in regular MS CT compounds the frequencies of the Raman-active A_g phonons are perturbed by eph coupling with the CT-transition. Furthermore, as observed in the MS phase of TTF-CA (chloranil) (ρ=0.65)[100], Raman-active A_g phonons can even show up as vibronic absorptions in IR spectra, as in SS dimerized CT compounds, at frequencies coincident with those observed in the Raman spectra. The amount of perturbation of the Raman frequencies and strength of the vibronic absorptions is related to the value of ρ; reaching a maximum at ρ=0.5[90]. This means that in quasi-neutral (ρ<0.1) MS CT compounds A_g Raman-active phonons will be minimally perturbed by the eph coupling with the CT transition and that there will be no visible vibronic absorptions in the IR spectra.

Measurements of resonance Raman spectra of the CT transition in CT compounds are rare. One reason for this is that many of the more interesting CT compounds near the neutral-ionic boundary have their CT transitions at energies less than 1.5 eV, meaning NIR to IR optics and lasers are required to complete the experiment. Despite this, there have been some resonance studies on dimerized SS TTF (Tetrathiafulvalen) radical ion salts[101–103]. This system can be modeled well with a two-site 1-dimensional Peierls-Hubbard Hamilitonian. In this limit, explicit expressions for the inclusion of both local and non-local eph coupling can be obtained. It was found that there was a selective enhancement of the scattering cross section of intermolecular phonons when the compound was excited with light of energy coincident with the CT transition. This selective effect was explained in terms of the Peierls-Hubbard Hamilitonian. When the non-local Hamiltonian is written in terms of the eigenstates of the electronic Hamiltonian it becomes clear that only intermolecular phonons will be enhanced. Using this theoretical model, non-local

eph coupling constants were obtained for the lowest translational optical intermolecular phonons of the TTF dimeric system. However, resonance Raman of MS CT compounds to explore eph coupling appears not to have been pursued by other researchers. In conclusion, microscopic effects, such as eph coupling, electronic coupling, and the degree of CT all have an effect on the optical spectra of CT compounds. Understanding how these effects influence the optical spectra are important in ultimately understanding charge transport in CT compounds.

1.5 Charge transport in organic semiconductors and CT compounds

1.5.1 Overview

As mentioned earlier, there are many factors that can affect charge transport in organic semiconductors such as molecular packing, static and dynamical disorder, chemical structure, charge carrier density[104], and impurities. In a perfect molecular crystal without phonons, disorder, or impurities, a charge carrier is described as a plane wave (Bloch state) delocalized over the expanse of the crystal, much like in an inorganic semiconductor (e.g. silicon, germanium). Introducing any change from perfect periodicity will localize the electronic wave function and narrow the conduction and valence bands. For instance, it has been shown[105] that high-purity pentacene single crystals exhibit an increase in charge carrier mobility compared to less-pure crystals, to nearly 35 $cm^2V^{-1}s^{-1}$, due to the removal of traps caused by chemical impurities. Also, in anthracene crystals, doping with tetracene at just 1 ppm drastically lowered the hole mobility from ~10^0 to 10^{-1} $cm^2V^{-1}s^{-1}$ [106]. These measurements justify the need for pure single crystals in order to study intrinsic charge transport. As deviation from perfect crystalline disorder increases, the mean free path of a charge carrier decreases and scattering increases. At a certain limit of disorder, the charge carrier is localized on a molecular site and charge carrier motion is best described as a series of uncorrelated hops from one molecular site to the next.

These are the two extremes of charge transport. When disorder is small and electronic coupling is high, band-like transport is an appropriate charge transport description, and in the opposite case hopping or polaronic transport is more accurate. An uncertainty type of relationship holds for the criterion that determines what type of limiting transport case is expected[57]

$$\tau \gg \frac{\hbar}{W}\text{; band transport} \qquad \tau \ll \frac{\hbar}{W}\text{; hopping transport} \tag{1.1}$$

In equation 1.1, τ is the mean scattering time of the charge carrier and W is the bandwidth of a conduction or valence band. In a real molecular crystal such as a CT compound the charge transport is typically in between these two regimes. Temperature-dependent measurements of charge carrier mobility in single crystals are used to compare with charge transport models in order to identify which type of limiting case is a more appropriate description. Even within one material a charge carrier can be described by different models due to structural anisotropy in molecular crystals. For instance, transport along one crystal direction by one charge carrier type may be band-like, whereas in another direction and with another charge carrier type it may be hopping-like in nature. In general the temperature dependence of band and hopping transport is

$$\mu_{band}\, \alpha\, T^{-n}\,; n = \pm 0 \rightarrow 3\,; \qquad \mu_{hopping}\, \alpha\, T^{-n} exp\left[\frac{E_{pol}}{k_b T}\right]; n \approx 1 \tag{1.2}$$

In equation 1.2, E_{pol} is the polaron binding energy, as described in section 1.5.4. As an example of the insufficiency of either description to fully describe a material, naphthalene exhibits both charge transport descriptions depending on the unit-cell direction and charge carrier. For example, naphthalene exhibits band-like hole mobility along each principal crystal axis, but the electron mobility along the c' direction displays a band-to–hopping-like transition at 100K[53]. In many cases, neither model fully explains the observed transport trends across the full temperature range.[107] As yet there is no fully general model for charge transport in organic

semiconductors. The temperature dependence of the mobility cannot be described by a purely band-like model, but must be augmented with polaronic effects[25,108]. In lieu of this, charge transport is usually approximated as the sum of two contributions, coherent (band-like) and incoherent (hopping) electron transfer as shown in equation 1.3.

$$\mu_{Total} = \mu_{band} + \mu_{hop} \tag{1.3}$$

Which contribution dominates depends on a number of microscopic parameters, such as electron-phonon coupling, the transfer integral, ionization potential and electron affinity of the donor and acceptor molecules, and phonon energies. In general, the larger the transfer integral (electronic coupling), the larger the bandwidth of the conduction or valence bands of the CT compound and ideally the larger the mobility. The value of the transfer integral depends on the orbital overlap of the two adjacent molecular sites, as well as the energy difference between them. Electron-phonon coupling comes in two varieties, non-local and local. Local coupling is a result of a modulation of the molecular site energies, mainly by intramolecular phonons, whereas non-local coupling is the modulation of the transfer integrals, mainly by intermolecular phonons. Local coupling tends to decrease the mobility by increasing the polaron binding energy. Non-local coupling has a dual effect in that it can decrease the mobility or else increase it as in the case of phonon mediated transport[22,23]. The reader interested in a theoretical treatment of charge transport with a description of the relevant microscopic parameters is recommended to read the rest of this chapter.

1.5.2 The vibronic Hamiltonian

Much of the ground work in our current theoretical understanding of charge transport in molecular-based organic semiconductors was laid out with Holstein's polaron theory of transport in molecular crystals in 1959.[109,110] He described what is now called a local model, in which a

charge carrier interacts solely with molecular phonons. In his model the energy of the charge carrier was lowered by an amount called the polaron binding energy, whose magnitude depends on the strength of the electron-phonon coupling. In sufficiently narrow-band molecular crystals this model is an appropriate description for charge transport. Following his approach, a one-electron tight-binding model helps elucidate the effect that parameters such as electron-phonon coupling and bandwidth have on charge transport, as can be seen in the following equations for the total energy of the organic semiconductor system[45,111].

$$\hat{H} = \hat{H}_E + \hat{H}_P + \hat{H}_{\varepsilon-P} + \hat{H}_{t-P} + \hat{H}_{Dis} \tag{1.4}$$

In equation 1.4, H_E represents the electronic Hamiltonian, H_P is the vibrational Hamiltonian, $H_{\varepsilon\text{-}p}$ is the local electron-phonon coupling Hamiltonian, $H_{t\text{-}P}$ is the non-local electron-phonon coupling Hamiltonian, and H_{Dis} represents the static disorder Hamiltonian.

$$\hat{H}_E = \sum_n \varepsilon_n a_n^+ a_n - \sum_{n \neq m} t_{nm} a_m^+ a_n \,; \qquad \hat{H}_P = \sum_\alpha \hbar\omega_\alpha (b_\alpha^+ b_\alpha + \frac{1}{2}) \tag{1.5}$$

In the preceding equation, H_E consists of ε_n, the site energy of the nth site and t_{nm}, the transfer integral between molecular sites n and m; spin is implicit in these sums. The operators a_n^+ (a_n) and b_α^+(b_α) represent the creation (annihilation) operators of an electron on site n or a phonon of branch α of frequency ω_α.

$$\varepsilon_n = \varepsilon_n^0 + \sum_\alpha \left(\frac{\partial \varepsilon_n}{\partial Q_\alpha}\right)_0 Q_\alpha + \cdots; \quad t_{nm} = t_{nm}^0 + \sum_\alpha \left(\frac{\partial t_{nm}}{\partial Q_\alpha}\right)_0 Q_\alpha + \cdots; \tag{1.6}$$

The site energy and the transfer integrals are both modulated by intramolecular and intermolecular phonons and can be expanded in dimensionless normal coordinates, Q_α. This expansion can be plugged into the electronic Hamiltonian to produce the electron-phonon coupling Hamiltonians.

$$\widehat{H}_{\epsilon-P} = \sum_{\alpha,n} \hbar\omega_\alpha g_{\alpha,n} a_n^+ a_n (b_\alpha^+ + b_\alpha)\,;\; g_{\alpha,n} = \frac{1}{\sqrt{2}}\left(\frac{\partial \varepsilon_n}{\partial Q_\alpha}\right)_0 ; Q_\alpha = \frac{1}{\sqrt{2}}(b_\alpha^+ + b_\alpha); \tag{1.7}$$

In $H_{\varepsilon\text{-}P}$, the local electron phonon coupling Hamiltonian, $g_{\alpha,n}$ is the local coupling constant of phonon α at site n.

$$\widehat{H}_{t-P} = \sum_{\alpha,n,m} \hbar\omega_\alpha f_{\alpha,nm} a_n^+ a_m (b_\alpha^+ + b_\alpha)\,;\; f_{\alpha,nm} = \frac{1}{\sqrt{2}}\left(\frac{\partial t_{nm}}{\partial Q_\alpha}\right)_0 ; \tag{1.8}$$

In $H_{t\text{-}P}$, the non-local electron phonon coupling Hamiltonian, $f_{\alpha,nm}$ is the non-local coupling constant of phonon α between sites n and m.

$$\widehat{H}_{Dis} = \sum_n \delta\varepsilon_n a_n^+ a_n + \sum_{n\neq m} \delta t_{nm} a_n^+ a_m \tag{1.9}$$

Finally, H_{Dis} represents any effect due to static disorder that would create a distribution of site energies or transfer integrals. Equations 1.4-1.9 in their totality cannot be solved analytically to find the ground state energy. Furthermore, with a typical CT compound having as many as 40-100 atoms per unit cell the calculation quickly becomes intractable. Application of a few simple approximations, such as accounting for only nearest-neighbor interactions that involve only the HOMO (highest occupied molecular orbital) and LUMO (lowest unoccupied molecular orbital) orbitals allows the site energy and the transfer integral to be easily defined as in equation 1.10.[112]

$$\varepsilon_n = \int \varphi_n^* H \varphi_n \, dr\,; \quad t_{nm} = -\int \varphi_n^* H \varphi_m dr; \tag{1.10}$$

This type of approach has been used widely in the small-molecule-crystal field of research. For instance, Hubbard applied a similar Hamiltonian (eq. 1.5) to describe the interaction of electrons in narrow conduction bands[113] and in the CT compound TTF-TCNQ, where transport in only one dimension was assumed, in order to describe the observed spectroscopic effects[56]. In fact,

transport in many CT compounds can be considered quasi-one-dimensional due to the formation of these compounds into molecular isolated stacks[114–116]. In order to gain microscopic insight into the factors that govern charge transport, a few limiting cases in the application of the vibronic Hamiltonian of equations 1.4-9 will be discussed.

1.5.3 The transfer integral and band-like transport

The transfer integral quantifies donor-acceptor electronic coupling. In the tight binding model presented thus far, the transfer integral is defined as the overlap between the frontier (HOMO/LUMO) molecular orbitals of adjacent molecular sites. In CT compounds, the overlap is between the HOMO of the donor and the LUMO of the adjacent acceptor molecule, whereas in monomolecular solids the overlap is between adjacent HOMO (LUMO) levels for hole (electron) transport. Considering only the electronic Hamiltonian, H_E, equation 1.5, and the one-dimensional row of evenly-spaced identical sites (e.g. only LUMO levels) shown in Figure 6, the Hamiltonian can be diagonalized via a Fourier transform into momentum space, k, to give the following electronic energy for an electron (hole)in a conduction (valence) band.

$$E(k) = \varepsilon - 2tcos(ka) \tag{1.11}$$

From equation 1.11, it becomes clear that the physical interpretation of the transfer integral is related to the conduction (valence) bandwidth, in this case defined as 4*t. Eigenstates of this Hamiltonian are plane wave (Bloch) states of quantized momentum delocalized over the expanse of the material.

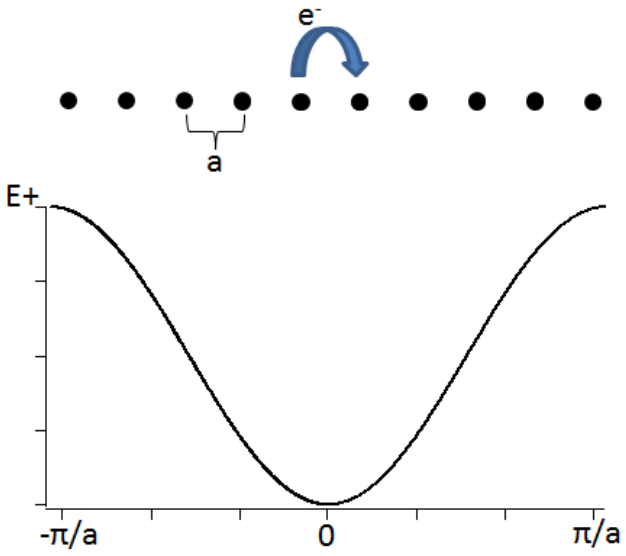

Figure 1.6: Electronic structure of a one dimensional crystal with no phonons and site spacing a.

The charge carrier effective mass is related to the curvature of the band; see equation 1.12.

$$m_{ij}^{*} = \pm\hbar^{2}\left(\frac{\partial^{2}E}{\partial k_{i}\partial k_{j}}\right)^{-1}\text{; (+) for electrons, (-) for holes} \tag{1.12}$$

In equation 1.12, the indices i and j correspond to different dimensions in reciprocal space. Applying equation 1.12 to the electronic energy of equation 1.11 gives the effective mass for this system.

$$m^{*}(k) = \frac{\hbar^{2}}{2ta^{2}\cos(ka)} \tag{1.13}$$

The mobility in a band-like system is related to the effective mass by equation 1.14.[117]

$$\mu = \frac{e\tau}{m^{*}};\ \tau = relaxation\ time \tag{1.14}$$

From this simple derivation of a one dimensional chain of identical molecular orbitals, the transfer integral is shown to have a large impact on electronic structure and transport. Namely, assuming all other parameters are held constant, the larger the transfer integral, the larger the

bandwidth and the higher the charge carrier mobility. Increasing HOMO/LUMO π-orbital overlap between neighboring molecules is essential to maximizing charge carrier mobility in organic semiconductors. Typical values of the transfer integral for the valence bands of traditional inorganic semiconductors, e.g. silicon and germanium, are on the order of a few eV[118–120]. In contrast, hole transfer integrals for typical organic semiconductors are 42 meV[27]in pentacene , 100 meV in rubrene[121], and 85 meV for the CT compound DBTTF-TCNQ[64]. The substantially lower values are direct consequence of the inherently weaker van der Waals forces binding the material together as compared to the covalent bonds found in inorganic semiconductors.

1.5.4 Holstein local polaron model: local eph coupling

The next limiting case is the model of Holstein's[109,110] in his work on a linear chain of diatomic molecules. In this model, the transfer integral and non-local coupling constant, $f_{\alpha,mn}$, are set to zero and only the site energy and local coupling constant, $g_{\alpha,n}$, are considered. The resulting Hamiltonian is then

$$H_{Holstein} = \sum_n \varepsilon_n a_n^+ a_n + \sum_\alpha \hbar\omega_\alpha (b_\alpha^+ b_\alpha + \frac{1}{2}) + \sum_{\alpha,n} \hbar\omega_\alpha g_{\alpha,n} a_n^+ a_n (b_\alpha^+ + b_\alpha) \qquad (1.15)$$

$H_{Holstein}$ can be diagonalized by a canonical transformation[122,123] to give the following energy eigenvalues considering only one electronic orbital per site.

$$E_n = \varepsilon_n + \sum_\alpha \hbar\omega_\alpha (b_\alpha^+ b_\alpha + \frac{1}{2}) - \sum_\alpha g_{\alpha,n}^2 \hbar\omega_\alpha \qquad (1.16)$$

The effect of local electron-phonon coupling is to lower the electronic energy by the third term of equation 1.16. This term is called the polaron binding energy, E_{pol}.

$$E_{pol} = \sum_{\alpha} g_{\alpha,n}^2 \, \hbar\omega_{\alpha} \tag{1.17}$$

Both intermolecular and intramolecular phonons can potentially contribute to E_{pol}. Physically, the coupling constants, $g_{\alpha,n}$, originate from changes in the positions of atoms in the molecule or changes in the position of the molecule in the lattice for a given electron state. In other contexts such as photoelectron spectroscopy (which studies vibronic transitions between potential energy surfaces, usually in the harmonic approximation), g_{α}^2 is equal to the mode-specific Huang-Rhys factor (S_{α}), which describes the strength of electron-phonon coupling[124,125]. Eigenfunctions of $H_{Holstein}$ are localized states centered on the molecular sites. Transport in this regime proceeds stepwise with each step requiring a charge carrier to escape the potential well created by E_{pol}, thus the transport is thermally activated, e.g. hopping-like transport. This is best visualized as a charge carrier moving in a cloud of phonons from localized state to localized state, a cloud whose diameter depends on the ratio between E_{pol} and t. Introducing a small but non-zero transfer integral (narrow band limit) leads to the following transition rate between neighboring localized sites in the high temperature limit ($\hbar\omega_0/kT<<1$) as calculated by Holstein for a system coupled to a dispersionless intramolecular phonon.

$$W_{hop} = \frac{t^2}{\hbar^2}\left[\frac{\pi}{2kTE_{pol}}\right]^{1/2} \exp\left[\frac{-E_{pol}}{2kT}\right] \tag{1.18}$$

Equation 1.(3. predicts that the hopping rate will decrease with a larger E_{pol}, a smaller transfer integral, t, or lower temperature. The hopping mobility has a similar form to W_{hop}. Interestingly, Marcus' electron transfer rate is identical[126] to equation 1.(3. with the replacement of $E_{pol}=\lambda/2$, where λ is the reorganization energy, assuming ground and excited state frequencies are the same. The effect of λ on the charge transfer process is diagrammatically portrayed in the potential energy surfaces of a donor-acceptor pair of Figure 1.7.

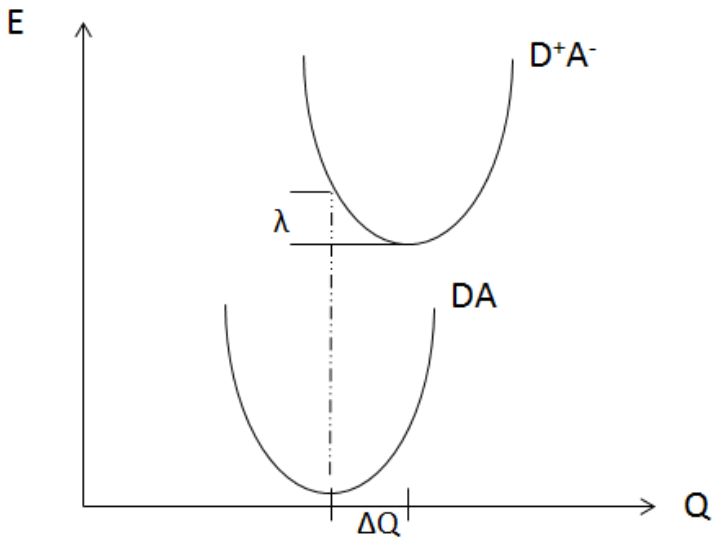

Figure 1.7: Potential energy surfaces of a donor-acceptor electron transfer process along normal coordinate Q.

The contribution to E_{pol} is generally assumed to be mainly from intramolecular phonons rather than intermolecular ones, because E_{pol} was derived by considering only modulations of the site energy. The site energy is intimately related to molecular quantities such as the IP or EA due to the van der Waals nature of the intermolecular forces. This claim has been explored theoretically using a few different approaches[24,26,127–129] that have shown that the intermolecular contribution to E_{pol} is only a few percent of the total. Experimentally, E_{pol} is usually determined from a Frank-Condon analysis of the intensities of vibronic transitions in UPS[98,130,131] (Ultraviolet Photoelectron Spectroscopy) spectra[124]. Additionally, E_{pol} can also be extracted using vibrational spectroscopy (either IR or Raman) in CT compounds by looking at changes in intramolecular phonon frequency between the neutral, ionic, and CT molecules[89]. The values of E_{pol} and the transfer integrals for holes of various molecular systems are E_{pol}~78 meV[132] and t~105 meV[121] for rubrene, E_{pol}~59 meV[133] and t~90 meV[22,134] for pentacene, and E_{pol}~125 meV[64,95] and t~85 meV[64] for DBTTF-TCNQ. These values of E_{pol} show that its magnitude is similar to that of the largest hole transfer integrals. From this outlook it is clear that local eph coupling is an important

parameter in discussing charge transport properties of organic semiconductors. However, the transfer integral is not in fact much smaller than E_{pol}, as was assumed in deriving the small-polaron hopping model of equation 1.(3.. In the regime of higher transfer integral, the effect on the eigenfunctions of the system will be to delocalize them so that the electronic wavefunction is now spread out over a number of molecular sites. This type of wavepacket is termed the large polaron and exists whenever the bandwidth is much larger than E_{pol}. Instead of localized states as in the small polaron picture, for the large polaron there exists a band of energies whose width is proportional both to the transfer integral and to an exponentially decaying function of E_{pol}:

$$Bandwidth \sim t * \exp[-E_{Pol}] \tag{1.19}$$

Electronic wavefunctions in the large-polaron region are described by band-like plane wave functions. As the temperature increases the bandwidth of the polaron-band narrows and at a certain point the band picture is no longer applicable for the system. At this point a small-polaron model is invoked to describe the charge transport at this band-to-hopping transition. Interestingly, this kind of transition has been used to describe the temperature dependence of the electron mobility of naphthalene in the c' direction.[135] The Holstein model however is limited in its scope, as it only considers local coupling (site energy modulation), whose main contribution is from high frequency intramolecular phonons.

1.5.5 Non-local Peierls coupling:

A full description of charge transport requires the inclusion of non-local effects. Where local coupling describes modulations in site energy due to phonons, non-local coupling describes the modulation of the transfer integrals due to phonons. In looking at the vibronic Hamiltonian of equation 1.4, linear non-local coupling is categorized in $H_{t\text{-}p}$ of equation 1.8. A non-zero non-local coupling constant, $f_{\alpha,nm}$, results from displacements in intermolecular positions or

orientations of neighboring molecules caused by intermolecular phonons. As mentioned earlier, the energy of the transfer integral comes from the overlap of the HOMO/LUMO π-levels of neighboring molecules. The orbital overlap and not necessarily the spatial proximity of the neighboring molecules is important. It is possible for phonons that draw molecules spatially closer to exist but have no effect on the transfer integral, because the orbital overlap does not change with vibration. This type of phonon would give a zero non-local coupling constant. Figure 1.8 portrays how librational and translational phonons can have non-zero non-local coupling; note how the orbital overlap changes with phonon type.

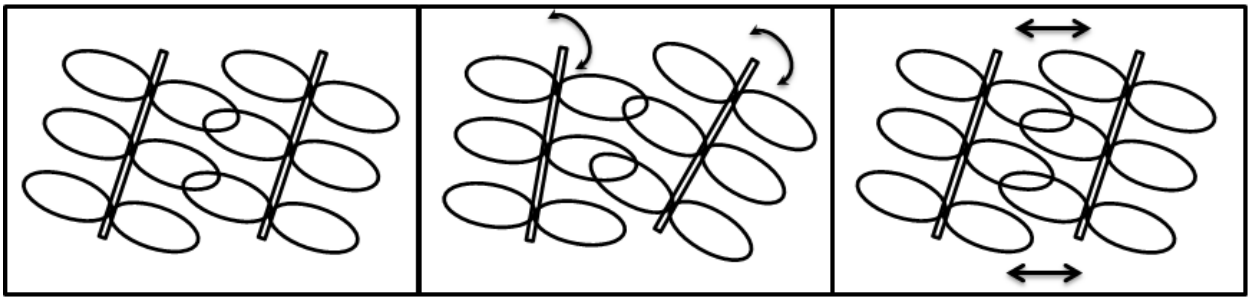

Figure 1.8: Impact of intermolecular phonons on the transfer integral. From left to right; static position, effect of librations (hindered rotations), and translations on transfer integral.

The non-local eph coupling constant L is usually quantified in a manner similar to E_{pol}, by defining[23]

$$L_{nm} = \sum_{\alpha} \frac{f_{\alpha,nm}{}^{2}}{\hbar\omega_{\alpha}} \tag{1.20}$$

In this fashion, L acts similarly to the mechanism of E_{pol} in the case of local coupling, and increases charge carrier scattering by phonons[127]. However, L is also related to the variance of the thermal fluctuations of the transfer integral[22,136], so that when the t^2 term in equation 1.(3. is thermally averaged, it is transformed as in equation 1.21.

$$\langle t^2 \rangle \rightarrow t^2 + \sigma^2; \text{ where } \sigma^2 = \sum_\alpha \frac{f_{nm,\alpha}^2}{2} \coth\left(\frac{\hbar\omega_\alpha}{2kT}\right) \quad (1.21)$$

This makes non-local coupling much harder to incorporate into charge transport models because of the two opposite functions it plays in charge transport. A number of theoretical groups[23,129,137] have evaluated non-local coupling constants using various approaches. For example, the magnitude of L was calculated to be 10-20% of the total transfer integral[138] in pentacene by one group. Furthermore, it was shown that there is even significant coupling below the frequency of the lowest optical phonon (<20cm^{-1}), meaning that acoustic phonons are also important in describing charge transport in organic semiconductors. Studies[22] on non-local coupling in oligoacenes as a function of the number of acene rings have shown that even high-frequency modes can couple non-locally, but only to a limited extent; their contribution decreases as the number of acene rings increases. Calculations of non-local coupling in both CT and mono-molecular organic semiconductors have revealed that phonons of frequency <300 cm^{-1} contribute to roughly 80% or more of the total non-local coupling in those systems.[65,127,139] Experimental studies on non-local coupling are very rare and the author is aware of only one group that has looked at non-local coupling in systems of SS CT compounds composed of symmetric dimers by modeling resonance Raman spectra with a two site 1-D tight binding Peierls-Hubbard Hamiltonian [103,140].

1.6 Chapter summary

In summary, the charge transport process is extremely complicated. Inclusion of eph coupling drastically increases the difficulty of a general model for charge transport in organic semiconductors. For a given theoretical charge transport model, understanding the scale and effect of each model parameter is important in developing a better understanding of charge transport. Connecting theoretical estimates with those of experiment is vital in creating new and

better charge transport descriptions. As described in the remainder of this dissertation, the microscopic parameters identified here that are necessary to incorporate eph coupling to model charge transport have been derived from Raman spectroscopic measurements of charge transfer compounds to estimate the magnitude of electron-phonon and electronic coupling in these systems. In chapter 4, the degree of charge transfer and the magnitude of local electron-phonon coupling will be determined for the PnT1 system and compared with theoretical determination. Chapter 5 will look at both intermolecular and intramolecular phonons, in order to extract both the local and non-local electron-phonon coupling constants in the CT compound APMDA and compare with theoretical determinations.

CHAPTER 2: MATERIALS

2.1 PnT1: Background and prior research

2.1.1 PnT1 basic information

PnT1 (n=1,2,3) is a system of CT compounds comprised of varying ratios of perylene ($C_{20}H_{12}$) and TCNQ (7,7,8,8-tetracyanoquinodimethane) ($C_{12}H_4N_4$) molecules (donor:acceptor ratio of 1:1, 2:1, or 3:1). P1T1[141] and P3T1[142] were discovered in the 1970s and P2T1 more recently in 2014[63]. The chemical and crystal structures of this system are shown in Figure 2.1 and Figure 2.2.

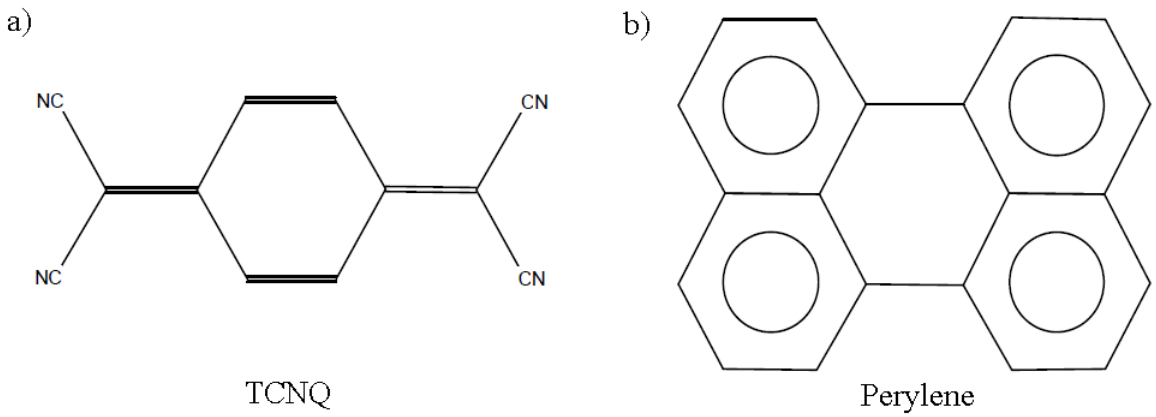

Figure 2.1: Chemical drawings of a) TCNQ and b) perylene

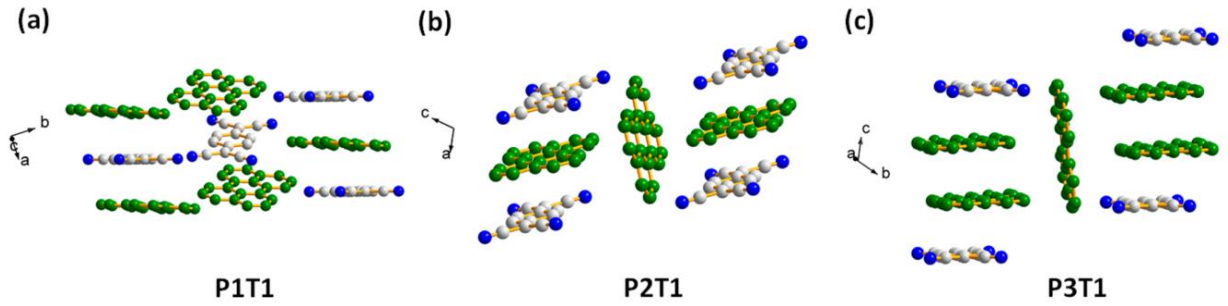

Figure 2.2: Crystal structures of PnT1. In order to distinguish molecules, carbon atoms are shown as green spheres for perylene and white spheres for TCNQ. The blue spheres on the TCNQ molecule represent nitrogen atoms. (adapted from ref.[63])

The crystal structure of P1T1 is monoclinic with two formula units per unit cell and space group symmetry of $P2_1/b$. Both P2T1 and P3T1 are triclinic with one formula unit per unit cell and have the same space group symmetry of $P\bar{1}$. In the solid state the molecules retain their planar gas phase nature. P1T1 consists of two symmetry-inequivalent DA stacks in the unit cell, while P2T1 consists of a DA stack with an extra perylene molecule separating adjacent DA stacks whose long axis is coincident with the molecular stacking axis. P3T1 is similar to P2T1 except that it consists of perylene-separated DAD stacks. The PnT1 materials were grown by our collaborators, Dr. Christian Kloc and his group at Nanyang Technological University. The crystals studied were grown from the gas phase using physical vapor transport (PVT)[143]. PVT growth of P1T1 crystals tends to form needle-like structures, whereas PVT growth of P2T1 and P3T1 forms platelet-like structures. A growth scheme has not yet been developed for P2T1, as it was found rarely and usually among P3T1 platelets. The PnT1 crystals are shown in Figure 2.3. This system of materials is unique in that there are three compounds with three different structures, yet all having the same chemical species present i.e. perylene and TCNQ. Choosing to study this system gives the opportunity to study structure-property relationships in CT compounds more generally, including the effect of structure on the electronic or vibrational properties.

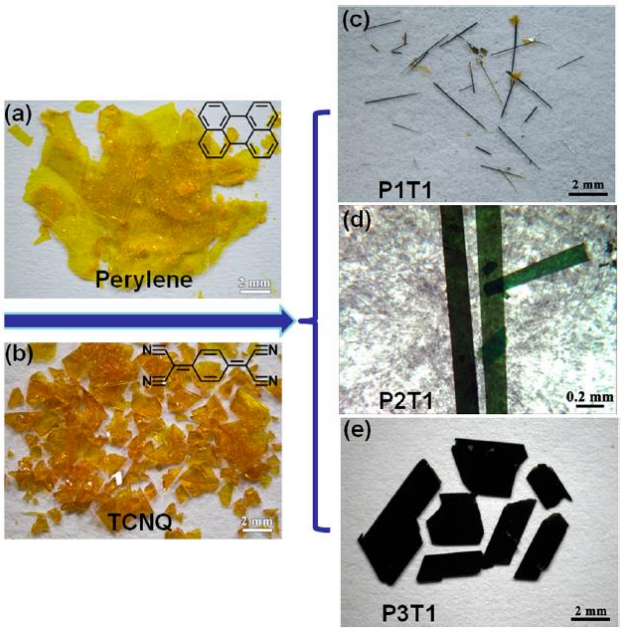

Figure 2.3: Optical images of PnT1 crystals a) perylene b) TCNQ c) P1T1 (gas phase) d) P2T1 (gas phase) e) P3T1 (solution). P2T1 and P3T1 look very similar to one another when grown from the gas phase.

2.1.2 Prior research

X-ray studies have been performed on P1T1 and P3T1 which focused on basic crystal structure, bond lengths and angles, and molecular packing. Such studies revealed that the perylene and TCNQ molecules are oriented relative to one another such that they maximize the CT stabilization of the ground state.[144] The projection of TCNQ onto the plane of perylene shows that the CT interaction is maximal when the center of the quinone ring of TCNQ is positioned over the middle of the C-C bond connecting the two naphthalene moieties of perylene. By using an empirical X-ray method[93] for determining the degree of CT of TCNQ-based CT compounds, it was found that P3T1 has a degree of CT of ~0.2[142].

Bandrauk[145–148] and his group thoroughly explored the basic optical and spectroscopic qualities of P1T1 and P3T1. The absorption spectra of the two compounds are similar with molecular excitonic absorptions occurring below 520 nm and a charge transfer excitation in the

near-IR at ~960nm. Furthermore, polarized reflection spectra showed that the charge transfer excitation is polarized along the molecular stacking axis of the two compounds. Vibrational modes of the two compounds were characterized using Raman spectroscopy and infrared absorption with intramolecular phonons identified as belonging to either perylene or TCNQ. Only the low frequency (<200 cm^{-1}) spectrum of P3T1 was analyzed. The group also used resonance Raman scattering to see that the scattering cross sections of only the perylene phonons increase as the incident energy is tuned toward 457 nm (blue). This was attributed to resonance of the cross sections with the lowest singlet excited state of perylene.

Studies following Bandrauk focused on the electronic properties of the two compounds. Ishii[149] analyzed the photoconduction and reflection spectra of P1T1 and P3T1. It was shown that the threshold for photoconduction in both P1T1 and P3T1 was close in energy to the energy to create a pair of thermally-relaxed charge carriers of ~1.7 eV. The peak in photocurrent of P3T1 was observed to be about one to two orders of magnitude smaller than that in P1T1. This observation was explained by noting the lack of absorption in the P3T1 compound between the CT excitation and the molecular exciton region, whereas in P1T1, there is increasing absorption most likely from higher CT states. Kuroda[150] used polarized reflectance measurements of P1T1 at two different pressures to estimate the microscopic charge transport parameters at those pressures. In his analysis of the reflectance spectra of the CT transition, he used the solution of the tight binding 1-D Hamiltonian developed by Painelli and Girlando[90] for mixed stack CT compounds in order to estimate the transfer integral (t), the degree of CT (ρ), and the site-energy difference between adjacent donor and acceptor molecules (ε_d-ε_a). His estimates were 0.25 eV for t, 1.2 eV for ε_d-ε_a, and 0.1 for ρ. More recently in 2008 de Groot et al.[3] calculated the electronic band structure of P1T1 using DFT. He calculated that the effective charge carrier

masses and bandwidths are similar for both holes and electrons along the stacking axis, due to the symmetry of the crystal structure. Furthermore, the field effect mobility was measured to be ~0.3 $cm^2V^{-1}s^{-1}$ and found to be best described by electron transport.

In conclusion, much ground work has been laid out on the basic vibrational and electronic properties of P1T1 and P3T1. However, no study on electron-phonon coupling or the degree of CT for the full PnT1 system has been attempted prior to the work of this dissertation.

2.2 Anthracene-Pyromellitic Dianhyride: Background and Prior Research

2.2.1 Anthracene-PMDA basic information

Anthracene-PMDA (APMDA) is a CT compound with anthracene ($C_{14}H_{10}$) as the donor (IP~7.42 eV[151]) and PMDA (furo[3,4-f][2]benzofuran-1,3,5,7-tetrone) ($C_{10}H_2O_6$) as the acceptor (EA~2 eV[152]). The chemical and crystal structures are shown in Figure 2.4 and Figure 2.5.

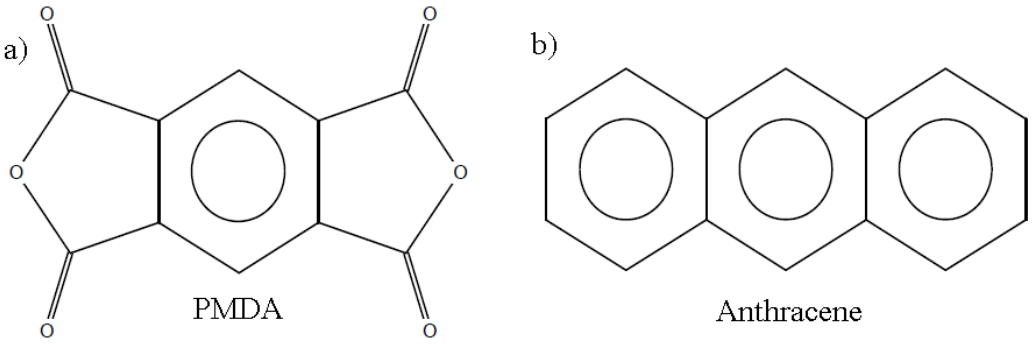

Figure 2.4: Chemical drawings of a) PMDA and b) anthracene.

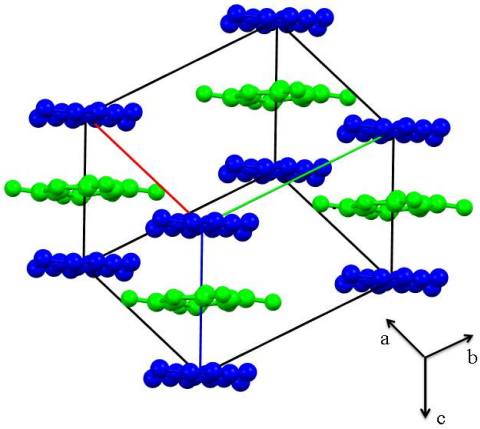

Figure 2.5: Crystal structure of APMDA. Blue molecules are Anthracene and green are PMDA.

The crystal structure of APMDA is triclinic of space group $P\bar{1}$, which means that each molecule is located at an inversion center of the unit cell. Anthracene and PMDA molecules are stacked along the crystallographic c-axis and spaced roughly 3.5 Å from each other. Like PnT1, these crystals were formed from the gas phase using PVT. They were grown by our collaborators from Wake Forest University, the Jurchescu group. APMDA crystals tend to form in long flat needle-like samples, where the needle axis is coincident with the molecular stacking axis i.e. the c-axis.

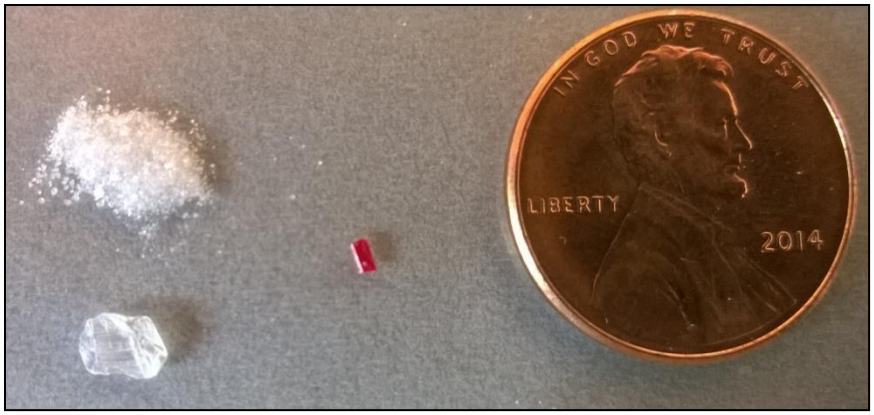

Figure 2.6: Crystals of PMDA (top left) anthracene (bottom left) and APMDA (right) compared with the size of a penny.

2.2.2 Prior research

Since its discovery[153] in the 1960s, considerable research into the optical and electronic properties of APMDA has been completed. From solution UV-Vis absorption spectra it was first

discovered that there was a charge transfer excitation at ~470nm[154]. Subsequent solid state polarized absorption, reflection, and fluorescence measurements showed that there was underlying vibronic structure not seen in the solution phase, which was attributed to the polar nature of the CT state.[155–157] The CT exciton was identified as the lowest excited singlet state polarized along the stacking axis (c-axis) of the crystal with a lifetime of ~4 ns at room temperature[155]. At low temperature (2K), phosphorescence is observed with a lifetime of ~15 msec, whose intensity depends on the crystal growth method.[155] A Stokes shift of 1900 cm^{-1} was observed between the absorption and fluorescence, implying rearrangements in the intermolecular coordinates between the ground state and the excited CT state. Furthermore, at low temperature the optical spectra become a series of sharp zero-phonon transitions with accompanying phonon side-bands.[156] The sharp peaks correspond to vibronic transitions starting from the 0-0 to the simultaneous excitation of the electronic CT transition and an intramolecular phonon. The phonon side-bands accompanying the sharp vibronic transitions are the result of intermolecular coupling to the vibronic transition. Closer analysis of the phonon side-bands in the low temperature polarized reflection spectra reveals transitions at frequencies corresponding to experimentally-observed intermolecular APMDA phonons. The similarity between the optical spectra of APMDA and those of color centers in alkali halides led researchers to apply the same local-state phenomenological model to APMDA[156]. In this model each excitation of an intramolecular phonon with charge transfer is treated as a separate excited state that couples independently to a set of intermolecular phonons. From this point of view, exciton-phonon coupling of the CT transition can be extracted from the ratio of intensities of the zero-phonon line and the total intensity of the transition including its phonon side band, giving a Huang-Rhys factor of S~6. The Huang-Rhys factor S is proportional to the displacement of the excited state

potential energy surface from the ground state, i.e. $S \alpha \Delta^2$, where Δ is the dimensionless displacement. The local nature of this model is that it considers only short-range charge transfer interactions by breaking down the DA stacks into trimers of either ADA or DAD. Basis functions such as $|D^+A^-D>$ and $|D\ A^-\ D^+>$, which represent charge transfer either to the right or left, make up the ground and excited states along with |DAD>. Using symmetric and anti-symmetric combinations of these functions creates two CT states of opposite parity, one that is dipole-allowed and the other that is not. Stark effect experiments on the zero-phonon line have observed the dipole-forbidden CT state[158]. At zero electric field, the two states are just 10 cm^{-1} apart; they increase their spacing with applied electric field. In addition, from the Stark effect experiment a change in dipole moment between the ground state and the CT exciton can be extracted and was measured to be ~11 debye, further confirming the polar nature of the CT exciton and the neutral nature of the ground state. Another application of the local model is that the change in intermolecular distance between D and A molecules upon charge transfer can be calculated[157] to be 0.11 Å using simple coulombic considerations.

The low frequency Raman spectrum below 140 cm^{-1} has been studied in some detail by one group from IBM[159]. Presumably the spectrum above 140 cm^{-1} has been measured as well from inferences made by different authors, all from the same IBM research laboratory, but these measurements appear not to have been published to date. According to crystal and molecular symmetry arguments, there are six librational intermolecular fully symmetric (A_g) phonons expected, three of which correspond to anthracene and the other three to PMDA. All six are Raman active below 140 cm^{-1}. Using the moments of inertia of anthracene and PMDA extracted from a rigid body analysis of APMDA X-ray data, librational frequencies of anthracene and PMDA can be calculated along each molecular principal axis. Assignment of the observed

librational modes can be made based on comparing these calculated frequencies with the observed values. Resonance enhancement of the scattering cross section for low frequency modes was also observed as the excitation energy approached the energy of the CT exciton. In the range of excitation energies used, only two modes were observed to be resonantly enhanced, while the others either remained constant or decreased in intensity.

The onset of the photogeneration of charge carriers in APMDA begins roughly at the wavelength at which the increase in absorption due to the CT exciton begins. Temperature-dependent photoconductivity measurements reveal a constant activation energy for photo-generation of 0.14 eV with an excitation energy above 2.1 eV, which is near the maximum absorption intensity of the CT exciton (max. at 2.27 eV). This value is quite similar to the adiabatic band gap of 2.38 eV[160] calculated using the ionization potential of the crystal (~6 eV)[161], the ionization potential of anthracene (~7.42 eV)[151], and the electron affinity of PMDA (~2 eV)[152], implying that the electron-hole pair of the CT exciton can be thermally separated to generate charge carriers. This is shown by the photoconductivity measurements. Charge transport measurements on APMDA have been completed using mobility time-of-flight experiments of both holes and electrons versus temperature.[162] The charge carrier mobility is anisotropic with maximum mobility occurring along the DA stacking axis. Electron mobility along the stacking axis was measured to be ~0.2 $cm^2V^{-1}s^{-1}$ at 370 K, whereas the electron mobility perpendicular to the stacking axis at 370 K is 7 times smaller. Furthermore, the electron mobility parallel to the stacking axis is thermally activated below 350 K with activation energy of 0.22 eV, and becomes temperature independent above 350 K. The interpretation is that below 350 K the mobility is trap limited and above 350 K the electron traps become ineffective so that the mobility becomes uninhibited. The electron mobility perpendicular to the stack was observed

to decrease with temperature as $\sim T^{-2}$, which is consistent with behavior that is unaffected by trap sites, because it was only measurable at temperatures higher than 370 K. At 100 ^{o}C, hole mobilities measured both parallel and perpendicular to the stack, were measured to be smaller than electron mobilities by as much as two orders of magnitude. Temperature dependence of the hole mobilities in both directions reveals that these are thermally activated due to the presence of deep (~0.5 eV) hole traps in the temperature range measured (>370 K).

In conclusion, there has been substantial research in understanding the optical and electronic properties of APMDA. However, as in the case of PnT1, electron-phonon coupling is not yet fully understood in APMDA. Some estimates of the overall exciton-phonon coupling in APMDA have been made using optical absorption and reflection measurements (see above), however no mode-specific coupling, either local or non-local, has been measured. In addition, non-local coupling of intermolecular modes seems to be an important mechanism for charge transport due to the presence of the broad phonon side bands in the low-temperature optical spectra. This will be explored in this dissertation in chapter 5.

CHAPTER 3: EXPERIMENTAL TECHNIQUES

3.1 Introduction

This chapter presents the experimental tools and methodologies used in this project to study charge transport and electron-phonon coupling in CT compounds. There are two major sections: Section 3.2 on Raman spectroscopy and Section 3.7 on optical absorption. Each section begins with an explanation of the theory behind the technique followed by a description of how I carried out the technique in practice.

3.2 Raman Spectroscopy

3.2.1 Brief historical note

This technique is based on the phenomenon in which a photon of momentum, k_i, and energy, E_i, incident on a material will be scattered inelastically with a scattered momentum, k_f, and energy, $E_i \pm E_q$, where $E_q$is the energy of a quantum state of the material. This phenomenon was first observed by Raman and Krishnan[163] in 1928. A theory was developed for atomic systems by Kramers and Heisenberg[164] in 1925 in analogy to the classical theory of scattering and then it was formulated in full quantum mechanical language by Dirac soon after in 1927[165]. As the theory developed, two interpretations of Raman scattering emerged. One interpretation, termed the 'vibronic' approach and championed by Albrecht[166], was favored by those studying molecular and polymer systems and was derived using second-order time-dependent perturbation theory. The other interpretation emerged out of the field of solid state physics in studying periodic solids such as semiconductors (e.g. silicon) and insulators (e.g. diamond), whose

derivation involves third-order perturbation theory; see Loudon[167] and Cardona[168]. This dissertation will focus on the vibronic approach.

3.2.2 Classical Raman scattering

Classical oscillating dipoles of the scattering centers induced by the incident light will radiate power according to the dipole approximation as (in mks units)[169]

$$\frac{dP_s}{d\Omega} = \frac{{\omega_s}^4 |\varepsilon_s^* \cdot \vec{\mu}_{ind}|^2}{32\pi^2 \epsilon_0 c^3} \tag{3.1}$$

In equation 3.1 ω_s is the frequency of the oscillating dipole, ε_0 is the permittivity of free space, c is the speed of light, ε^* is the complex conjugate of the scattered electric field unit vector, and μ_{ind} is the induced harmonic dipole moment. The induced dipole can be related to the polarizability of the material by

$$\vec{\mu}_{ind} = \bar{\alpha}\vec{E}_I = \bar{\alpha}E_I^0 e^{i(k_I z - \omega_I t)} \cdot \varepsilon_I \tag{3.2}$$

The polarizability, α, is a tensor whose dimensions are usually defined with respect to the principal axes of the material or molecule, and then transformed into the laboratory coordinate reference frame. k_I is the wave vector of the incident light moving in the z-direction, ω_I is the frequency of the incident light, and ε_I is the unit vector describing the polarization of the incident electric field. Plugging this into equation 3.1 gives

$$\frac{dP_s}{d\Omega} = \frac{{\omega_s}^4 \left|\varepsilon_s^* \cdot \bar{\alpha} \cdot \varepsilon_I E_I^0 e^{i(k_I z - \omega_I t)}\right|^2}{32\pi^2 \epsilon_0 c^3} \tag{3.3}$$

In a homogeneous medium, the oscillating dipole will oscillate at the same frequency as the incident electric field; this is known as Rayleigh scattering. However, inhomogeneous effects in space and time, such as phonons, will lead to modulations of the polarizability tensor at frequencies other than that of the incident electric field. Expanding the polarizability in a Taylor

series with respect to phonons of normal coordinate Q about their equilibrium position Q_0 leads to

$$\alpha_{ij} = \alpha_{ij}^0 + \sum_i (\frac{\partial \alpha_{ij}}{\partial Q_i})_{Q_0} Q_i + \sum_i (\frac{\partial^2 \alpha_{ij}}{\partial Q_i \partial Q_j})_{Q_0} Q_i Q_j + \cdots \quad (3.4)$$

And assuming a harmonic dependence on the normal coordinates

$$Q_i = Q_{0i} e^{i(\pm k_{pi} z \pm \omega_{pi} t)} \quad (3.5)$$

where k_{pi} is the wave vector of the ith phonon and ω_{pi} is its frequency and Q_{oi} its amplitude.

$$\frac{dP_s}{d\Omega} = \frac{{\omega_s}^4 |E_I^0|^2}{32\pi^2 \epsilon_0 c^3} X \ldots$$

$$(\left| \varepsilon_s^* \cdot (\alpha_{ij}^0 e^{i(k_I z - \omega_I t)} + (\frac{\partial \alpha_{ij}}{\partial Q_i})_{Q_0} e^{i((k_I \pm k_{pi}) z - (\omega_I \pm \omega_{pi}) t)}) \cdot \varepsilon_I \right|^2) \quad (3.6)$$

$$(\frac{dP_s}{d\Omega})_{Raman} = \frac{{\omega_s}^4 |E_I^0|^2}{32\pi^2 \epsilon_0 c^3} \left| \varepsilon_s^* \cdot (\frac{\partial \alpha_{ij}}{\partial Q_i})_{Q_0} \cdot \varepsilon_I \right|^2$$

In equation 3.6 only one normal coordinate is taken into account for the sake of simplicity. The modulations in the polarizability due to a phonon lead to coupling between the incident electric field and the phonon, resulting in three frequency components of radiation. The first is the Rayleigh-scattered light, where there is no change in the frequency of the scattered light from that of the incident light. The other two components correspond to the Raman-scattered light with a frequency shifted from that of the incident light by the energy of the phonon, $\pm\omega_P$. Stokes scattering refers to the negative sign of ω_P and anti-Stokes scattering the positive sign. What is also shown in equation 3.6 is that the power of the scattered radiation for Raman scattering is related to the square of the modulus of the change in polarizability of the material due to a particular phonon. Phonons in which the polarizability is unchanged will not be observed in a

Raman spectrum. Therefore the symmetry of the phonon is highly important in determining if it will be observed in the scattered radiation (see section 3.2.4). Finally, equation 3.6 gives two conservation rules for Raman scattering, namely

$$k_s = k_I \pm k_P; \qquad \omega_s = \omega_I \pm \omega_P \tag{3.7}$$

Typical magnitudes of wave vectors for optical phonons are between 10^1-10^3 cm^{-1} and for visible light ~12-25x10^4 cm^{-1}. Comparison of the magnitude of the wave vectors with that of the wave vector of the first Brillouin zone edge of ~10^7 cm^{-1} shows that first-order Raman scattering samples phonons that are near the Γ point (k≈0) of the Brillouin zone. The differential cross section for classical Raman scattering can be obtained by dividing by the intensity of the incident light i.e. $\varepsilon_0 cE^2/2$, to give

$$\left(\frac{d\sigma}{d\Omega}\right)_{Raman} = \frac{{\omega_s}^4}{(4\pi\epsilon_0)^2 c^4}\left|\varepsilon_s^* \cdot \left(\frac{\partial \alpha_{ij}}{\partial Q_i}\right)_{Q_0} \cdot \varepsilon_I\right|^2 \tag{3.8}$$

3.2.3 Quantum mechanical picture of Raman scattering

Going from a classical to a quantum picture for Raman scattering requires introducing the transition polarizability tensor, α_{if}, where 'i' and 'f' are initial and final quantum states of the system. From the conservation rules of equation 3.7 in the previous section, Raman scattering occurs only between those states that differ in initial and final state index, i.e. have different energies and momenta. Calculation of the transition polarizability tensor lies at the heart of the quantum theory of Raman scattering. Before looking at the quantum mechanical expression for the transition polarizability tensor, selection rules for Raman scattering will be discussed.

3.2.4 Selection rules:

The quantum mechanical dipole transition moment is defined as

$$\mu_{ij} = \langle i|\hat{\mu}|j\rangle \tag{3.9}$$

|i> and |j> are the initial and final quantum states of the material under inspection. By analogy the induced transition dipole moment is defined as

$$\mu_{if}^{ind} = \langle i|\hat{\alpha}|j\rangle E \tag{3.10}$$

In the previous section, it was shown that the differential cross section is proportional to the square of the dipole moment. Therefore, for there to be a non-zero intensity of a Raman transition, the direct product of the transition polarizability with the symmetry of the initial and final states needs to be fully symmetric. Otherwise, the integral of equation 3.10 will be zero.

$$\Gamma_1 \subset \Gamma_i \otimes \Gamma_\alpha \otimes \Gamma_j \tag{3.11}$$

Γ_1, the fully symmetric irreducible representation, is contained in the direct product of the irreducible representations of the corresponding vibronic states ($\Gamma_{i,j}$) and the polarizability tensor (Γ_α). Using the Born-Oppenheimer approximation, a material's eigenstates can be broken up into those belonging to its electronic, vibrational, and rotational degrees of freedom. Let the indices, g and e, represent the initial and final electronic states and i and f refer solely to the initial and final vibrational states. Using this approximation in equation 3.11 leads to the following selection rule:

$$\Gamma_1 \subset (\Gamma_g \otimes \Gamma_i) \otimes \Gamma_\alpha \otimes (\Gamma_j \otimes \Gamma_e) \tag{3.12}$$

$\Gamma_{g,e}$ are the irreducible representations of the initial and final electronic states with 'i' and 'f' now referring to vibrational states . Rotational states in molecular crystalline materials are known as hindered rotations, or librations, and are treated similarly to a vibrational phonon, thus there is no need to add any rotational irreducible representation to equation 3.12. For a molecule in a crystal, there are three librations that correspond to hindered rotations, usually along the principal axes of

the molecule. In Stokes scattering, which is commonly used because it is more intense than anti-Stokes at room temperature, the initial state is the ground state of the material for both the electronic and vibrational degrees of freedom. The final electronic state is usually also the ground state; therefore, Γ_g, Γ_e, and Γ_i are all represented by the fully symmetric irreducible representation Γ_1. Thus, if the symmetry of a phonon is contained within the irreducible representation of the polarizability tensor, then the phonon is Raman active, that is, it is allowed by symmetry to be observed. Pertinent Raman processes are diagrammed in Figure 3.1.

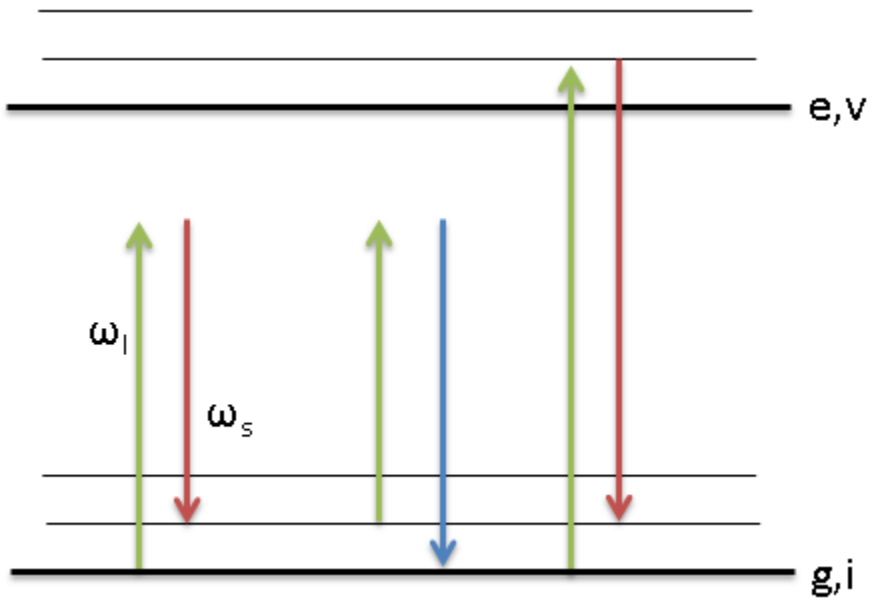

Figure 3.1: Diagram of different Raman processes. From left to right, Stokes scattering, anti-Stokes scattering, and resonance Raman Stokes scattering. g,i are the initial electronic and vibrational states and e.v are the excited electronic and vibrational states.

3.2.5 Quantum transition polarizability tensor

A full derivation of the quantum mechanical transition polarizability tensor is beyond the scope of this project, therefore only a brief description of its derivation and the result will be given. Beginning from the Hamiltonian for the molecular crystal and the radiation field, an interaction term is added describing the coupling between the radiation field and the charged

electrons and nuclei. This term is treated as a perturbation to the unperturbed eigenstates of the original Hamiltonian. In Raman scattering a quantum of light is absorbed by the material from the incident radiation field and a light quantum is created at a different frequency in the scattered radiation field. Second-order time-dependent perturbation theory can be used to calculate the transition probability between these initial and final states, which differ by one quantum of radiation, in the adiabatic and electric dipole approximations to give the quantum mechanical vibronic transition polarizability tensor.[166]

$$(\alpha_{\rho\sigma})_{gi,gj} = \frac{1}{\hbar}\sum_{ev}\frac{(\mu_\rho(Q))_{ev,gj}(\mu_\sigma(Q))_{gi,ev}}{\omega_{ev,gi} - \omega_I + i\Gamma_{ev}} + \frac{(\mu_\rho(Q))_{gi,ev}(\mu_\sigma(Q))_{ev,gj}}{\omega_{ev,gj} + \omega_I + i\Gamma_{ev}} \qquad (3.13)$$

In equation 3.13, ρ and σ are components of the polarizability tensor running over x, y, z, referring to the principal axes of a molecule, unit cell of a crystal, or other reference frame. The indices e and v refer to the electronic and vibrational states above the ground electronic state respectively (see Figure 3.1) and the indices i and j refer to the initial and final vibrational states of the ground electronic state, g. The frequency $\omega_{ev,gi}$ refers to the difference in energy between the two vibronic levels i.e. $\omega_{ev,gi} = \omega_e + \omega_v - (\omega_g + \omega_i)$. Γ_{ev} is the lifetime of the intermediate vibronic state 'ev'. μ(Q) is the transition moment dependent on the phonon normal coordinates, where the indices are defined as follows:

$$(\mu_\rho(Q))_{gi,ev} = \langle v|\langle e|\hat{\mu}_\rho(Q)|g\rangle|i\rangle \qquad (3.14)$$

|e> and |v> are the adiabatic excited electronic and vibrational states and |g> and |i> are the ground state adiabatic electronic and vibrational states. According to equation 3.**Error! eference source not found.**, the magnitude of the transition polarizability tensor depends on the sum over intermediate states (ev) of the transition dipole moment. The differential quantum

Raman scattering cross section can be obtained by plugging the transition polarizability tensor into equation 3.8, dividing by the incident intensity and ω_S/ω_I to give[170]

$$\left(\frac{d\sigma_{gi,gj}}{d\Omega}\right)_{Raman} = \frac{\omega_I \omega_S^3}{(4\pi\epsilon_0)^2 c^4} \left|\varepsilon_s^* \cdot (\alpha_{\rho\sigma})_{gi,gj} \cdot \varepsilon_I\right|^2 \tag{3.15}$$

3.3 Resonance Raman spectroscopy

The two terms in equation 3.13 represent the resonant and non-resonant terms for Raman scattering. When the frequency of the incident light approaches the vibronic frequency difference ($\omega_{ev,gi}$), the first term becomes large in comparison to the second term. This is the quantum mechanical understanding for resonant Raman scattering. As the resonance frequency is approached, only those states that have frequencies near the resonance frequency are important to consider. This can lead to a simplification in the calculation of the polarizability tensor as only one other electronic state typically needs to be considered. Otherwise, the problem quickly becomes intractable when considering the number of eigenstates needed to calculate a Raman transition. For example, it is possible to have 10^6 eigenstates per wavenumber for a polyatomic molecule with 6-10 degrees of freedom[171,172]. In a resonance Raman spectrum, those vibronic states near in frequency to the frequency of the incident light will experience an increase in their scattering cross sections. Equation 3.13 can be further simplified by introducing the Herzberg-Teller expansion[173] into the electronic Hamiltonian of the system, i.e. expanding the electronic Hamiltonian in a Taylor series about the phonon normal coordinates' equilibrium position. The perturbation to the electronic Hamiltonian due to the coupling of the phonon coordinates gives the following perturbed electronic eigenstates:

$$|e>=|e^0>+\frac{1}{\hbar}\sum_k\sum_{s\neq e}\lambda_{es}^k\,Q_k|s^0> \tag{3.16}$$

and similarly for |g>, where $|e^0>$ are the unperturbed electronic eigenstates, $|s^0>$ is the unperturbed electronic eigenstate of another higher excited electronic state, Q_K is the normal coordinate of the kth phonon, and λ_{es} is the vibronic coupling operator defined as

$$\lambda_{es}^k(Q)=\frac{1}{\hbar}\frac{\left\langle s^0\left|\frac{\partial H_E}{\partial Q_k}\right|e^0\right\rangle}{\omega_e^0-\omega_s^0} \tag{3.17}$$

Taking equations 3.16 and 17 and plugging them into the definition of the electronic portion of transition dipole moment defined in equation 3.14 gives

$$\begin{aligned}\mu_{g,e}(Q)=\langle e|\hat{\mu}|g\rangle&=\mu_{g,e}^0(Q_0)+\sum_{k,s\neq e}\lambda_{es}^k\mu_{g,s}^0(Q_0)Q_k\\&=\mu_{g,e}^0+\sum_k(\frac{\partial\mu_{g,e}}{\partial Q_k})_{Q_0}Q_k\end{aligned} \tag{3.18}$$

Plugging equation 3.18 into the resonant term of the transition polarizability tensor of equation 3.13, three terms for resonance Raman scattering known as Albrecht's[166] 'A', 'B', and 'C' terms emerge.

$$(\alpha_{\rho\sigma})_{gi,gj}^A=\frac{1}{\hbar}\sum_{s\neq e}\sum_v\frac{(\mu_\rho)_{g,e}^0(\mu_\sigma)_{e,g}^0}{\omega_{ev,gi}-\omega_I+\mathrm{i}\Gamma_{ev}}*\langle i|v\rangle\langle v|j\rangle \tag{3.19}$$

$$(\alpha_{\rho\sigma})^{B}_{gi,gj} = \frac{1}{\hbar}\sum_{e,v}\sum_{k}\left(\frac{1}{\omega_{ev,gi} - \omega_I + \mathrm{i}\Gamma_{ev}}\right)$$

$$* \left[(\mu_\rho)^0_{g,e}\left(\frac{\partial \mu_{\sigma\, e,g}}{\partial Q_k}\right)_{Q_0}\langle i|v\rangle\langle v|Q_k|j\rangle\right. \tag{3.20}$$

$$\left. + \left(\frac{\partial \mu_{\rho\, g,e}}{\partial Q_k}\right)_{Q_0}(\mu_\sigma)^0_{e,g}\langle i|Q_k|v\rangle\langle v|j\rangle\right]$$

The 'C' term is excluded for the sake of brevity. The 'A' term is known as the Franck-Condon approximation and only depends on overlaps between vibrational wavefunctions of the ground and excited electronic states. For these overlaps to be non-zero, the excited state potential energy surface must have either a different equilibrium position or a different curvature (i.e. a different vibrational frequency) than the ground state surface.

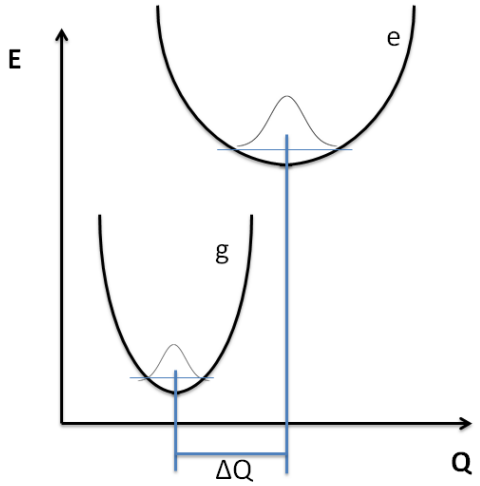

Figure 3.2: Potential energy surfaces for a phonon of normal coordinate, Q, for the ground and excited electronic states, displaced by ΔQ.

Unless there is a change in symmetry of the molecule or system upon electronic excitation, then only fully symmetric phonons will be active in 'A' term resonance , assuming there is a displacement in the potential energy minima of the two electronic states, which is generally the case. This can be seen by looking at the overlap integral <i|v>, because |i> is always fully

symmetric in normal Raman scattering, so |v> must also be fully symmetric for the overlap to be non-zero. This is possible for vibrational modes when i≠v, if the vibrational modes are not solutions from the same vibronic Hamiltonian. 'B' term resonance, or Herzberg-Teller resonance, involves the vibronic coupling of two excited electronic states, as seen in equation 3.20. There are a few factors that determine if this term is active. First, both electronic states must be dipole-allowed transitions from the ground state. Second, according to the vibronic coupling parameter of equation 3.17, the direct product of the excited electronic states with normal coordinate Q_k must be fully symmetric, meaning that for a totally symmetric phonon to be active, the two excited electronic states must possess the same symmetry, otherwise only non-totally symmetric phonons will be active. Finally, the overlap integrals imply that only fundamental modes are active in B-term resonance, i.e. transitions that differ by only one quantum between the initial and final states.

3.4 Time-dependent resonance Raman spectroscopy[171,174–178]

As described briefly in the previous section, it is extremely difficult to calculate the transition polarizability tensor to predict Raman intensities using the sum over states (Kramers-Heisenberg-Dirac) approach; there are just too many eigenstates to consider. That is why only in very specific situations, such as resonance conditions with one or two electronic states and few active vibrational degrees of freedom, can some progress be made. Heller and coworkers[172,175,179] formulated a time-dependent approach to combat this problem in 1979. Since then, their model has been extended for use in absorption and emission spectroscopy and also to include homogeneous and inhomogeneous broadening effects. A main point of resonance Raman, absorption, and emission spectroscopy is to gain information on a material's excited states. Information on excited state structure and dynamics is very important in photochemical, electron

and energy transfer, and photo-isomerization processes[180]. Using their model to simultaneously model the resonance Raman and absorption spectra, information on the excited state structure and dynamics of molecules or condensed phase systems can be extracted, such as molecular geometry changes. This model has been successfully applied to a host of diverse systems, such as solution-based charge transfer complexes[181], inorganic metal-to-ligand charge transfer systems[182,183], and biological molecules[180].

There are a couple of ways to derive a time-dependent picture for Raman scattering, such as adopting a density matrix formalism, but one easy way to see the transformation from the sum over states picture to a time-dependent picture is via the mathematical transformation of equation 3.21.[179]

$$\frac{1}{\omega_{ev,gi} - \omega_I + \mathrm{i}\Gamma_{ev}} = \frac{1}{i}\int_0^\infty dt\, \exp[-i(\omega_{ev,gi} - \omega_I)t - \Gamma_{ev}\mathrm{t}] \tag{3.21}$$

Adopting the preceding transformation to the resonant portion of the transition polarizability tensor of equation 3.13 and assuming one resonant excited electronic state gives the following resonant Raman polarizability.

$$(\alpha_{\rho\sigma})_{ij} = \frac{1}{i\hbar}\int_0^\infty dt\, exp[i(\omega_{gi} + \omega_I)t - \Gamma\mathrm{t}]\left\langle \chi_f^\rho \middle| \chi_i^\sigma(t)\right\rangle \tag{3.22}$$

In obtaining equation 3.22, the following relations were made:

$$< \chi_f^\rho| =< j|\mu_\rho(Q)_{g,e} \tag{3.23}$$

$$|\chi_i^\sigma(t) >= \exp[i\frac{H_{ev}}{\hbar}t]\mu_\sigma(Q)_{e,g}|i > \tag{3.24}$$

H_{ev} is the Hamilitonian of the excited electronic (vibronic) state. The sum over the vibrational states of the excited electronic state was closed by assuming the damping factor (Γ) is the same

for each vibrational state. Using the time dependent approach, the polarizability tensor for resonant Raman scattering is simplified to just a half Fourier transform over the overlap between a time dependent initial wavefunction propagating on the excited electronic state and the final static wavefunction of the ground state. In the Condon ('A' term) approximation, i.e. no normal coordinate dependence of the transition dipole moment, equation 3.22 can be written in terms of just vibrational wavefunctions.

$$(\alpha_{\rho\sigma})_{ij} = \frac{(\mu_\rho)^0_{g,e}(\mu_\sigma)^0_{e,g}}{i\hbar}\int_0^\infty dt\ exp[i(\omega_{gi} + \omega_I)t - \Gamma t]\langle j|i(t)\rangle \qquad (3.25)$$

In the time dependent formalism there is no need to calculate the excited vibronic eigenstates as in the sum over states model. The Raman scattering process in this picture is understood to involve the instantaneous excitation of the initial vibrational wavefunction, |i(0)>, via the dipole transition moment; then at t>0, |i(t)> propagates on the excited electronic surface by the propagator ($\exp[iH_{ev}t/\hbar]$) and decays by the damping factor ($\exp[-\Gamma t]$). As the initial wavefunction propagates on the excited electronic surface it will pick up overlap with the final vibrational wavefunction, |j>, over time and give the resonant Raman transition its intensity. To calculate the vibrational overlap between the two wavefunctions a semi-classical wave packet analysis is adopted. In this analysis, the initial and final vibrational states are treated as Gaussian wave packets that exist on multi-dimensional electronic surfaces and in the case of |i(t)> evolve on the surface versus time. The electronic surfaces are most simply represented with harmonic potentials with a unique curvature and displacement from one another. Using this method, analytic expressions for the overlaps can be obtained.[179] This scheme is represented pictorially in Figure 3.3.

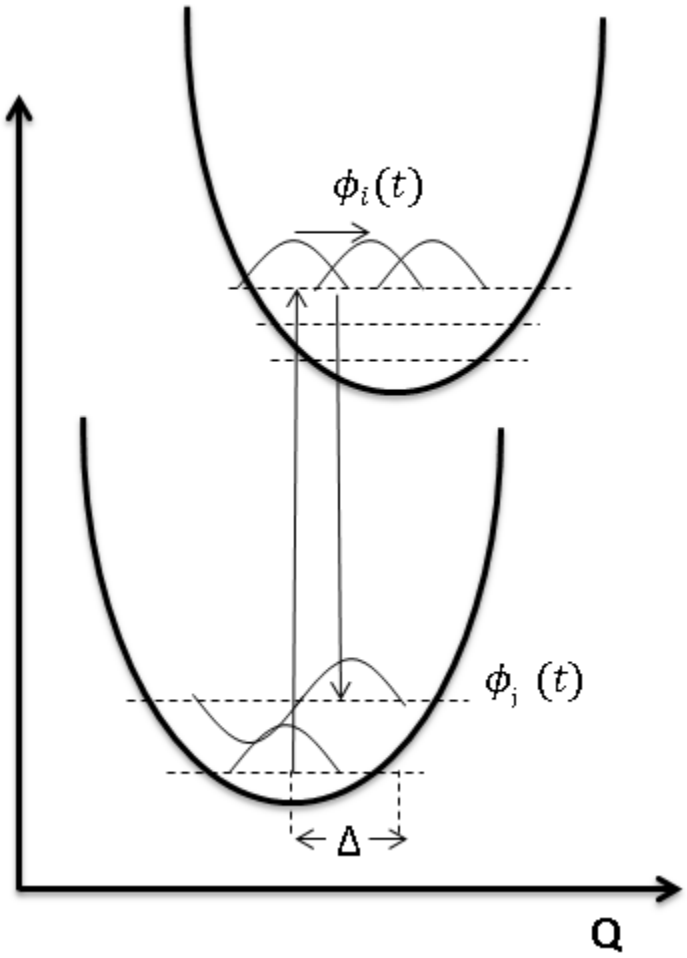

Figure 3.3: Time dependent resonance Raman diagram projected onto normal coordinate Q. Two harmonic potentials displaced by dimensionless displacement Δ. Φ_i and Φ_f are the initial and final vibrational wavefunctions. Adapted after ref.[184]

Assuming there are N vibrational degrees of freedom, each dimension of the N-dimensional electronic surfaces corresponds to a phonon normal coordinate, Q. The traveling wave packet will travel on the excited electronic state classically and travel preferentially along phonon coordinates that have either large displacements or steeper curvature due to changes in excited state phonon frequency. At later times, the wave packet will return to where it was located on the excited state potential surface, however damped by the exp[-Γt] term. Therefore, the phonons that experience the greatest increase in scattering cross section are those that have the greatest

excited state displacement along that phonon coordinate. The reorganization energy is defined in terms of the individual displacements of the phonon normal coordinates.[184]

$$\lambda_{reorg} = \sum_k \lambda_k = \sum_k \frac{\omega_k \Delta_k^2}{2} \tag{3.25}$$

Here λ_k is the reorganization energy of the kth phonon, Δ_k is its dimensionless displacement, and ω_k its vibrational frequency. It is important to note that the overlap integral (<f|i(t)>) is an N-dimensional function, which, in the absence of Duschinsky rotation, can be approximated as the product of N one-dimensional overlap integrals[176] representing the projections of the overlap integral along different phonon normal coordinates. Duschinsky rotation is the rotation of normal coordinates due to changes in molecular or crystal symmetry upon electronic excitation. In systems with large numbers of vibrational degrees of freedom, the overlap integral for a Raman transition attains most or all of its intensity during its time in the initial Franck-Condon region of the excited state (i.e. the region of the excited state potential where the wave packet is initially excited), which lasts a few to tens of femtoseconds.[172] The reason for ignoring later recurrences of the time evolving wave packet to its initial starting location is that when there are many phonons of differing frequencies, it is rare for them to all return to the Franck-Condon region at the same time. For example, if just one of the one-dimensional overlap integrals is zero because it has not yet returned to the Franck-Condon region, then the entire N-dimensional overlap integral will also be zero. At longer times, the N-dimensional integral may return, but the damping factor will be sufficiently large to prevent any contribution to the overall intensity. This is known as the short-time dynamics limit. In fact, a few simple expressions describing the relative intensities of resonant Raman transitions can be made in the short time dynamic limit, namely under the pre-resonance limit. Heller and coworkers[175] showed that when the frequency

of the incident radiation is detuned from resonance, the overlap integral oscillates rapidly and self-cancels for times greater than the inverse of the detuning frequency ($\Delta\omega^{-1}$). This means essentially that the farther the frequency of the incident radiation is from the resonance frequency, the shorter the amount of time the excited wave packet spends on the excited state surface. In this limit, they showed that the intensity of a Raman transition was related to the slope of the potential energy surface along that phonon coordinate[172].

$$\frac{I_1}{I_2} = \frac{\omega_1^2 \Delta_1^2}{\omega_2^2 \Delta_2^2} \tag{3.26}$$

In equation 3.26, I_k refers to the intensity of an observed resonant Raman transition, ω_k the ground state frequency, and Δ_k the dimensionless displacement.

In order to accurately model the dispersion of the Raman polarizability tensor (resonant Raman excitation profile), the interaction of the vibronic potential energy surfaces with their environment needs to be taken into account. The model presented so far is local in nature in that it assumes the traveling wave packet interacts with only the observed resonant Raman vibrational modes of the excited vibronic surface before it decays back to the ground state with the natural lifetime of the excited state, Γ. However, in a molecular crystal at finite temperature the wave-packet will couple to other degrees of freedom, such as acoustic modes or other optical phonons that are not included in the model. The resonant excitation will be surrounded by non-resonant neighbors along the same stack, or in other stacks. In addition, static disorder and thermal fluctuations are present in molecular crystals[153,185,186] which leads to variation in photo-physical parameters, such as the resonant frequency and, by extension, the line shape and intensity of the calculated Raman polarizability tensor.[187] Such system-bath interactions can be incorporated using a density matrix approach pioneered by Mukamel and coworkers[187]. In this approach the

spontaneous emission from an excited electronic state is calculated by assuming that the electronic degrees of freedom are coupled to a bath of vibrational degrees of freedom, representing the nuclear dynamics of the system. The effect of the system-bath interactions is to broaden the emission lineshape through static and dynamic homogeneous and inhomogeneous broadening mechanisms. In Raman scattering, these are incorporated into the differential scattering cross section in the Condon ('A' term) approximation as[188]

$$\left(\frac{d\sigma_{\rho\sigma}}{d\Omega}_{i,j}\right)_{Raman} = \frac{(\mu_\rho)^0_{g,e}(\mu_\sigma)^0_{e,g}\omega_L\omega_s^3}{(4\pi\epsilon_0)^2\hbar^2c^4}\sum_i P_i \int d\delta G(\delta) \times \left|\int_0^\infty dt\, \langle j|i(t)\rangle \exp[i(\omega_L + \omega_{gi} - \delta)t - g_h(t)]\right|^2 \tag{3.27}$$

In equation 3.27, P_i is the Boltzmann population of state |i> and G(δ) is a function describing the inhomogeneous distribution of shifts, δ, in the purely electronic 0-0 transition. The function $g_h(t)$ is an electronic dephasing term that represents homogeneous broadening due to the other unaccounted degrees of freedom acting on the excited state wave packet that are not included in the model. The functional form of $g_h(t)$ is modelled usually using the Brownian oscillator model. Each unaccounted degree of freedom in the bath is treated as an overdamped oscillator coupled to the electronic surface with a specific coupling strength, frequency, and frictional term.[176,187] $g_h(t)$ is modelled as[187]

$$g_h(t) = g'(t) + ig''(t) \tag{3.28}$$

$$g''(t) = -(\lambda/\Lambda)[\exp(-\Lambda t) + \Lambda t - 1] \tag{3.29}$$

$$g'(t) = \left(\frac{\lambda}{\Lambda}\right)\cot\left(\frac{\hbar\Lambda}{2k_bT}\right)[\exp(-\Lambda t) + \Lambda t - 1]$$

$$+ \frac{4\lambda\Lambda k_bT}{\hbar}\sum_{n=1}^{\infty}\frac{\exp(-v_nt) + v_nt - 1}{v_n(v_n^2 - \Lambda^2)} \tag{3.30}$$

$$v_n \equiv \frac{2\pi k_bT}{\hbar}n$$

λ is the reorganization energy of the collective oscillator and Λ is its timescale. Λ is related to the frequency of the Brownian oscillator mode, ω_{BO}, and the frictional term, ϒ, as $\Lambda = \omega_{BO}^2/\Upsilon$. Specific displaced low frequency modes can be added to the bath as well by adding the following term to g_h.

$$g_{vib}(t) = \sum_j \frac{\Delta_j^2\omega_j^2}{2}\left[\coth\left(\frac{\hbar\omega_j}{2k_bT}\right)\left[1 - \cos(\omega_j t)\right] + i(\sin(\omega_j t) - \omega_j t)\right] \tag{3.31}$$

With all these parameters in place, the dispersion of the Raman differential cross section for resonant Raman transitions can be calculated and compared to experiment.

As will be presented in section 3.7, there is a similar formula for the absorption scattering cross section as that of the Raman cross section. In applying the time dependent model to real systems, uniqueness of the parameters to model the resonance Raman cross sections of the many observed phonons is an issue. In the Franck-Condon approximation of resonance Raman there are really only five free floating parameters; the dipole transition length, the 0-0 transition frequency, the homogeneous and inhomogeneous linewidth, and the displacement of one phonon. The displacements of all other phonons are constrained by the ratio of absolute Raman cross sections to that one phonon. By simultaneously fitting the observed resonance Raman and the absorption spectra the number of parameters is highly constrained. The Franck-Condon progressions observed in the absorption spectrum can help pin down the final phonon

displacement. Also, the absorption spectrum defines the dipole transition length and 0-0 frequency. The final two parameters, homogeneous and inhomogeneous broadening, are constrained by the absolute resonance Raman cross sections, since the absorption spectrum cannot tell the difference between the two parameters. Taken all together, applying this model to the resonance Raman and absorption spectra can yield accurate information on the excited state structure of a material.

3.5 Light scattering

In a typical light scattering experiment, the differential scattering cross section is the relevant experimental parameter. It is defined as the ratio between the scattered power per unit solid angle, P_s (Ws^{-1}) and the incident intensity, I_I ($W^2m^{-2}s^{-1}$).

$$\frac{d\sigma_{Tot}}{d\Omega} = N * \frac{d\sigma_v}{d\Omega} = \frac{dP_s/d\Omega}{I_I} \tag{3.32}$$

A detector will collect a signal that is proportional to the total differential cross section (units: $[m^2Sr^{-1}]$) of a particular Raman transition of the material. N is the number of scattering centers of volume v each with differential cross section $d\sigma_v/d\Omega$. A standard back-scattering arrangement is displayed in Figure 3.4.

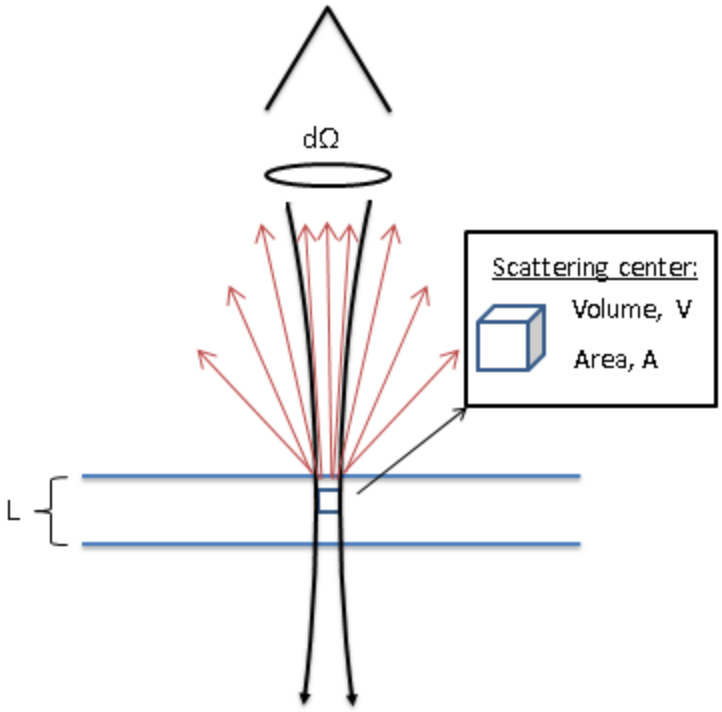

Figure 3.4: Back-scattering light configuration: L is the scattering length in the material, dΩ is the solid angle of the detector. The red arrows are the scattered light from the scattering center, and the black arrows are the incident light.

Light incident on the material will be focused usually via a microscope objective of numerical aperture NA. The scattered light will then be collected by the same objective and sent to a spectrometer/detector system by a dichroic beam splitter. Only a portion of the scattered light will make it to the detector. The light imaged by the detector system will correspond physically to scattered light from a volume of the sample known as the scattering volume, V_{tot}, of scattering length L. This volume is composed of smaller volumes called scattering centers that correspond to the microscopic entities that scatter the light e.g. atoms, molecules, formula units, or unit cells. The differential cross section, $d\sigma_v/d\Omega$, of equation 3.32 is usually made in reference to the relevant scattering center of the system under inspection.

3.6 Absolute Raman scattering

In order to properly compare calculated Raman cross sections as a function of frequency with experimental cross sections, absolute cross sections are needed. Raman absolute cross sections are very finicky objects. There are many factors that will affect the detection of the intensity of the Raman transition, especially for anisotropic solids. First, all of the optics, the gratings, and the detector used in a typical Raman set-up have frequency- and polarization-dependent responses. Second, the Raman cross section of the material is also dependent on the frequency and polarization of the incident light. In addition, the material has frequency-dependent parameters, such as reflection and absorption coefficients, that will influence the amount of scattered light that reaches the detector. The surface smoothness can also affect the amount of detected radiation. Finally, the power of the incident radiation, spot size, and detector acquisition time will also impact the Raman cross section and will become important when comparing with results obtained with other incident frequencies. In order to tackle this problem, the substitution method[189] is used. The entire method hinges on the fact that the scattering cross section and Raman scattering tensors for diamond, calcium fluoride, rutile, and various other 'standards' have been painstakingly measured using techniques such as a combined Brillouin-Raman scattering efficiency comparison[190,191]. In the Raman spectroscopy experiment, a scattering rate 'R_s' (photons/sec) from the sample under inspection is measured. This scattering rate is due to a contribution of a number of geometrical and material factors as stated above. The general equation for R_s including these factors is as follows[192]

$$R_s = \frac{dS_{\alpha\beta}}{d\Omega} * P_{i\beta}(\omega_i) * \Omega_s * D(\omega_s) * T(\omega_i, \omega_s) \tag{3.33}$$

Terms in equation 3.33 are the incident power of polarization β, $P_{iβ}$, the solid angle inside the sample that reaches the detector, Ω_s, the detector efficiency $D(\omega_s)$ at the scattered photon

frequency, ω_s, and a function $T(\omega_i, \omega_s)$ describing the effect of the reflection and absorption constants of the material at the incident and scattered frequencies, ω_i and ω_s. $S_{\alpha\beta}$ is the Raman scattering efficiency (1/length) of the sample connecting incident polarization β with scattered polarization α. The Raman scattering efficiency, used for solids, is defined as the differential cross section ($d\sigma_v$), as defined in equation 3.32, multiplied by the volume of the scattering center. This definition has the advantage of not being made in reference to any volume and is just the ratio between scattered and incident power for a unit path length in the solid.[189] Thus, in order to determine the total scattering efficiency, the Raman scattering efficiency is just multiplied by the scattering length, L, as shown in Figure 3.4. In the substitution method, a material of known Raman scattering efficiency is measured under the same experimental conditions as the sample and the ratio of its signal to that of the sample is used to extract the Raman scattering efficiency of the sample and then the differential cross section. Many factors like the incident power, detection solid angle, detector acquisition time, and the response of entrance and exit optics are factored out using this method. Also, only relative changes in detector and grating efficiency are needed between the frequency of the scattered photons of the sample and standard, rather than an absolute calibration of those elements. The function $T(\omega_i, \omega_s)$ can be formulated in a number of limiting cases[192]

$$T(\omega_i, \omega_s) = (1 - R_i)(1 - R_s)\frac{\left(1 - e^{-(\alpha_i + \alpha_s)L}\right)}{\alpha_i + \alpha_s}; General\ Case \tag{3.34}$$

$$T(\omega_i, \omega_s) = (1 - R_i)(1 - R_s)L; Transparant\ Material \tag{3.35}$$

$$T(\omega_i, \omega_s) = \frac{(1 - R_i)(1 - R_s)}{\alpha_i + \alpha_s}; Opaque\ Material \tag{3.36}$$

$R_{i,s}$ and $\alpha_{i,s}$ are the reflection and absorption coefficients of the material. The limiting cases are usually chosen with respect to a ratio of the scattering length, L, to the absorption coefficients. If

$\alpha_{i,s}L$ <<1 then the transparent case is chosen, and if $\alpha_{i,s}L$>>1 then the opaque case is chosen. For a transparent material, L is chosen to be the depth of focus of the collecting lens. For simplicity, if the depth of focus is much larger than $1/(2\alpha_{i,s})$, then the opaque limiting case is a good approximation. The function describing relative changes in detector efficiency versus frequency, $D(\omega_s)$, was determined using a NIST calibrated Tungsten halogen lamp. Descriptions of this procedure are presented in the following references[193,194].

3.6.1 Experimental set-up

The Raman experiments in this project were completed using two different spectrometers. Data below a Raman shift of 100 cm^{-1} and the entire APMDA experiment were completed using the DilorXY triple-axis spectrometer, manufactured by Jobin-Yvon, outfitted with a liquid nitrogen cooled CCD (charge coupled device) detector. Raman scattered light is collected in a back-scattering configuration using an attached microscope. The spectrometer was operated in subtractive mode. In subtractive mode, the first two of the three gratings act as a band pass filter to eliminate stray light, such as the Rayleigh scattered light, yet still allow for a rather wide field of view. The resolution is the same as that which would be attained by a double spectrometer operating in additive mode, approximately ~1 cm^{-1}. In the APMDA experiment the crystals were cooled to 80 K using a MMR Technologies Joule-Thomson refrigerator. The crystals rest on the sample mount of the fridge under a vacuum of ~10^{-6} Torr. The vacuum was achieved by using a roughing and diffusion pump combination. Due to their small relative size, the crystals were electrostatically attracted to the fridge mount and did not necessarily require any added adhesive; however a speck of vacuum grease was attached to one corner of each crystal. Due to their small relative size and mass compared to the fridge mount, thermal equilibrium of the crystals was quickly achieved with changes in temperature of the fridge. This

was monitored by observing the Raman spectrum as a function of time. Polarization of the incident and scattered light was controlled via entrance and exit linear polarizers. In measurements of APMDA, the c-axis of the crystal was aligned with the polarization of the incident and scattered light. This spectrometer system has two lasers coupled to it via entrance optics, 1) a Coherent Genesis CX 532 nm solid state laser and 2) a Spectra-Physics 375b dye laser. The dye laser was pumped with the Coherent laser and Rhodamine 6G was used as the dye with a tuning range of 560-640 nm using a birefringent filter. The light was focused using one of two microscope objectives. For room temperature measurements, a 100X objective with a numerical of aperture (NA) of 0.95 was used resulting in a spot size of ~1 micron. Temperature dependent measurements used a 32X objective with an NA of 0.3 resulting in a spot size of ~10 microns. Power of the incident radiation was controlled with a series of neutral density filters. The power of the incident radiation and the acquisition time of the CCD were chosen to achieve the best signal-to-noise ratio possible in a reasonable amount of time without burning the sample. Typical laser powers prior to entrance into the microscope objective were on the order of a few milliwatts. A scan consisted of multiple acquisitions averaged together, where each acquisition time was around one minute. The frequency response of the spectrometer was calibrated using the calibrated emission spectrum of a solution of Kiton red dye at 532 nm. This emission spectrum was obtained from the Renishaw spectrometer system (described below), which was calibrated with the NIST calibrated tungsten halogen lamp under 514 nm excitation.

The other Raman spectrometer set-up used in this work consisted of a Renishaw Invia Confocal Raman microscope with five laser wavelengths provided by three lasers: a Spectra-Physics Stabilite 2017 argon-ion laser (457, 488, and 514 nm), a Renishaw HeNe 633 nm laser, and a Renishaw NIR 785 nm laser. The Renishaw spectrometer employed a single removable

diffraction grating. The grating was selected based on the wavelength of the laser used. A grating with a groove density of 2400 lines/mm was used for 457 and 488 nm excitation wavelengths, 1800 lines/mm for 514 and 633 nm, and 1200 lines/mm for 785 nm. With only a single grating stray light scatter, including Rayleigh scattering is diffracted along with the Raman scattering. This prevents the CCD detector from properly observing a Raman spectrum without saturation from Rayleigh scattering. Therefore, a set of Rayleigh filters are used to prevent any Rayleigh scattering from reaching the detector. The Raman shift cut-off for these filters is around 100 cm^{-1}. A 50X microscope objective with an NA of 0.75 was used for the room temperature measurements completed on the PnT1 materials. A rotation stage was installed to adjust the orientation of the single crystals relative to the direction of polarization of the incident light. The PnT1 crystals rested on glass slides with no added adhesive. Similar acquisition times and powers were used in the PnT1 experiment as the APMDA experiment. A depolarizer was installed just before the entrance slit to the spectrometer in the Renishaw system to negate the effect of any polarization dependence of the diffraction grating. The depolarizer was necessary because the frequency response of the spectrometer was calibrated with unpolarized light.

3.7 Optical absorption

3.7.1 Theory and time-dependent formalism

Optical absorption is a one-photon process, as opposed to Raman scattering, which is a two-photon process. In optical absorption, a photon incident on a material of interest is absorbed by the material at a frequency coincident with the frequency of a symmetry-allowed electronic transition. The discussion of this section closely mirrors that of the Raman scattering, therefore it will be greatly compacted for the sake of simplicity. Using first-order time-dependent

perturbation theory, where the coupling of the incident electric field with the transition dipole of the material acts as the perturbation, a sum over states model for optical absorption is derived.[170]

$$\sigma_{g,e}(\omega) = \frac{\pi\omega}{\epsilon_0 \hbar c n} \sum_i P_i \sum_v \left| \mathcal{E}^* \cdot \mu(Q))_{ev,gi} \right|^2 \left[\frac{\Gamma/\pi}{(\omega_{ev,gi} - \omega)^2 + \Gamma^2} \right] \tag{3.37}$$

The model for optical absorption, equation 3.37, is between two electronic states, g and e, and describes the observed optical absorption spectra as a superposition of Lorentzian line shapes representing various vibronic transitions between the two separated electronic states. The selection rule for optical absorption is that the permanent dipole moment $\mu_{ev,gi}$ must exist. Recasting equation 3.14 here for convenience, the following selection rule can be made to see what kind of transitions can occur.

$$(\mu_\rho(Q))_{gi,ev} = \langle v | \langle e | \hat{\mu}_\rho(Q) | g \rangle | i \rangle \tag{3.14}$$

$$\Gamma_1 \subset (\Gamma_i \otimes \Gamma_g) \otimes \Gamma_\mu \otimes (\Gamma_e \otimes \Gamma_v) \tag{3.38}$$

The irreducible representation for Γ_μ is the same as that for the coordinates x, y, and z. Similar to the selection rules for Raman scattering, if the fully symmetric irreducible representation, Γ_1, is contained in the direct product of the vibronic states with the dipole transition moment then that transition will be allowed. From equation 3.38, considering a transition between the two electronic states g and e, purely electronic absorptions i.e. ones without vibronic coupling, cannot have the same irreducible representation. The transition dipole moment can be expanded in a Taylor series along phonon normal coordinates Q, to give the Condon approximation, in a manner similar to the 'A' term of resonance Raman scattering.

$$\sigma_{\rho_{g,e}}(\omega) = \frac{\pi\omega \left| (\mu_\rho)^0_{g,e} \right|^2}{\epsilon_0 \hbar c n} \sum_i P_i \sum_v \frac{|\langle v|i \rangle|^2 \Gamma/\pi}{(\omega_{ev,gi} - \omega)^2 + \Gamma^2} \tag{3.39}$$

In equation 3.39, the projection along the molecular or crystal axis ρ has been taken. In the same manner as for Raman scattering, a time-dependent approach can be applied to the sum over states model for optical absorption including system-bath interactions as well. Applying the same technique as from the section 3.4, the following time dependent absorption equation is obtained.[188]

$$\sigma_{\rho_{g,e}}(\omega) = \frac{\pi\omega\left|(\mu_\rho)^0_{g,e}\right|^2}{\epsilon_0\hbar cn}\sum_i P_i \int d\delta G(\delta) \times \int_{-\infty}^{\infty} dt \,\langle i|i(t)\rangle \exp[i(\omega + \omega_{gi} - \delta)t - g_h(t)] \tag{3.40}$$

In comparing this equation with equation 3.27 for resonance Raman scattering there are two important differences. One is that the integral is now a full Fourier transform, where in the Raman picture it was the square of a half Fourier transform. The other major difference is that the overlap integral is now an overlap between |i(t)> with the initial vibrational state, |i>, rather than the one vibrational quantum different state of |f> in normal Raman scattering. In both pictures, there is no reference to excited state vibrational eigenstates.

In the same vein of resonant Raman scattering in the limit of pre-resonance or short-time dynamics, a simple relation can be made between the optical absorption spectrum and the slope of the excited state potential surface.[172]

$$2\sigma^2 = \sum_k \Delta_k^2 \omega_k^2 \tag{3.41}$$

σ is the standard deviation of a Gaussian line shape assumed for the optical absorption spectrum of a transition to one excited electronic state. The index k refers to the vibrational modes observed in the resonance Raman spectrum. This equation coupled with the short-time dynamics

resonant Raman equation 3.26 gives the proper constraint needed to make a simple estimate of the excited state displacements. All that is needed to make the estimate are the bandwidth of the electronic transition, the relative resonant Raman intensities, and their frequencies. As this model is a local model describing mainly high frequency resonant modes, it will tend to overestimate the excited state displacements of the lower frequency observed resonant modes.[184]

In general for organic semiconductor molecular crystals, the optical absorption spectra are broad and any underlying vibronic structure is difficult to resolve. Armed with just the absorption spectrum, it is nearly impossible to apply the model of equation 3.40 and extract useful numbers about the excited state potential surface (e.g. Δ_k, ω_e) and the broadening mechanisms. Simultaneously fitting both the absorption and resonance absolute Raman excitation spectra however puts the proper constraints on the transition moment, homogeneous broadening, and excited state parameters used in the models. The fitting of the resonance Raman excitation profiles feeds the absorption model with the proper excited state parameters, while fitting of the absorption spectra constrains the transition dipole moment. Also, the absolute Raman excitation profiles are needed so one can properly distinguish between homogeneous and inhomogeneous broadening.[195]

3.7.2 Experimental set-up

A typical absorption experiment is diagrammed in Figure 3.5.

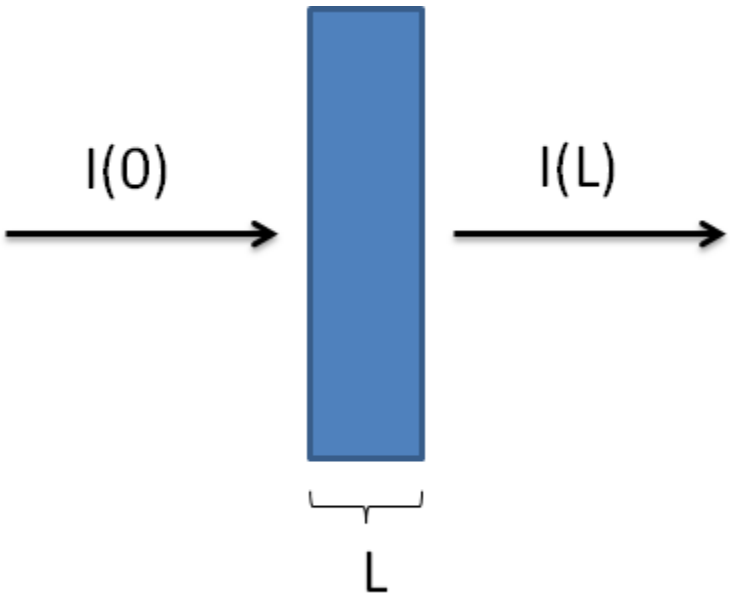

Figure 3.5: An optical absorption experiment on a slab of material of thickness L. I(0) is the intensity of light right before it hits the material and I(L) is the intensity after it has passed through the material.

A Beer-Lambert law is used to describe the attenuation of the incident radiation normal to the plane of the sample.[170]

$$\frac{I(\omega, L)}{I(\omega, 0)} = e^{-\sigma NL} \tag{3.42}$$

I(ω,0) is the initial intensity of the incident radiation before it enters the sample and I(ω,L) is the intensity of the radiation after passing through the sample. σ is absorption cross section, L is the length of the sample the light travels through and N is the density of absorbers, which in the case of a molecular solid would either be the density of unit cells or the density of a certain molecule depending on the nature of the electronic transition under inspection.

In this project, optical absorption spectra of PnT1, APMDA, and their parent molecular crystals, perylene, TCNQ, anthracene, and PMDA, were taken using a UV-Visible-NIR absorption spectrophotometer (Varian Instruments, model: Cary 400). The Cary 400 works using a double beam configuration, where one beam travels through the sample and the other, a

reference beam, travels through a sample blank. For instance, if the crystal is mounted on a glass slide, then a blank glass slide would be in the sample blank beam. The instrument operates by using a Tungsten lamp whose light is fed into a double monochromator that selects a wavelength with a bandwidth of ~1 nm; that light is then split into two beams which correspond to the sample and reference beams. A chopper is placed before the detector to selectively measure the sample beam and the reference beam and create the intensity ratio of equation 3.42. Because the single crystals in this project are thick, single crystal absorption spectra are nearly impossible with the Cary 400 system. To combat this shortcoming, a crystal was taken and crushed onto the sticky side of a one-sided piece of scotch tape using a razor blade. The crushed area was around 1 cm^2. Using this method, a thinner and wider sample was achieved at the expense of gaining any polarization-dependent absorption measurements of the sample. These crushed samples were then measured with a blank piece of scotch tape as the reference.

3.8 Raman selection rules

The following diagrams are the Raman selection rules for PnT1 and APMDA. These were derived using well known methods of group theory; the reader is recommended to read these references[196,197] , if interested in the derivation of the rules.

3.8.1 P1T1:

Table 3.1: Raman selection Rules for perylene modes in P1T1

Raman Selection Rules: Perylene in P1T1				
Molecular Group (D_{2h})		Site Group (C_i)	Factor Group (C_{2h})	
Degrees of Freedom	Species		Species	Degrees of freedom
16	a_g	a_g	A_g	48 (3 lib.)
$6+R_z$	b_{1g}			
$8+R_y$	b_{2g}		B_g	48 (3 lib.)
$15+R_x$	b_{3g}			

Table 3.2: Raman selection rules for TCNQ in P1T1

Raman Selection Rules: TCNQ in P1T1				
Molecular Group (D_{2h})		Site Group (C_i)	Factor Group (C_{2h})	
Degrees of Freedom	Species		Species	Degrees of freedom
10	a_g	a_g	A_g	30 (3 lib.)
$3+R_z$	b_{1g}			
$5+R_y$	b_{2g}		B_g	30 (3 lib.)
$9+R_x$	b_{3g}			

3.8.2 P2T1:

Table 3.3: Raman selection rules for perylene modes in P2T1

Raman Selection Rules: C_i Perylene in P2T1				
Molecular Group (D_{2h})		Site Group (C_i)	Factor Group (C_i)	
Degrees of Freedom	Species		Species	Degrees of freedom
16	a_g	a_g	A_g	96 (6 lib.)
$6+R_z$	b_{1g}			
$8+R_y$	b_{2g}			
$15+R_x$	b_{3g}			

Table 3.4: Raman selection rules for TCNQ in P2T1

Raman Selection Rules: TCNQ in P2T1				
Molecular Group (D_{2h})		Site Group (C_i)	Factor Group (C_i)	
Degrees of Freedom	Species		Species	Degrees of freedom
10	a_g	a_g	A_g	30 (3 lib.)
$3+R_z$	b_{1g}			
$5+R_y$	b_{2g}			
$9+R_x$	b_{3g}			

3.8.3 P3T1:

Table 3.5: Raman selection rules for perylene of site symmetry C_i in P3T1

Raman Selection Rules: C_i Perylene in P3T1				
Molecular Group (D_{2h})		Site Group (C_i)	Factor Group (C_i)	
Degrees of Freedom	Species		Species	Degrees of freedom
16	a_g	a_g	A_g	48 (3 lib.)
$6+R_z$	b_{1g}			
$8+R_y$	b_{2g}			
$15+R_x$	b_{3g}			

Table 3.6: Raman selection rules for TCNQ in P3T1

Raman Selection Rules: C_i TCNQ in P3T1				
Molecular Group (D_{2h})		Site Group (C_i)	Factor Group (C_i)	
Degrees of Freedom	Species		Species	Degrees of freedom
10	a_g	a_g	A_g	30 (3 lib.)
$3+R_z$	b_{1g}			
$5+R_y$	b_{2g}			
$9+R_x$	b_{3g}			

Table 3.7: Raman selection rules for perylene of site symmetry C_1 in P3T1

Raman Selection Rules: C_1 Perylene in P3T1				
Molecular Group (D_{2h})		Site Group (C_1)	Factor Group (C_i)	
Degrees of Freedom	Species		Species	Degrees of freedom
16	a_g	a	A_g	96 (3 lib. + 3 trans)
$6+R_z$	b_{1g}			
$8+R_y$	b_{2g}			
$15+R_x$	b_{3g}			

3.8.4 APMDA:

Table 3.8: Raman selection rules for anthracene in APMDA

Raman Selection Rules: C_i Anthracene in APMDA				
Molecular Group (D_{2h})		Site Group (C_i)	Factor Group (C_i)	
Degrees of Freedom	Species		Species	Degrees of freedom
12	a_g	a_g	A_g	36 (3 lib.)
$6+R_z$	b_{1g}			
$4+R_y$	b_{2g}			
$11+R_x$	b_{3g}			

Table 3.9: Raman selection rules for PMDA in APMDA

Raman Selection Rules: C_i PMDA in APMDA				
Molecular Group (D_{2h})		Site Group (C_i)	Factor Group (C_i)	
Degrees of Freedom	Species		Species	Degrees of freedom
9	a_g	a_g	A_g	27 (3 lib.)
$4+R_z$	b_{1g}			
$3+R_y$	b_{2g}			
$18+R_x$	b_{3g}			

The preceding tables are called correlation tables. The Raman active modes and their respective symmetries are listed on the left for the molecular Raman case. Then these modes are correlated into the symmetry of the site where the molecule resides in the unit cell, whose symmetry the molecule adopts. Following this the site symmetry is correlated into the factor group of the crystal so that it will possess the translational symmetry elements of the crystal, such as translations, glides, and screw operations. The column "degrees of freedom" refers to the vibrational degrees of freedom of the species' irreducible representation.

CHAPTER 4: PERYLENE$_n$-TCNQ

4.1 Introduction

As mentioned in chapter two, many of the electronic and optical properties of P3T1 and P1T1 have been studied both experimentally and theoretically using a variety of methods. However, prior to this project, important parameters for charge transport such as the degree of CT and electron-phonon coupling have not yet been investigated experimentally and theoretically. In addition, the inclusion of the third, recently-discovered material P2T1 adds a link between P1T1 and P3T1 that allows the further elucidation of the effect of structure on the optical and electrical characteristics of the PnT1 system. This is the aim of the chapter, which will present the optical, electrical, and computational results produced by the present study of the PnT1 system. This chapter begins with a presentation on the relevant optical, electrical, and vibrational properties measured in this study for PnT1 in order to provide a sufficient basis for the following study on the degree of charge transfer and local electron-phonon coupling in PnT1.

4.2 Background

4.2.1 Opto-electronic properties

A brief discussion of the optical-electronic spectra of P1T1 and P3T1 was completed in chapter 2. An extension to that discussion will be made here in light of additional experimental measurements our collaborators and I made. Figure 4.1 displays the unpolarized powder UV-Vis-NIR absorption spectra of P1T1 and P3T1. This measurement was not attempted on P2T1, due to the very limited supply of the P2T1 material available. The two spectra are very similar in

that they display prominent absorption bands from 350-450nm and additional broad absorption bands with a maximum close to 950nm. As described elsewhere[145,146,149,150], when comparing these absorption spectra to those of the parent molecules (either perylene or TCNQ), it becomes clear that the prominent absorption bands from 350-450nm belong to the molecular excitons of the parent molecules, as shown in Figure 4.2 for P3T1. The shoulder at 500nm in both compounds is only visible in the complex and not in the absorption spectrum of either perylene or TCNQ. The lowest-lying observed and calculated neutral TCNQ molecular exciton is at 442nm[198,199], which rules out neutral TCNQ as a cause for this transition. As for perylene, the lowest excited electronic transition is at 476nm[200]. This absorption is most probably a higher-energy CT state or a mixed state of perylene and TCNQ excitons. The broad absorption in the NIR with a maximum near 950 nm in both compounds is identified as a CT transition because of its polarization along the molecular stacking axis, as well as its similarity to CT transitions in other CT compounds[145,149].

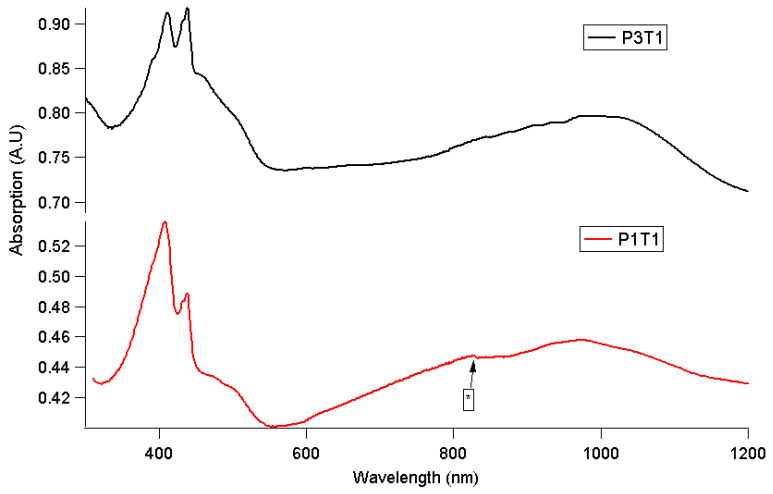

Figure 4.1: Unpolarized powder electronic absorption spectra of P1T1 and P3T1. '*' is an experimental relic from a changeover of an optical filter.

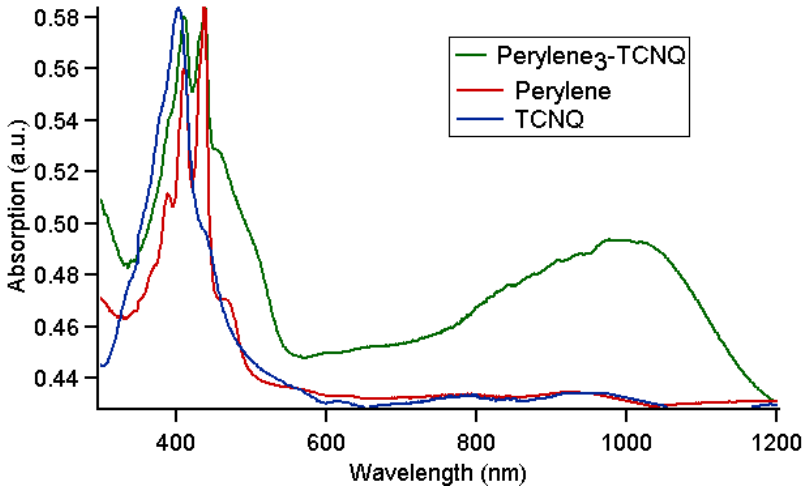

Figure 4.2: Unpolarized powder electronic absorption spectra of P3T1, perylene, and TCNQ.

4.2.2 Electronic properties

The electrical characteristics of PnT1 were measured by our collaborators, Dr. Jurchescu and her group from Wake Forest University, according to the procedure described in reference[63]. They created organic field effect transistors from the crystals. Due to their thin, platelet-like geometry, P2T1 and P3T1 were most amenable to a bottom-gate, bottom-contact device architecture, where the crystals can be laminated to their test beds and adhere electrostatically to the dielectric surface. For P1T1, because of its thickness and needle-like geometry, a bottom-gate, top-contact device architecture was employed. Their results are displayed in Figure 4.3.

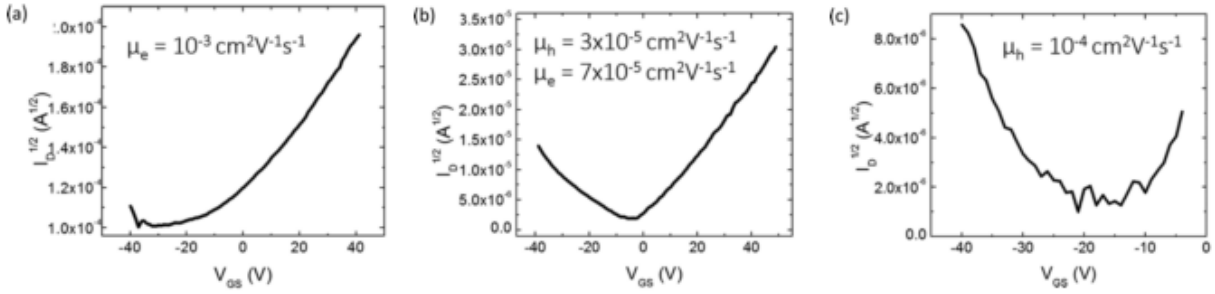

Figure 4.3: Electrical characteristics of PnT1 at 300K a) electron-only transport in P1T1 b) ambipolar transport in P2T1 and c) hole-only transport in P3T1. Adapted from ref.[63]

All measured moblities are very low. Interestingly, each compound exhibits a different type of transport behavior. P1T1 has electron-only transport, P2T1 has ambipolar transport, and P3T1 has hole-only transport.

4.2.3 Vibrational properties

Our group's measurements on the basic vibrational properties of PnT1 are presented here to familiarize the reader with the many phonons that will become important when discussing electron-phonon coupling. The vibrational spectra of PnT1 can be split into two regimes, an intramolecular (high frequency) and an intermolecular (low frequency) regime. PnT1 vibrational spectra are similar among the three compounds in the intramolecular regime, yet due to differences in crystal structure they are much different in the intermolecular regime. Spectra in the intermolecular regime provide a unique fingerprint that allows the identification of a given PnT1 compound. Low frequency (<200cm^{-1}) polarized Raman spectra of the three compounds along two different polarization directions are compared in Figure 4.4.

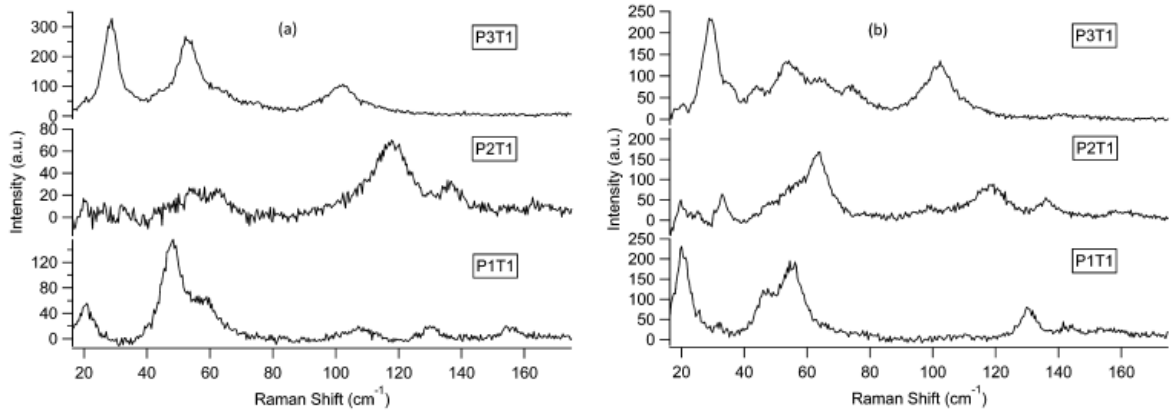

Figure 4.4: Raman spectra of P1T1, P2T1, and P3T1 in the low-frequency range: a) incident and scattered electric field parallel to the molecular stacking axis and b) incident and scattered electric field perpendicular to the stacking axis.

Each spectrum was measured at room temperature with the incident and scattered electric field coincident with or perpendicular to the molecular stacking axis of the PnT1 sample. The Raman spectra of these three crystals are very different in this frequency range, reflecting the fact that the low-frequency phonons are either of intermolecular nature, or are hybrids of intermolecular and low-frequency intramolecular vibrations. Consequentially, each spectrum is unique to the specific crystal structure and can be used to identify the crystal stoichiometry. Raman selection rules dictate that 12 (all librations), 9 (all librations), and 12 (9 librations plus 3 translations) intermolecular phonons are Raman active in P1T1, P2T1, and P3T1 respectively. Not every expected intermolecular phonon was observed in the compounds, due either to scattering geometry, the overlapping of near-degenerate librations, or low Raman activity. The separation between intermolecular and intramolecular regimes is supported by DFT calculations[63] of isolated molecules which indicate that all the intramolecular phonons of perylene and TCNQ located below 200 cm^{-1} show marginal or no Raman activity. The Raman spectra above 200 cm^{-1} are very similar among the three compounds with only minor shifts (<5 cm^{-1}) in frequency of corresponding phonons. Similarities in the high-frequency spectra stem from the van der Waals nature of the CT compounds. Differences in intensity among corresponding peaks in in the high frequency spectra of the three compounds is a result of differences in crystal structure resulting in differences in the relative orientations of the incident and scattered electric field with respect to the orientations of the molecules. There are shifts in frequency of particular phonons between the compounds due to either changes in solid state environment or charge transfer effect, as will be discussed in section 4.3.1.

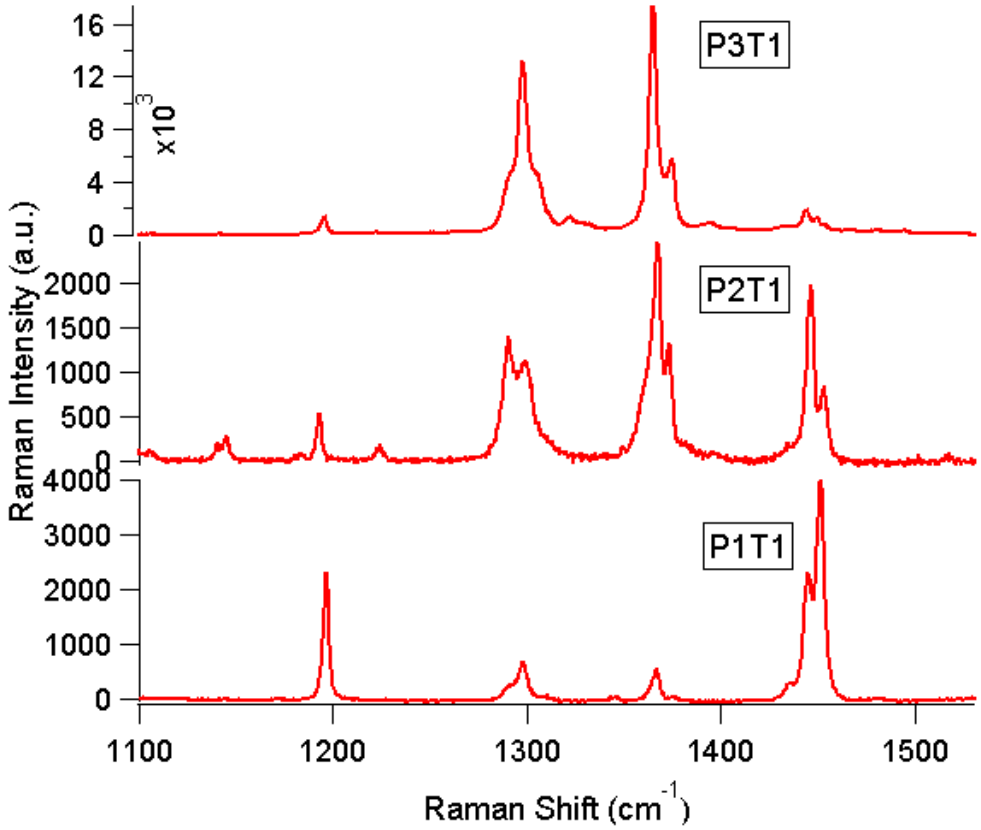

Figure 4.5: Raman spectra of PnT1 with electric field coincident with the molecular stacking axis in the high frequency regime at 532nm excitation.

The frequencies of the low-frequency intermolecular phonons in PnT1 display significant shifts to higher frequency as the temperature is decreased from 300K to 80K, as shown in Figure 4.6. However, the intramolecular phonons do not exhibit any significant change in frequency from 300K to 80K. The change in frequency of the intermolecular phonons is a result of large thermal contraction of the unit cell due to weak intermolecular bonding. Furthermore, the smooth and linear change in the frequencies of the intermolecular phonons of the two compounds in Figure 4.6 corresponds to the absence of any structural phase transition in the observed temperature range. The interpretation of the frequency change is that of a contraction of the unit cell as the temperature decreases. This interpretation is corroborated by the XRD measurement

of P1T1 at 150K. At 300K, the unit cell parameters of P1T1 are a=7.32, b=10.88, and c=14.55Å and the unit cell volume is 1159 $Å^3$. However, at 150K the unit cell parameters of P1T1 are a=7.21, b= 10.86, and c=14.49Å and the unit cell volume is 1134 $Å^3$. According to the XRD data, the main contraction is along the a-axis, which is also coincident with the molecular stacking axis. Therefore, as the temperature decreases the intermolecular distance between adjacent molecules also decreases in PnT1.

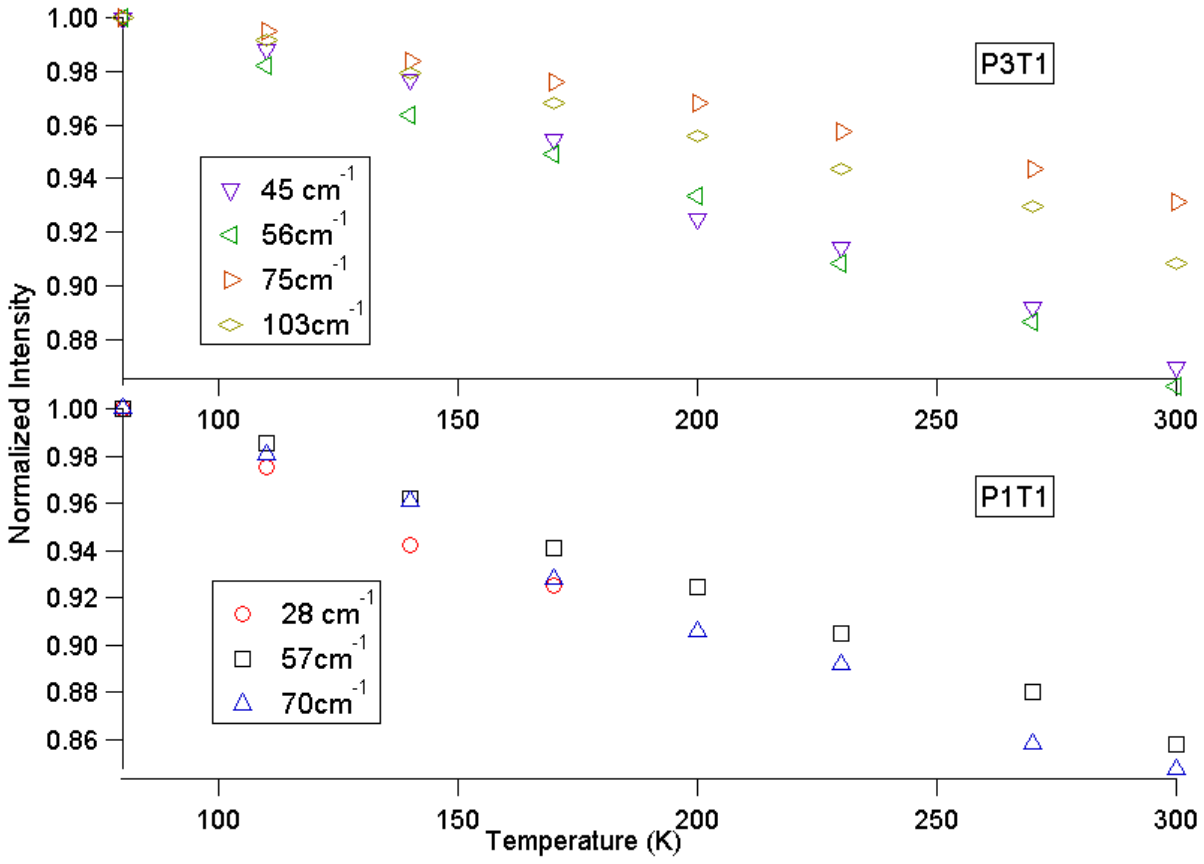

Figure 4.6: Temperature dependence of selected low frequency phonons of P3T1 and P1T1

4.3 Electron-vibrational spectra

With the basic optical, vibrational, and electronic measurements presented, discussion on the effect of structure on the degree of charge transfer and local electron-phonon coupling will ensue.

4.3.1 Degree of charge transfer

As mentioned in the introduction, in the ground state of charge transfer compounds the structure of the constituent molecules is not the same as that of the free molecule. Van der Waals crystal forces will perturb bond lengths and therefore shift phonon frequencies (albeit by <5 cm^{-1}), but CT between the donor and acceptor molecule also changes the equilibrium positions of the atoms composing the molecule. Charge is not necessarily distributed evenly over the molecule and so bond lengths and angles will shift by different amounts. Phonons that involve vibrations along the direction of contraction or expansion of one or more of these bond lengths will shift in frequency as compared to the frequency of the phonon in the neutral molecule. These phonons are termed "charge sensitive" and can be either infrared- or Raman-active. In the high-frequency regime (>200cm^{-1}), there is a charge-sensitive fully symmetric (A_g) phonon of TCNQ located at a frequency of 1454 cm^{-1} in neutral single-crystal TCNQ[201]; this vibration is pictured in Figure 4.7.

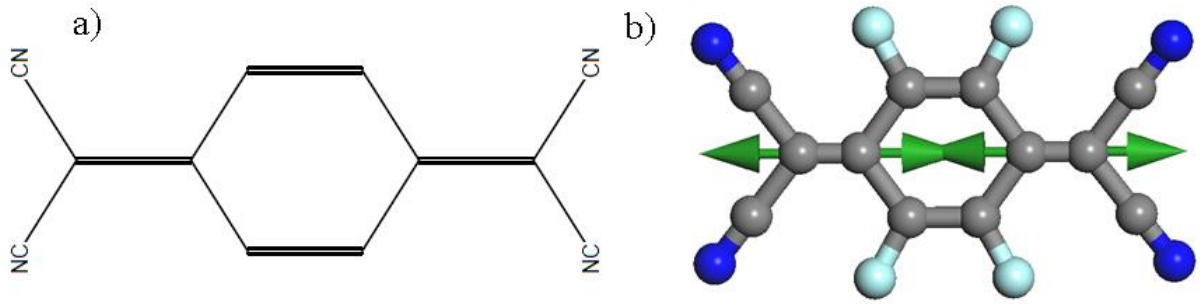

Figure 4.7: a) TCNQ molecule and b) 1454 cm^{-1} C=C stretching phonon of TCNQ: Color scheme: carbon (grey), nitrogen (blue) and hydrogen (light blue).

This phonon has been measured[84,202,203] to linearly downshift by 60 ± 3 cm^{-1} between the neutral TCNQ molecule and the anion, as the result of a decrease in the C-C bond length and an increase in the C=C bond length of the inner quinoid ring as the net charge on the molecule becomes more negative[204,205]. This observation is also supported by DFT calculations by our

collaborators[206]. Figure 4.8 compares the Raman signal of this phonon among the PnT1 compounds. In the CT compounds the 1454 cm^{-1} TCNQ phonon appears as a doublet, a result which is not expected. For P2T1 and P3t1 there is only one TCNQ molecule per unit cell, therefore the doublet is not a result of Davydov splitting[207] which occurs when there are two identical symmetry-inequivalent molecules in the unit cell. Another possibility is that the doublet is a result of mixing and intensity sharing of the 1454 cm^{-1} phonon with that of either a nearby perylene phonon or an overtone of a lower-frequency TCNQ phonon. In neutral single crystal TCNQ the 1454 cm^{-1} phonon is the most intense phonon (has the highest scattering cross section). In this spectral region there are no strong perylene phonons reported to date.[208,209] Therefore, in calculating the degree of charge transfer in PnT1 only the most intense phonon of the doublet was used, because the 1454 cm^{-1} phonon is the most intense in the single crystal spectrum of TCNQ. The results from such a calculation are performed using the following equation

$$\rho = \frac{\omega_{TCNQ^{o}} - \omega_{CT}}{\omega_{TCNQ^{0}} - \omega_{TCNQ^{-1}}} * e \qquad (4.1)$$

In equation 4.1, $\omega_{TCNQ^{o}}$ is the frequency of the 1454 cm^{-1} phonon in neutral TCNQ, $\omega_{TCNQ^{-1}}$ is the frequency of the same phonon in the anion $TCNQ^{-1}$, ω_{CT} is the frequency of that same phonon in the CT compound, in this case PnT1, and 'e' is the electron charge. The results of using equation 4.1 for the degree of CT on the PnT1 system at room temperature are tabulated in Table 4.1, along with the values obtained by comparing the bond lengths derived by X-ray diffraction (XRD) of neutral TCNQ and its anion with that of TCNQ in the CT compound.

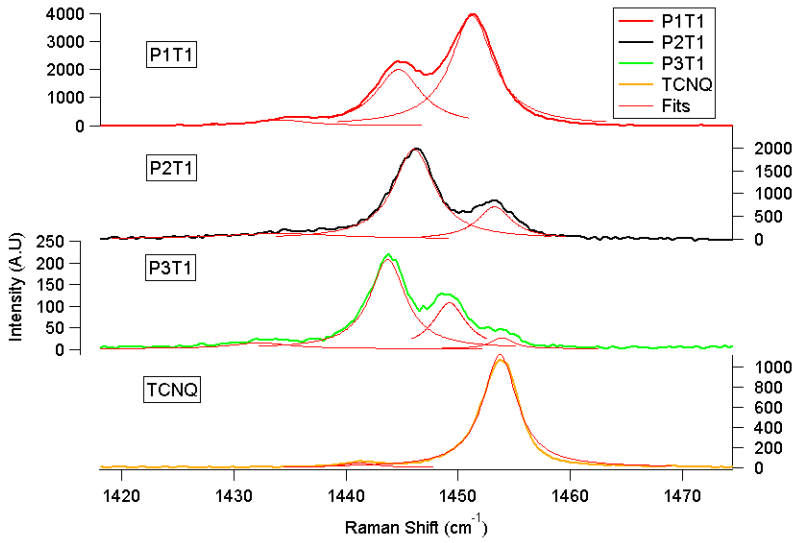

Figure 4.8: Comparison of 1454 cm^{-1} C=C stretching mode between PnT1 and neutral TCNQ. Fits of the above peaks are also shown.

Upon reduction only a few bond lengths in TCNQ are greatly affected. There are two major empirical methods[92,93] for calculating the degree of CT from XRD-derived bond lengths. Both methods rely on ratios of bond lengths of the lengthened C-C bonds and the contracted C=C bonds, and the two give similar values for the degree of CT. Values obtained by the method of Kistenmacher[92] are included in the table, because this method corresponds better with the values for degree of CT obtained using other methods such as diffuse X-ray scattering[94] and arguments based on stoichiometry.

Table 4.1: Charge transfer between perylene and TCNQ in P3T1 at room temperature, estimated from the frequency of the C=C stretching phonon of TCNQ and from bond lengths derived from XRD.

Compound	Mode Freq. (cm^{-1})[a]	Raman CT estimate	Bond length CT estimate
P1T1	1451	0.04 ± 0.02	0.01 ± 0.07
P2T1	1446	0.13 ± 0.02	0.1 ± 0.07
P3T1	1444	0.17 ± 0.02	0.21 ± 0.06
[a]1454 cm^{-1} in neutral TCNQ			

From both Figure 4.8 and Table 4.1 it is clear that the degree of CT increases as the stoichiometry changes from 1:1 to 3:1 and that the two estimates agree with one another. Furthermore, PnT1 is quasi-neutral as a whole, which, in the context of Torrance's work [75] on the neutral to ionic transition (see introduction), means that this system is also semiconducting. At this point it is useful to go over the main effects that determine the degree of CT, in order to understand why the degree of CT changes between the compounds. The CT can be viewed as a delocalization of charge in the ground state. From previous chapters it can be seen that electronic coupling (the transfer integral) between adjacent molecules has a delocalizing effect on the wavefunction of the electron, whereas effects such as electron-phonon coupling tend to have a localizing effect. Another barrier to charge transfer is the site energy difference between neighboring donor and acceptor molecules. Since all of the PnT1 compounds have the same donor and acceptor molecules, the site energy difference is nearly the same for all three. This is also true of the polaron binding energy, which is a measure of the amount of local electron-phonon coupling in the system. The reason the polaron binding energies (i.e. reorganization energies) are similar is that this effect is a local molecular effect and since the molecules are the same chemically it is justified to assume they have similar polaron binding energies. Thus, it seems that changes in the amount of electronic coupling will be the main reason for observed changes in the degree of CT. Our collaborators have used DFT to calculate the electronic coupling in P1T1 and P3T1, and found that the electronic couplings in P1t1 and P3T1 were 375 and 426 meV respectively.[206] Electronic coupling is a function of overlap between the HOMO of the donor and the LUMO of the acceptor. One possible way to increase or decrease overlap is by changing the donor-acceptor distance in PnT1 assuming there is a projection of the overlap along this distance. From XRD measurements of crystal structure[63,141,142] data the mean plane distance

between adjacent donor and acceptor molecules in PnT1 is 3.44, 3.35, and 3.29Å for P1T1, P2T1, and P3T1 respectively. From these measurements it becomes clear that the cause of the change in the degree of charge transfer is the tighter spacing between donor and acceptor molecules as the ratio of perylene to TCNQ molecules increases. This idea is further exemplified in the temperature dependent measurements of the degree of charge transfer for P1T1 and P3T1 in Figure 4.9.

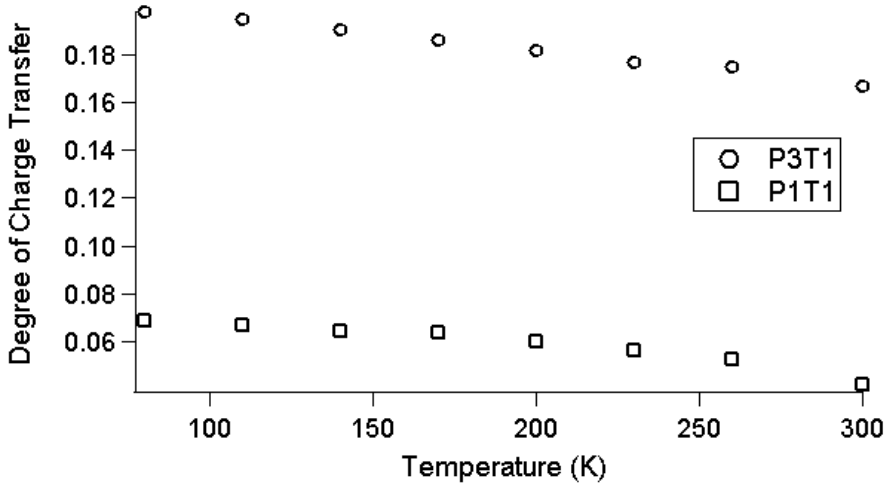

Figure 4.9: Change in charge transfer with temperature from Raman scattering measurements: squares, P1T1; circles, P3T1.

As Figure 4.9 shows, the degree of charge transfer increases as the temperature decreases. This further corroborates our interpretation that it is the donor-acceptor distance that has the most impact in the charge transfer differences between the three compounds. As mentioned above for P1T1, there is a decrease in both the a-axis (molecular stacking axis) and unit cell volume as the temperature is lowered, thus pushing the donor and acceptor molecules closer together. Calculations of the electronic couplings of P1T1 and P3T1 show an increase in coupling as the temperature is lowered; from 375 to 409 meV in P1T1 and 426 to 452 meV in P3T1[63] between 300 and 150K.

4.3.2 Connection to transport

Assuming no electron-phonon coupling and a band-like charge transport model, having a large transfer integral will result in a large charge carrier mobility. P3T1 has a larger degree of charge transfer and transfer integral than P1T1. Applying the band-like mobility concept to PnT1 means that P3T1 will have the largest mobility of the compounds. However, P1T1 has the largest observed mobility, P3T1 the second largest, and P2T1 has the lowest. It is clear that a model based solely on the transfer integral is not sufficient to explain these observed electrical characteristics. Including electron-phonon coupling will be the next step in trying to explain the observed transport characteristics.

4.4 Local electron-phonon coupling

4.4.1 Qualitative aspects of local electron-phonon coupling

We will now shift focus to the study of local electron-phonon coupling in PnT1. As a reminder, local electron-phonon coupling is so named because it is a result of the modulation of the molecular site energy by phonons. Resonance Raman spectroscopy was employed to explore eph coupling in PnT1 both qualitatively and quantitatively. As discussed in the experimental methods chapter, in resonance Raman spectroscopy the excitation energy (i.e. laser frequency) is tuned such that it is coincident with the energy of an electronic transition. Those phonons that are coupled to that electronic transition will experience an increase in their scattering cross sections. In this experiment we excited the PnT1 compounds with excitation energies spanning the range of the visible to the NIR and at two different polarization directions in order to more fully understand eph coupling in PnT1 and the effect structural anisotropy has on it. At each excitation energy the scattering cross sections of the phonons were normalized to the measured cross section of diamond under the same experimental conditions. In this way the effects of differing

experimental conditions, such as laser wavelength, power, detector exposure time, and system alignment, will be accounted for. Furthermore, as mentioned in the experimental methods chapter, this method accounts for the non-material-specific intrinsic frequency dependence of the cross section, the so called ν^4 factor. Finally, the spectrometer was calibrated with a NIST-traceable tungsten-halogen lamp in order to account for any frequency-dependent signal response of the optics, diffraction grating, and CCD. Using this technique Raman scattering cross sections of phonons at one excitation energy can be properly compared to those at another excitation energy devoid of any extrinsic effects such as experimental parameters. Figure 4.10 displays a microscopic diagram of the back-scattering conditions for this resonance Raman experiment.

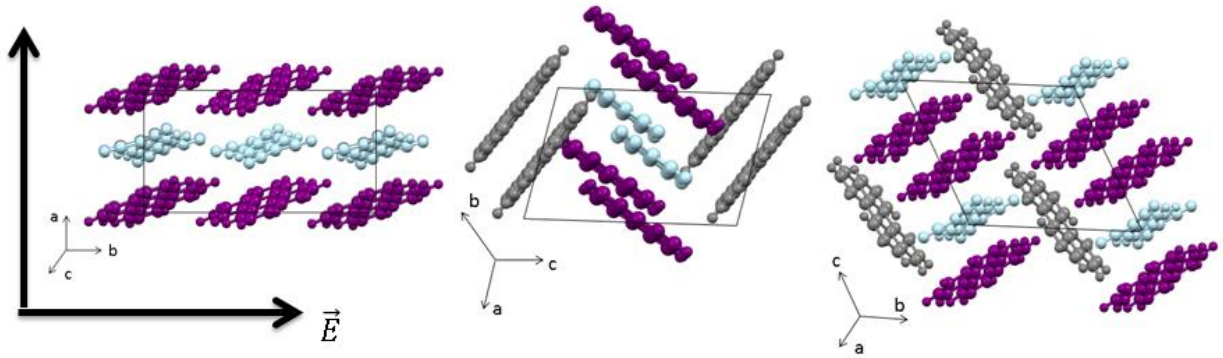

Figure 4.10: Resonance Raman scattering conditions: The incident electric field was polarized parallel and perpendicular to the molecular stacking axis (black arrows). Purple and light blue molecules correspond to perylene and TCNQ molecules of the stack. Grey molecules are the perylene molecules separating molecular stacks.

Incident light was polarized parallel and perpendicular to the molecular stacking axis; this axis is $\hat{a}$ for P1T1, $\hat{a}$ for P2T1, and $\hat{c}$ for P3T1. XRD was utilized to determine the crystal face and also the direction of the molecular stacking axis for the individual samples in all compounds except for P1T1. In P1T1 the long axis of the needle-shaped sample was used as the molecular axis, as these two are known to be coincident from XRD[63]. Results from the resonance experiment are

compiled for representative phonons of TCNQ and perylene in Figure 4.11 for the excitation wavelengths of 457, 514, 633, and 785 nm.

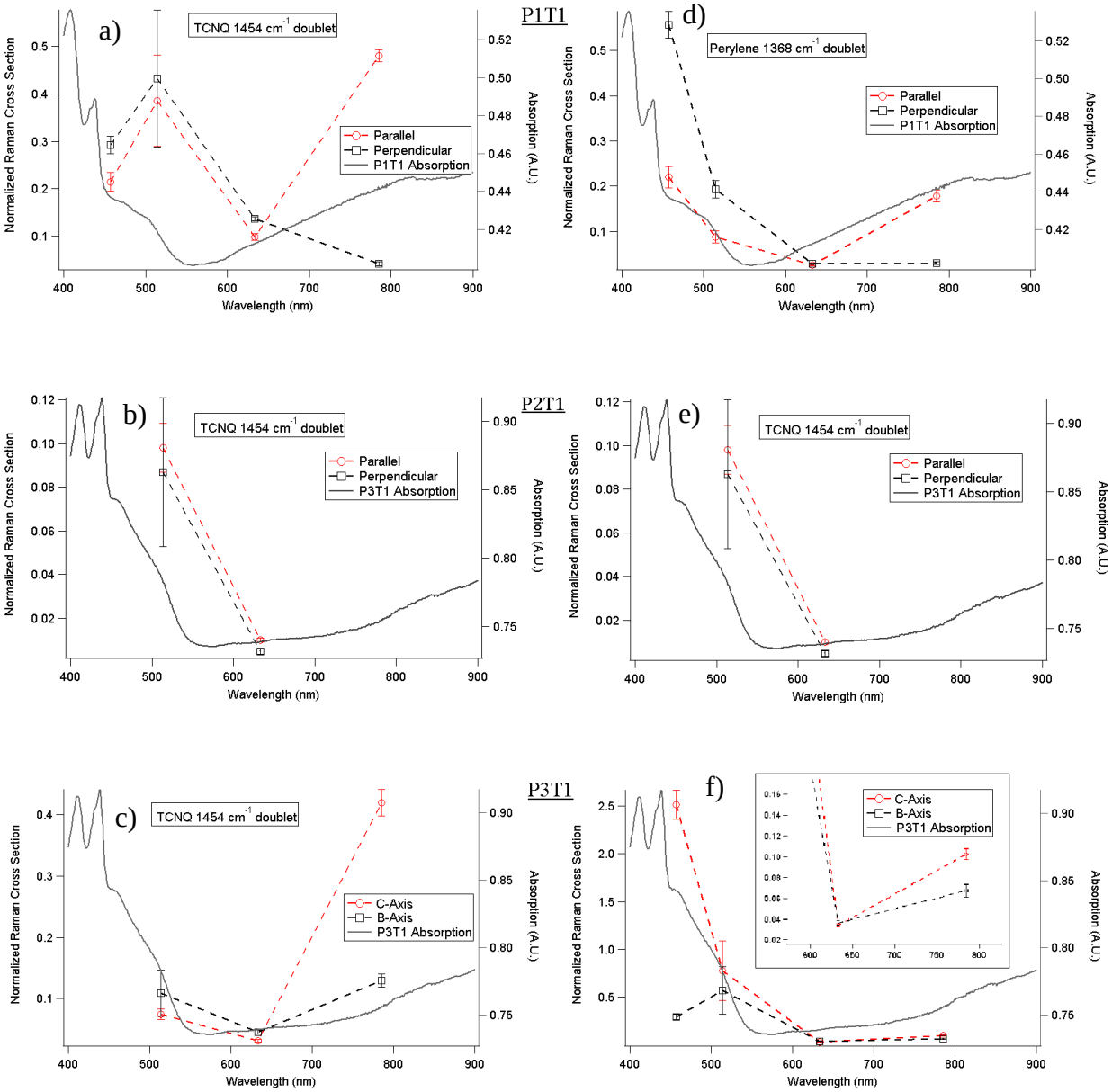

Figure 4.11: Resonance Raman profiles of PnT1 of the intramolecular phonons of TCNQ (1454cm^{-1}) (a-c) and perylene (1368cm^{-1}) (d-f) normalized to the scattering cross section of diamond. P3T1 absorption included for P2T1, since I was not able to obtain a spectrum.

The unpolarized powder absorption spectra of P1T1 and P3T1 have been included for those compounds in order to aid the eye and help in interpretation of the data. Unfortunately, there was

heavy fluorescence in P2T1 at an excitation wavelength of 785 nm that masked the ability to extract the scattering cross section for that wavelength. P1T1 and P3T1 also exhibited fluorescence, but it was either weaker or shifted slightly to higher wavelengths. In Figure 4.11 TCNQ intramolecular phonons exhibit similar behavior in all of the PnT1 compounds and appear to mirror the absorption spectra. When the exciting polarization is coincident with molecular stacking axis, as the exciting light wavelength is increased toward the NIR there is an increase in the Raman scattering cross section that coincides with the onset of absorption due to the CT exciton. When the polarization of the light is oriented perpendicular to the stacking axis, the scattering cross section decreases compared to the parallel case; this is true in P3T1 as well. The anisotropy of the scattering cross sections is due to the anisotropy of the transition moment of the CT exciton. These results imply that the CT exciton transition moment is polarized along the molecular stacking axis. This effect is also clearly seen in the resonance profile of perylene intramolecular phonons in P1T1. Perylene intramolecular phonons in P3T1 appear to not be resonant with the CT exciton, but that is an artifact of the scale of the graph; both perylene and TCNQ phonons are resonant with the CT exciton (see Figure 4.11f inset). The very strong resonance of the perylene phonons in the blue wavelength region masks the resonance in the NIR; the Raman scattering cross section is actually three fold larger at 785nm as it is at 633nm. The reason that the change in Raman intensity is not as drastic in P3T1 as in P1T1 between the two polarizations is that in P3T1 the incident polarization is aligned with the crystal b-axis, which is not quite perpendicular to the molecular stacking axis as was measured in the case of P1T1. By definition, this means that there is a projection of the transition moment along the b-axis (see Figure 4.10). Only fully-symmetric (A_g) phonons were observed to be resonant with the CT exciton in each compound. Symmetry arguments based on a few simple assumptions can be

made to aid in interpreting this observation. Assuming that the electronic state of interest is non-degenerate and that the symmetries of the molecules do not change between the ground state and excited electronic state, only totally fully symmetric (A_g) phonons will have non-zero linear electron-phonon coupling constants[25,98]. Therefore, the observed resonant phonons in PnT1 will have non-zero electron-phonon coupling constants. In P3T1, the crystal symmetry is triclinic, meaning that all Raman modes are of crystal symmetry A_g and potentially have non-zero eph coupling constants. P1T1 is monoclinic with two pairs of symmetry-inequivalent perylene-TCNQ units per unit cell. Under these circumstances there are two Raman active symmetries, A_g and B_g. Every molecular phonon will have an A_g and a B_g counterpart (Davydov splitting) in the crystal phase with only the A_g type having non-zero eph coupling constants. In PnT1 and many CT compounds Davydov splitting is too small to be observed experimentally. The anisotropy observed in the Raman scattering cross sections of the CT exciton resonant TCNQ and perylene phonons most probably means that the charge transport in these materials is anisotropic as well. This is so because the CT exciton, which is polarized along the stacking axis, is the lowest excited state of the PnT1 material; therefore the energy barrier for charge transfer will be lower along the stacking axis than any other direction in the crystal. DFT calculations on the directional dependence of the electron and hole effective masses in the unit cells of PnT1 do indeed display an anisotropic character to the electronic coupling[63]. For each compound the lowest charge carrier effective masses occur along the molecular stacking axis.

The interpretation of the resonance Raman spectra becomes less clear at shorter excitation wavelengths (<550nm), due to spectral congestion in the absorption data. Illumination with either blue or green light induces absorption by local perylene and TCNQ molecular excitons and most likely also higher-order CT excitons. There is most likely also mixing of some

or all of these excitons. Analysis of the resonance Raman profiles give some deeper insight into these transitions that it is more difficult to obtain solely from the absorption spectra. There appears to be a maximum in the Raman intensity of the TCNQ phonons in P1T1 at an excitation wavelength of 514 nm corresponding to the shoulder in the absorption spectra. The decrease in Raman intensity at 457 nm coincides with the observation of Bandrauk[147] that as the exciting light wavelength goes toward the blue, the perylene phonons increase drastically in intensity and the TCNQ phonons become comparatively far less intense. Going back to the resonance of the TCNQ phonon in PnT1at 514 nm, it appears there is no polarization dependence of the Raman scattering cross section of the resonant phonons with this transition. Therefore it is most likely not a CT exciton, whose transition moment has been consistently observed in similar materials to be parallel to the molecular stacking axis[81,210]. It is also hard to tell from the data if this electronic transition is coming solely from a TCNQ exciton, due to the presence of overlapping perylene excitons. In both P1T1 and P3T1 there is a large polarization dependence of the cross sections at an excitation wavelength of 457 nm. The Raman cross sections are large when the incident polarization vector is perpendicular to the stacking axis for P1T1 and when the incident polarization vector is parallel to it for P3T1. Various polarized absorption and reflection studies[200,211,212] on crystalline perylene have identified the lowest electronic transition to be a molecular transition of symmetry B_{2u} polarized along the long axis of the perylene. According to those studies the Raman scattering cross sections are maximized for incident light polarized parallel to the long axis of perylene. In P1T1 the resonance data are consistent with this interpretation since when the incident electric field vector is perpendicular to the stacking axis the projection of the electric field vector on the long-axis of perylene is greater than when the incident polarization is parallel to the stacking axis (see Figure 4.10). When the incident electric

field is polarized parallel to the stacking axis it is nearly coincident with the long axis of the perylene molecules that separate the DAD stacks. However, when the incident electric field is polarized along the b-axis, neither the separator perylenes nor the perylenes in the stacks are effectively excited (see Figure 4.10).

4.4.2 Quantitative determination of local eph coupling

Quantitative estimates of linear eph coupling constants for specific phonons and the overall polaron binding energy (E_{pol}) for both perylene and TCNQ in PnT1 can be made using resonance Raman spectroscopy. As mentioned in the introduction, E_{pol} is half the value of the reorganization energy, λ. The reorganization energy is made in reference to the anion of the acceptor molecule and the cation of the donor molecule. This is so because in a hopping-like charge transfer process a charge carrier will be localized and relaxed on a particular molecule before transferring to a neighboring molecule. Therefore, knowledge of the reorganization energy of the ionic molecular states is important in describing charge transport. In a CT compound these molecular ionic states can be probed simultaneously by studying the charge transfer exciton, where the donor is ionized and the acceptor is reduced. Figure 4.12 represents a symbolic view of the relation between the ground state and the CT state along a phonon coordinate Q.

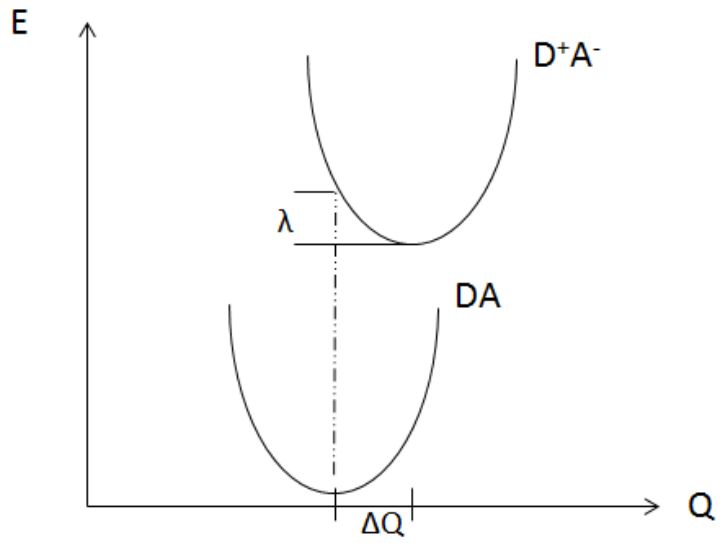

Figure 4.12: Potential energy diagram of the ground state and CT state projected along a phonon coordinate. λ is the reorganization energy, Q is the phonon coordinate, and ΔQ is the displacement between the two potential energy curves.

In this picture, when PnT1 is optically excited in to the CT state the perylene and TCNQ molecules will then relax into their new molecular and intermolecular geometries. The change in energy between the relaxed and unrelaxed configurations of the molecule is called the reorganization energy. Each phonon will have its own specific contribution to the reorganization energy, since the geometry of the excited state is not displaced relative to the ground state in all phonon coordinates by the same amount. The relationship between the reorganization energy and the displacement between the two electronic states (ground and CT) is shown in equation 4.2.[213]

$$\lambda_k = \frac{\hbar\omega_k\Delta_k^2}{2} \tag{4.2}$$

λ_k is the phonon specific reorganization energy, ω_k is the phonon frequency, and Δ_k is the phonon specific dimensionless displacement between the potential energy surfaces (PES) of the two electronic states. Δ is related to ΔQ by a factor of $(\omega/\hbar)^{1/2}$. Heller and co-workers[171,172,175,179] developed a time dependent formulation of resonance Raman scattering that can relate measured

resonant Raman cross sections to phonon dimensionless displacements under certain assumptions, namely short-time dynamics. In short-time dynamics the optically-excited wave-packet spends a very short time (10^{-15} s) traveling on the excited state PES before transitioning down to the ground state. Heller and co-workers were able to show that most of the contribution to the scattering cross section was attained near the Franck-Condon region of the excited state PES, i.e. the region of the excited state the wave-packet initially travels upon (see chapter 3 for more information). They were able to show that when the frequency of the incident optical radiation was tuned away from the excited state absorption maximum the lifetime of the wave-packet in the excited state was very short. This occurs in the pre-resonance region of the absorption spectrum near the onset of the electronic transition. In this region of short-time dynamics the relative resonant Raman cross section of a phonon is related to the slope of the excited state PES projected along that phonon coordinate. This relation can be expressed in terms of dimensionless displacements as shown in equation 4.3[171,172].

$$\frac{I_1}{I_2} = \frac{\Delta_1^2 \omega_1^2}{\Delta_2^2 \omega_2^2} \tag{4.3}$$

I_k is the intensity of a resonant Raman transition. In addition, equation 4.3 assumes that the ground state and CT state phonons have nearly the same frequency, that there is no change in the description of the phonons between the two electronic states (Duschinsky rotation), and finally that the transitions are Franck-Condon in nature, i.e. the transition dipole moment between the two states is not modulated by phonons. Since equation 4.3 is a ratio, the dimensionless displacements can be scaled to obtain absolute displacements using the experimental CT absorption spectrum.[172]

$$2\sigma^2 = \sum_k \Delta_k^2 \omega_k^2 \tag{4.4}$$

In equation 4.4 σ is the standard deviation (assuming a Gaussian distribution) of the CT absorption spectrum. This formula was also derived using short-time dynamics and assumes that the entire width of the absorption spectrum is due to high-frequency intramolecular phonons.[181] The short-time dynamics/pre-resonance condition is met by the excitation at 785 nm (see Figure 4.2). Under these assumptions, the more intense the resonant Raman transition is, the higher will be its contribution to the total reorganization energy. The reorganization energies and E_{pol} from using equations 4.2, 3, and 4 on the resonant Raman transitions observed in P1T1 and P3T1 at 785 nm are displayed in Table 4.2. Due to the heavy fluorescence at room temperature P2T1 data were not available.

Table 4.2: Reorganization and E_{pol} for P1T1 and P3T1

Freq. (cm^{-1})	P1T1: Reorganization Energy (meV)	P3T1: Reorganization Energy (meV)	Type
Resonant TCNQ Phonons			
143	16	0	CN group bending
332	85	80	CN group and C-C bend
597	6	6	C-C stretch and CN bend
708	24	31	C-C ring and C-C wing stretch
950	2	4	C-C ring and C-C wing stretch
1198	20	32	C-H bend
1447	21	32	Ring and external C=C stretch
1452	24	23	Ring and external C=C stretch
1604	19	20	C=C stretch, C-H bend
2220	28	29	CN group stretch
Resonant Perylene Phonons			
352	17	6	C-C-C bend
417	7	5	C-C-C bend

Table 4.2 (cont.)

428	5	<1	?
744	2	~0	?
753	0	4	C-C-H bend
773	3	10	C-C-H bend
780	6	<1	?
816	0	2	C-C-H bend
977	0	2	C-C stretch
1292	5	12	C=C stretch
1299	21	7	C=C stretch
1367	18	16	C=C stretch
1570	28	14	C=C stretch
	E_{pol} (meV)	E_{pol} (meV)	
TCNQ	123	129	
Perylene	56	39	
Parameters:	FWHM: 4000 cm^{-1} ± 200	FWHM: 4000 cm^{-1} ± 200	

In the calculation of Table 4.2, the value of σ was assumed to be the same in P1T1 and P3T1. Both our own measurements and those of others[149] seem to confirm this assumption. The determination of σ was made difficult by the vibronic structure seen in the CT exciton absorption spectrum, because the CT exciton appears to be the superposition of two displaced distributions. Because of this, the value of σ used here is an approximate value, hence the large uncertainties. Such an uncertainty in σ results in uncertainties of a few meV for each phonon reorganization energy and ±10 meV for E_{pol}. In spite of the inherent uncertainties, the agreement of E_{pol} with values derived from both of the other experimental methods and from theoretical calculations is quite remarkable. E_{pol} in TCNQ has been calculated [64] to be 128 meV. A comparison with some other values determined by other researchers is tabulated in Table 4.3.

Table 4.3: Comparison of polaron binding energy of TCNQ by different researchers.

E_{pol} (meV)	Material	Method	Author
131	$TEA(TCNQ)_2$	Optical conductivity	Rice et al.[214]
99	K-TCNQ	Optical conductivity	Pecile et al.[215]
128	TCNQ	DFT Calculations	Brédas et al.[64]
128	DBTTF-TCNQ	Vibrational Spectroscopy	Girlando et al.[79]
125	PnT1	Resonance Raman	This work
Avg. = 121			

Overall, many of the phonon-specific reorganization values agree between the compounds, but there are some stark differences too. There appears to be a reorganization energy redistribution in going from P1T1 to P3T1, where much more of the reorganization energy is distributed over the C=C in-plane stretches of the TCNQ molecule in P3T1, namely the 1197 and 1447 cm^{-1} phonons. One contributing reason for this redistribution is in part because there was no 143 cm^{-1} phonon observed in P3T1. The lack of a 143 cm^{-1} phonon will cause the energy of the absorption bandwidth (see equation 4.4) to be distributed over a smaller number of phonons than in P1T1. In molecular TCNQ the 144 cm^{-1} mode is an A_g in-plane bending of the cyano group tails as pictured in Figure 4.13.

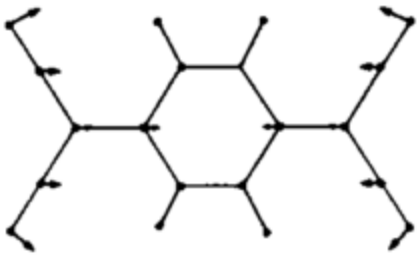

Figure 4.13: A_g 144 cm^{-1} phonon, adapted from ref.[82]

One hypothesis for the reason this phonon is missing from the P3T1 spectrum is that the resonance has been quenched due to interaction with the free perylene spacer molecules. The cyano groups interact with the surrounding crystalline environment and surrounding molecules much more easily than do the phonons that stretch the inner quinoid ring. However, the 2220 cm^{-1} in-plane cyano-group stretching mode has the same reorganization energy in both P1T1 and P3T1. The reason that there is no change in eph coupling between the two compounds for this phonon is likely a function of the much higher energy of this phonon, where the energy of the 144 cm^{-1} phonon is less than kT (~200 cm^{-1}) and is more prone to changes in lattice dynamics whose energies are around or less than kT. E_{pol} for perylene in P3T1 is smaller by 17 meV than in P1T1. I was not able to find any values for E_{pol} of perylene in the literature, so this may be the first time this has been determined. A similar effect happens for the perylene phonons in going from P1T1 and P3T1 in that the lower frequency mode at 352 cm^{-1} (Figure 4.14) has its resonance reduced by 11 meV. This mode is an in-plane C-C bend on the exterior of the perylene molecule. The lower frequency and the overall motion caused by the phonon indicate that this mode will also be affected by the addition of spacer perylenes in going from P1T1 to P3T1. Having the mode-specific eph coupling constants for P2T1 would further bolster this hypothesis. The overall distribution of the perylene reorganization energy is bimodal in P1T1, where most of the reorganization energy resides on the extremes of phonon frequency. In P3T1 the reorganization energy is more evenly distributed. The even distribution of the reorganization energy and smaller E_{pol} in P3T1 points to a more delocalized charge distribution over the perylene molecules in the charge transfer state. Since there are two perylene molecules per stack in P3T1, in the charge transfer state the positive charge (hole) will be delocalized over both perylene molecules, rather than just the one in P1T1. By default, the mean charge per molecule is

less in P3T1 than in P1T1 resulting in a smaller E_{pol}, because the perylene molecules do not relax to their fully ionic state.

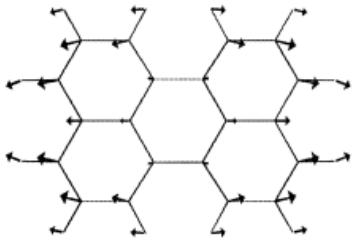

Figure 4.14: A_g 352 cm^{-1} perylene phonon, adapted from ref.[208]

4.4.3 Connection to transport

The simplest incorporation of local electron-phonon coupling into a charge transport model is through the hopping model. In the hopping model, the greater that the E_{pol} is, the lower the mobility will be. E_{pol} is roughly twice as large for perylene than for TCNQ in both P1T1 and P3T1. Furthermore, because E_{pol} for perylene in P3T1 is smaller than in P1T1, P3T1 will be more favorable for hole transport. Therefore, under the assumptions of this model, both compounds will exhibit hole transport and P3T1 will have a higher hole mobility. P3T1 does in fact show hole transport, but in P1T1 the transport is by electrons. The hopping model fails to explain the observed charge transport characteristics of PnT1. Thus, neither the band-like or hopping models are sufficient descriptions for charge transport in PnT1. These models assume either a fully delocalized charge carrier wavefunction over the expanse of the material (band-like) or a highly localized charge carrier on a molecular site (hopping). In actuality, the situation is more likely somewhere in between. In this case the concepts of local electron-phonon coupling take on new meaning when the charge carrier is not highly localized on the molecular site. Furthermore, incorporating non-local electron-phonon coupling into these models is important as

it can either localize charge carrier wavefunctions similar to E_{pol}, or it can also delocalize charge carriers through thermal fluctuations of the transfer integral.

4.5 Conclusions

This chapter focused on the effect of structure on the degree of charge transfer and local electron-phonon coupling. In the first part of this chapter it was shown that the degree of charge transfer increases as the number of donors increases due to a decrease in the donor-acceptor distance. Evidence for this came from temperature-dependent measurements of the degree of charge transfer and XRD measurements of the mean plane distance between adjacent donor and acceptor molecules. DFT calculations of transfer integrals in PnT1 at room temperature and versus temperature agree with our findings. In the second part of this chapter the local electron-phonon coupling constants were determined for intramolecular phonons of both perylene and TCNQ. It was found that the polaron binding energy in perylene was roughly half that of the binding energy of TCNQ. Also, the polaron binding energy in P3T1 was less than that in P1T1 by 30%. This was attributed to delocalization of charge in the CT state over the two stacking perylenes in P3T1. The polaron binding energies for TCNQ in P1T1 and P3T1 were similar and agreed with determinations from other studies and calculations. Overall, there was good agreement between experimental and theoretically-determined values for local electron-phonon coupling and electronic coupling. The attempt to connect these values to observed charge transport characteristics using purely band-like and hopping charge transport models was unsuccessful. This result points to the need for new charge transport models, including non-local electron phonon coupling and partially delocalized charge carrier wavefunctions.

CHAPTER 5: ANTHRACENE-PYROMELLITIC DIANHYDRIDE

5.1 Introduction

Non-local electron-phonon (eph) coupling in organic charge transfer compounds is an ongoing research area. This type of coupling represents modulations of the transfer integral due to phonons. The phonons most capable of having large non-local coupling constants are low-frequency lattice phonons. DFT calculations of the coupling constants are highly dependent on the type of functional used, and experimental studies on CT compounds are minimal. The goal of the work summarized in this chapter is to determine the non-local eph coupling in a CT compound and compare it with theoretical predictions. This is a major step in pushing our understanding of this type of coupling. Experimental results of this kind which are presently lacking in this research area will help to constrain and inform theoretical results. APMDA was chosen because it has a charge transfer transition in the visible. This is important primarily for practical reasons, namely that available experimental apparatus (including laser excitation wavelength tuning capabilities and triple grating spectrometer) is well suited for measuring low frequency phonons of this molecular crystal system. In PnT1 the charge transfer transition was in the NIR, outside of the range of the capabilities of our system. This chapter will begin with a discussion on the basic measured optical and vibrational properties of APMDA, then move into using a time dependent formulation of resonance Raman scattering presented in chapter 3 to extract both local and non-local electron-phonon coupling constants. Following this there will be a discussion on the extracted parameters and their comparison with theoretical predictions.

5.2 Optical spectra

The unpolarized UV-vis absorption spectrum of APMDA powder compared with those of anthracene powder and PMDA powder is displayed in Figure 5.1.

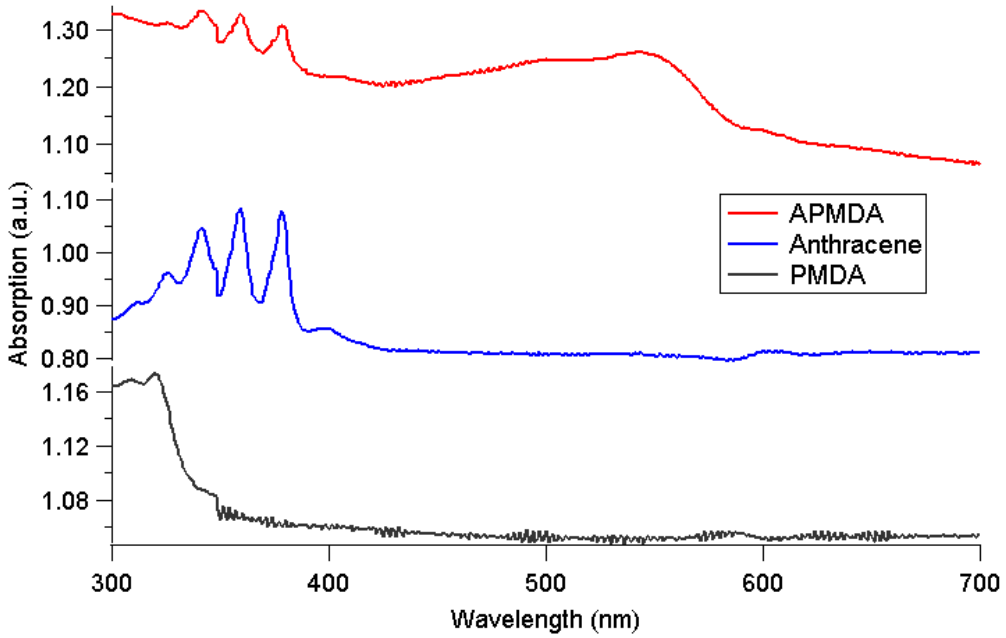

Figure 5.1: Unpolarized powder absorption of anthracene-PMDA (red), anthracene (blue), and PMDA (blk)

The wavelength of the charge transfer exciton is roughly between 415-600 nm and it is polarized along the molecular stacking axis of APMDA (c-axis).[154–156,158,216] In anthracene the absorption region between 300-400 nm corresponds to vibronic transitions between the ground state and the lowest excited electronic state of anthracene, namely the singlet B_{2u} state polarized along the short axis of anthracene[154,217]. In PMDA the lowest electronic absorption transition occurs above 335 nm; this has been observed also in solution spectra with an absorption maximum at 315 nm[154].

Obtaining a polarized single-crystal absorption spectrum of APMDA is difficult, because the samples are optically thick and have needle-like morphology. One way to get around this

experimental difficulty is to use reflection data and then use a Kramers-Kronig transformation[218] in order to obtain an absorption spectrum. Our lab was not equipped with the appropriate equipment, such as a micro-spectroreflectometer, to probe the small faces of the APMDA single crystal. Because of this, we relied on the absolute polarized absorption spectrum published by Eckhardt and coworkers[154]. The graph is reprinted here in Figure 5.2.

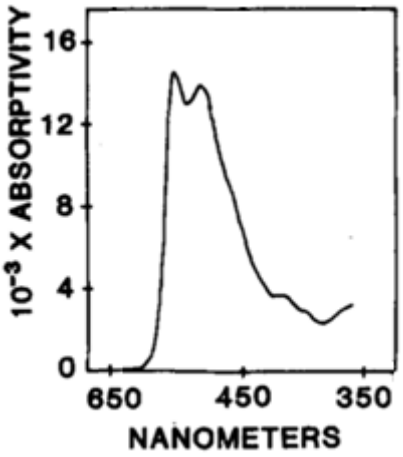

Figure 5.2: Kramers-Kronig transformed absorption spectrum of APMDA from the (010) face. Incident light is polarized along the (001) axis. Reprinted from ref.[154]

This measurement is for absorption on the (010) face of APMDA with incident light polarized along the c-axis, the molecular stacking axis of this material. In addition, they calculated the dipole strength for this charge transfer excitation to be 0.198 $Å^2$. They further verified that the CT exciton was completely polarized along the c-axis and using piezomodulation spectroscopy[219] they discovered two charge transfer excitons at wavelengths of 413 nm, and 348 nm in addition to the first CT exciton at 538nm. A schematic of the scattering configuration used by Eckhardt on the molecular level is displayed in Figure 5.3. This was the scattering configuration used in our experiments for all Raman measurements on APMDA.

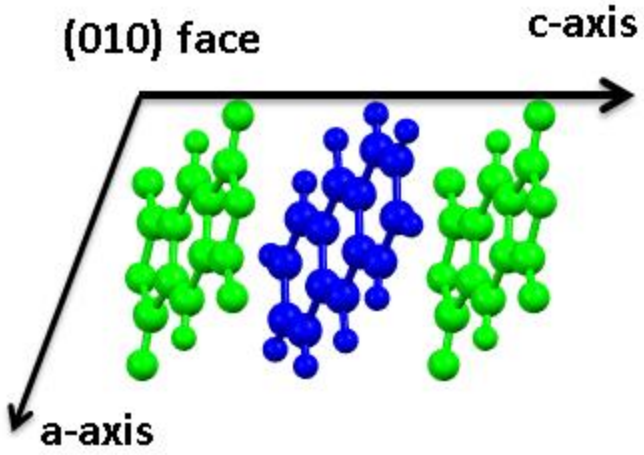

Figure 5.3: Molecular level scattering configuration of APMDA projected on to the (010) face. PMDA (green), anthracene (blue)

5.3 Raman spectra

Significant photo-luminescence from the recombination of the CT exciton at room temperature prevented any attempt at spontaneous Raman measurements at excitation wavelengths higher than 650 nm. To probe the CT exciton without saturation of the detection system, Raman spectra following 620 nm excitation were recorded for APMDA cooled to 80 K, Figure 5.4. These data have been corrected for the frequency response of the grating/detection system using the calibrated emission from Kiton red dye excited at 532 nm.

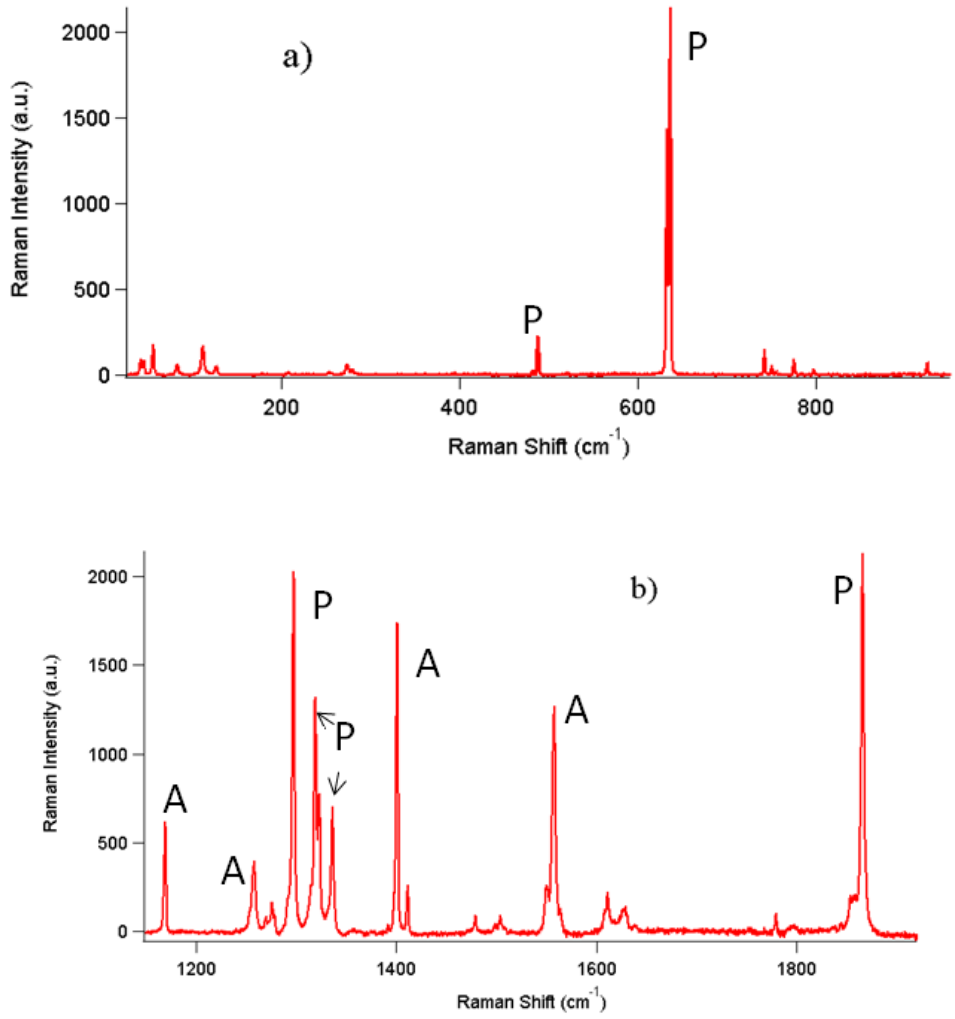

Figure 5.4: Raman spectra at 80K of the (010) face of APMDA with incident light polarized parallel to the (001) axis a) Frequency range 30-950 cm^{-1} b) 1150-1920 cm^{-1} (No significant peaks in regions not presented) Prominent intramolecular peaks are labelled as belonging to the P (PMDA) or A (anthracene) molecule.

According to the absorption spectrum of APMDA, Figure 5.2, Raman spectra collected by using an excitation of 620 nm, Figure 5.4, should include only minimal pre-resonance effects due to resonance with the CT exciton. Overall, the most dominant Raman intensity stems from intramolecular phonons of either the PMDA or anthracene molecule (>600 cm^{-1}). The intermolecular region below 200 cm^{-1} is weaker in intensity and has six clear peaks. By symmetry, six fully-symmetric librational phonons of anthracene and PMDA are expected. Identification of these intermolecular phonons was done by Macfarlane and coworkers[159] and

they showed that the phonons located at 43, 57, and 84 cm^{-1} are librations of PMDA and the phonons located at 47, 113, and 127 cm^{-1} belong to anthracene with each libration occurring about the Z, Y, and X principal axes respectively, as defined in Figure 5.5.

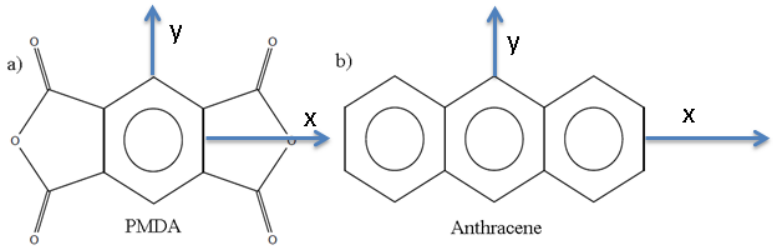

Figure 5.5: Molecular principal axes for a) PMDA b) Anthracene , the z-axis is out of plane.

However, Macfarlane's calculations did not consider coupling between anthracene and PMDA. Calculations completed by our collaborators, Dr. Coropceanu and coworkers, using DFT, showed that the motions of the two lowest phonons of PMDA (43 cm^{-1}) and anthracene (47 cm^{-1}) are coupled motions around the Z molecular principal axis. The 43 cm^{-1} libration is displayed in Figure 5.6 as an example of the coupling.

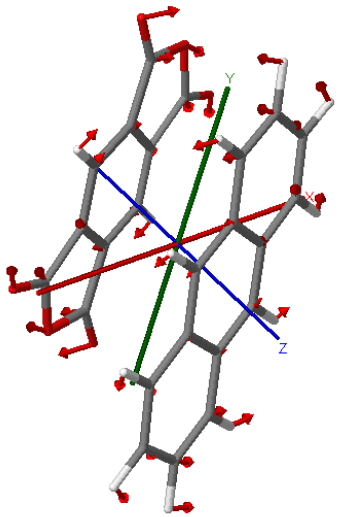

Figure 5.6: 43 cm^{-1} libration of APMDA. The axis system corresponds to the crystal coordinate system, with the z-axis coincident with the c-axis.

The rest of the motions of the librations of APMDA corresponded well with the identifications made by Macfarlane and coworkers. Identification of the intramolecular phonons was completed by comparing the Raman spectra of crystalline PMDA and crystalline anthracene with that of APMDA. Some of the most intense phonons have been labeled in Figure 5.4. A short list of the most intense phonons along with a description of their motion has been included in Table 5.1. Due to the low symmetry of the crystal, all Raman observed fundamentals are fully symmetric (A_g).

Table 5.1: Description and assignment of most intense observed intramolecular phonons at 620 nm excitation

Frequency (cm^{-1})	Species	Description
636	PMDA	In-plane C-O-C bend
1297	PMDA	Skeletal breathing of central benzene ring
1400	Anthracene	In-plane C=C and CC stretching
1556	Anthracene	In-plane C=C and C-C stretching
1865	PMDA	In-plane C=O and C-O-C stretching

5.3.1 Degree of CT

Comparing the APMDA intramolecular phonons with those of anthracene and PMDA revealed no significant shifts in frequencies between the parent and CT compounds. All shifts were less than $<7cm^{-1}$, which is around the tolerance usually given for shifts due to changes in solid state environment in going from a monomolecular to a bi-molecular compound[220]. Using the same method as in TCNQ-based CT compounds, in which a charge-sensitive phonon is chosen to estimate the degree of charge transfer (see chapter 4), I calculated the Raman phonon frequencies of the PMDA anion using $DMol^3$ in Materials Studio[221–223]. In this procedure phonons with large shifts in frequency between the neutral and ionic state are preferred so that

effects of the environment become less important. There is a predicted shift of over 90 cm^{-1} for the PMDA C=O stretching phonon between the neutral and the fully-ionic state, and this phonon is thus a good candidate for this procedure. However, there is essentially no observed shift in that phonon between the parent and the CT compound. There is a shift of ~7 cm^{-1} of the 636cm^{-1} PMDA phonon between the parent and CT compound. The calculation of the vibrational frequencies of the anion predicts only a shift of 2 cm^{-1} between the frequencies of the neutral PMDA molecule and its anion. From these observations, APMDA has minimal charge transfer in the ground state. However, I have not looked in depth at the effect of ionization on the anthracene molecule. Future investigations should include an analysis of the change in bond lengths among the neutral, ionic, and CT compound donor and acceptor molecules to confirm that indeed there is minimal charge transfer. An energy argument in favor of the conclusion drawn from the Raman measurements is based on the energy cost of ionizing the donor-acceptor pair compared with the electrostatic energy gain from ionization. The cost of ionization is usually expressed as the difference in energy between the ionization potential (IP) of the donor molecule and the electron affinity (EA) of the acceptor molecule. The gain in energy is quantified by Madelung energy, E_m. As described in the introduction, if IP-EA is much less than E_m the CT compound tends to be neutral, if IP-E_a is near E_m then it has intermediate ionicity (ρ~0.5-0.7), and if IP-EA is much greater than E_m the CT compound is ionic. E_m has not been calculated for APMDA, but it has been calculated for a number of CT compounds where typical numbers range from 2-4.5 eV[59,80,224]. The IP-EA difference in APMDA is 5.42 eV. This means that APMDA is most likely neutral to possibly quasi-neutral. As a comparison, P1T1 has an IP-EA difference of 4.16 eV and a calculated E_m of 3 eV[150] and has a measured ρ of 0.04 (see

section 4.3.1 above). If E_m in APMDA is close to that of E_m in P1T1, then APMDA is certainly near neutral.

5.4 Resonance Raman spectra

Now that the basic optical and vibrational properties have been discussed, a proper analysis of the resonance Raman spectra can ensue with the goal of extracting electron-phonon coupling constants. Resonance Raman spectra of APMDA with an excitation wavelength coincident with that of the charge transfer exciton located at 546 nm are required to extract the electron-phonon coupling constants. In this experiment, seven different excitation wavelengths were chosen ranging from 620 nm to 576 nm. The limiting factor in using even lower excitation wavelengths was fluorescence due to the CT exciton. At each excitation wavelength the Raman spectrum from 30-2000 cm^{-1} was taken and the integrated area of each peak was recorded and converted to a scattering cross section; these are known as resonance Raman profiles. The Raman scattering configuration was that of Figure 5.3. Each spectrum was corrected for any wavelength response due to the spectrometer detection system using the calibrated emission of Kiton red dye and then normalized using the measured and known scattering cross section of diamond under the same collection conditions. These numbers were converted into an absolute Raman scattering cross section using the procedure described in chapter 3 and accounting for the reflection and absorption constants of the materials, where the APMDA constants were derived from Eckhardt's reflection data at normal incidence[154].

All of the phonons in APMDA are of A_g symmetry, therefore it is expected that each phonon is allowed by symmetry to be resonant with the CT exciton. A comparison between the Raman spectra at excitation wavelengths of 620 nm and 576 nm is shown in a couple of selected spectral ranges, as seen in Figure 5.7.

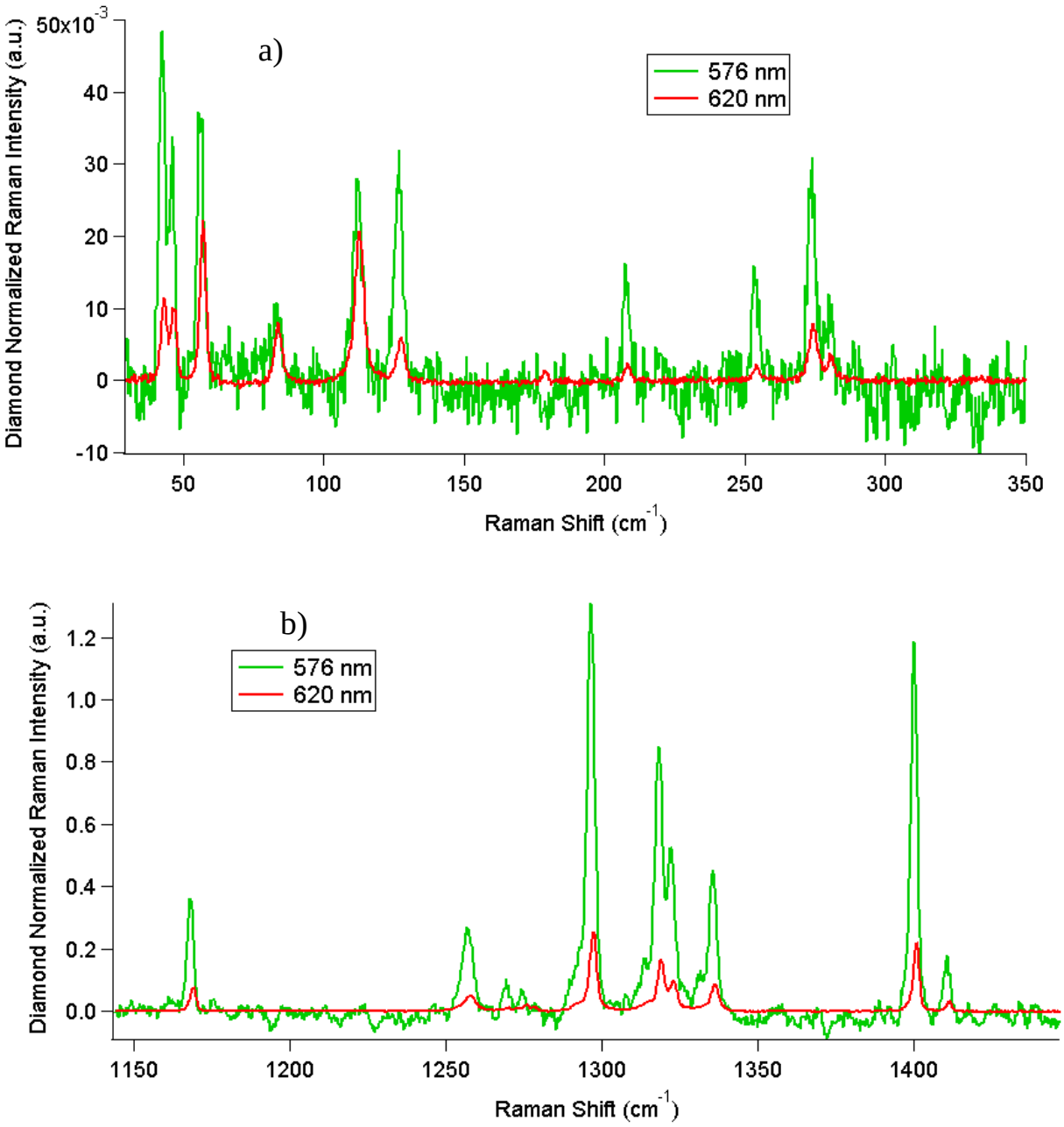

Figure 5.7: Resonance comparison spectra of APMDA at two different spectral windows a) 30-350 cm^{-1} and b) 1145-1450 cm^{-1} and at two excitation wavelengths 576 nm (grn) and 620 nm (red)

Looking at the low frequency region in Figure 5.7a there appear to be some phonons that are more strongly resonant than others when compared to the near-non-resonant spectrum at 620 nm. In particular, it appears that the librations at 43 (Anth-PMDA coupled), 47 (Anth-PMDA coupled), and 127 (Anth.) cm^{-1} are the most strongly resonant of the intermolecular phonons,

whereas the librations at 84 (PMDA) and 113 (Anth.) appear to increase very little in intensity. At higher Raman shift the increase in intensity upon resonance appears much stronger than in the intermolecular regime. These highly resonant intramolecular phonons are mainly double bond stretching of either carbon or oxygen in anthracene and PMDA.

5.4.1 Fitting resonance Raman and optical spectra

Quantitative determination of the electron-phonon coupling constants can be accomplished using the time-dependent formulation of Raman scattering developed by Heller and coworkers[171,174,175,179]. This method is described in more detail in chapter 3. In this method, absolute Raman and absorption cross sections are simultaneously fit in order to extract phonon-specific dimensionless displacements between the ground and the excited state (which is the CT exciton in this case). The phonon-specific dimensionless displacements can be converted into phonon-specific reorganization energies. Both intermolecular and intramolecular phonons can be fitted so that information on both local and non-local electron-phonon coupling can be extracted, assuming there is a separation between local and non-local coupling based on phonon frequency. Calculations on non-local coupling in APMDA by our collaborators showed that nearly 85 % of the contribution to the magnitude of the non-local coupling was from phonons below 300 cm^{-1}.[139] Therefore, to a first approximation, electron-phonon coupling of phonons of frequencies less than 300 cm^{-1} will be assumed to contribute solely to non-local coupling and phonons greater than 300cm^{-1} to local coupling.

The time dependent formulas for absorption and Raman scattering in the Condon approximation are re-stated (equations 3.27 and 3.40) here in equations 5.1 and 5.2.

$$\left(\sigma_{\rho\sigma_{i,j}}\right)_{Raman} = \frac{\left|(\mu_{(001)})_{CT}^{0}\right|^2 \omega_L \omega_s^3}{4\pi {\epsilon_0}^2 \hbar^2 c^4} \sum_i P_i \int d\delta G(\delta) \times \left| \int_0^\infty dt \, \langle j|i(t)\rangle \exp[i\left(\omega_L + \omega_{gi} - \delta\right)t - g(t)] \right|^2 \tag{5.1}$$

$$(\sigma_{\rho_{g,e}})_{Absorption} = \frac{\pi\omega\left|(\mu_{(001)})_{CT}^{0}\right|^2}{\epsilon_0 \hbar c n} \sum_i P_i \int d\delta G(\delta) \times \int_{-\infty}^{\infty} dt \, \langle i|i(t)\rangle \exp[i\left(\omega + \omega_{gi} - \delta\right)t - g(t)] \tag{5.2}$$

In the preceding equations, $(\mu_{001})^0_{CT}$ is the projection of the transition dipole moment of the CT exciton along the c-axis (001) direction, the index, i, refers to a particular phonon, and j refers to the same phonon in a different vibrational state. ω_L and ω_S are the frequencies of the incident and scattered light, and ω_{gi} is the frequency of the ith phonon in the ground state. P_i is the Boltzmann population of phonons, i, G(δ) is a function describing the static inhomogeneous distribution of shifts, δ, in the purely electronic 0-0 transition, and ε_0 is the permittivity of free space. The overlap functions, <i|i(t)> and <j|i(t)>, depend on the frequencies of the phonons in the ground and CT state, and the dimensionless displacement between the two harmonic potential energy surfaces of the ground and CT state, Δ_i. The function g(t) represents the homogeneous broadening in the system due to unaccounted-for degrees of freedom. In this model, g(t) was partitioned into a contribution from the low-frequency librational phonons measured by experiment and all other degrees of freedom. These unaccounted-for degrees of freedom are represented collectively using a Brownian oscillator model for an overdamped oscillator. Qualitatively, this model describes a system of higher-frequency vibrational degrees of freedom

interacting with a bath of librational and uncounted degrees of freedom. The homogeneous line shape, g(t), is stated in the following equations.[187]

$$g(t) = g_h(t) + g_{vib}(t) \tag{5.3}$$

$$g_h(t) = g'(t) + ig''(t) \tag{5.4}$$

$$g''(t) = -(\lambda/\Lambda)[\exp(-\Lambda t) + \Lambda t - 1] \tag{5.5}$$

$$g'(t) = \left(\frac{\lambda}{\Lambda}\right)\cot\left(\frac{\hbar\Lambda}{2k_bT}\right)[\exp(-\Lambda t) + \Lambda t - 1] + \frac{4\lambda\Lambda k_bT}{\hbar}\sum_{n=1}^{\infty}\frac{\exp(-v_nt) + v_nt - 1}{v_n(v_n^2 - \Lambda^2)} \tag{5.6}$$

$$v_n \equiv \frac{2\pi k_bT}{\hbar}n$$

$$g_{vib}(t) = \sum_j \frac{\Delta_j^2\omega_j^2}{2}[\coth\left(\frac{\hbar\omega_j k_bT}{2}\right)[1 - \cos(\omega_j t)] + i(\sin(\omega_j t) - \omega_j t)] \tag{5.7}$$

Λ^{-1} is the time scale for motion of the Brownian oscillator and λ is its reorganization energy. Δ_j is the dimensionless displacement of the jth librational phonon of frequency ω_j.

Using the above model the Raman and absorption spectra were fit iteratively. Initial guesses for the displacements were made by using the short-time approximation. In this approximation the resonant Raman intensities are proportional to the square of the displacements e.g. $I \alpha \Delta^2\omega^2$. The initial guesses for the displacements of the low frequency librational phonons were chosen similarly. These parameters were adjusted until the overall lineshape of the calculated absorption spectrum was attained. The transition dipole strength and 0-0 electronic transition frequency were set using Eckhardt's absorptivity data. Following this the homogeneous and inhomogeneous linewidth were adjusted until the calculated Raman cross sections were near to the measured values. Minor tweaks to the displacements were then applied

to best match the measured Raman cross sections with calculated ones. The ground state phonon frequencies were determined from the Raman experiment. Unfortunately, the excited state phonon frequencies of CT exciton have not been measured for PMDA or anthracene. To circumvent this, the calculated values for molecular anthracene cation were obtained from prior studies[225–227] and those for the molecular PMDA anion were calculated using DMol^3 in Materials Studio[221,222] using the PWC functional[223] and similarly for neutral PMDA. The shift between the calculated frequency of the neutral PMDA molecule and that of its anion was used to obtain the excited state phonon frequency by adding the calculated shift in frequency to the measured frequency in APMDA. The following fits for both absorption and Raman profiles were obtained using the above procedure and model.

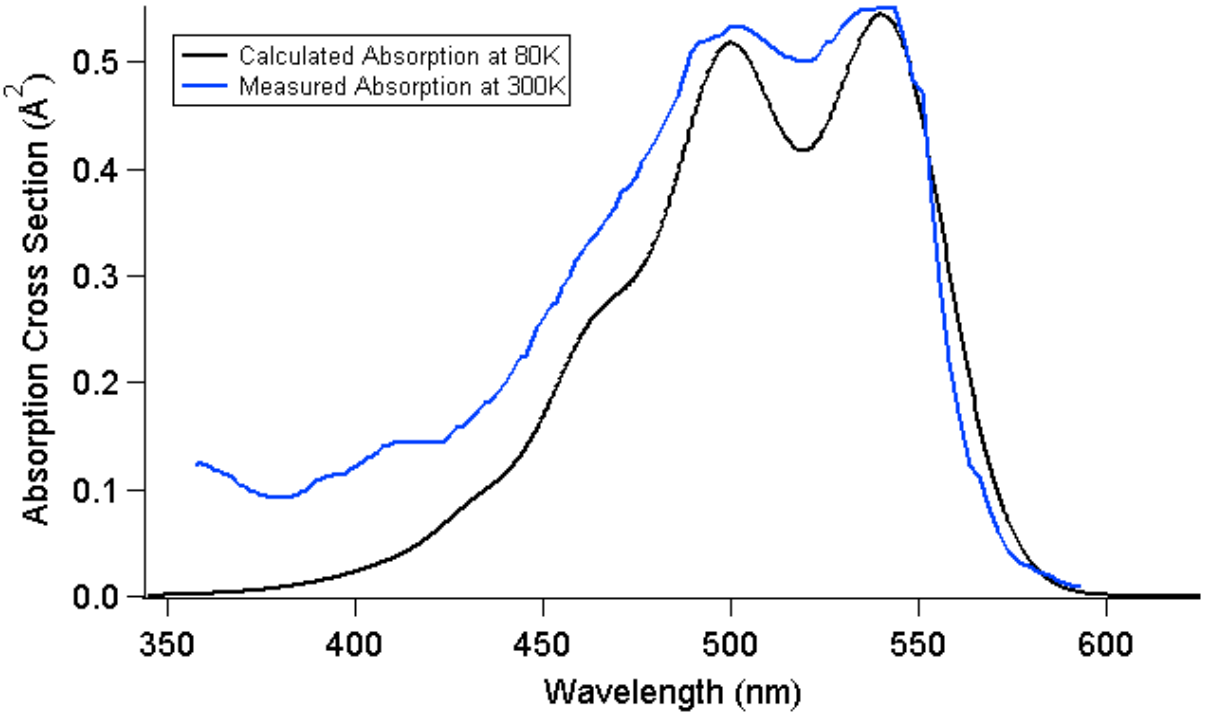

Figure 5.8: Calculated (black) and measured (blue) absorption spectra of the (010) face of APMDA

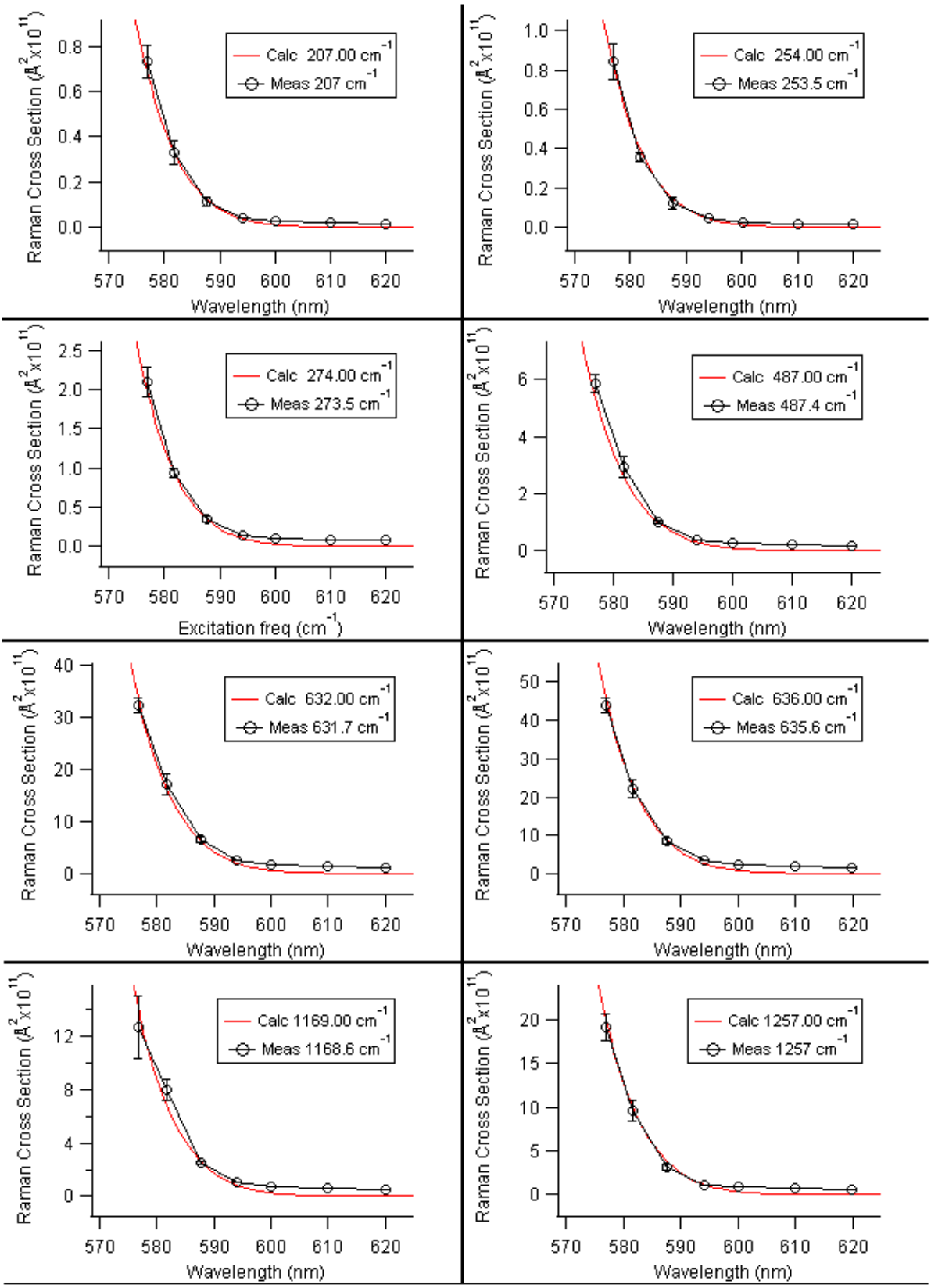

Figure 5.9: Raman fits compared with measured Raman cross sections

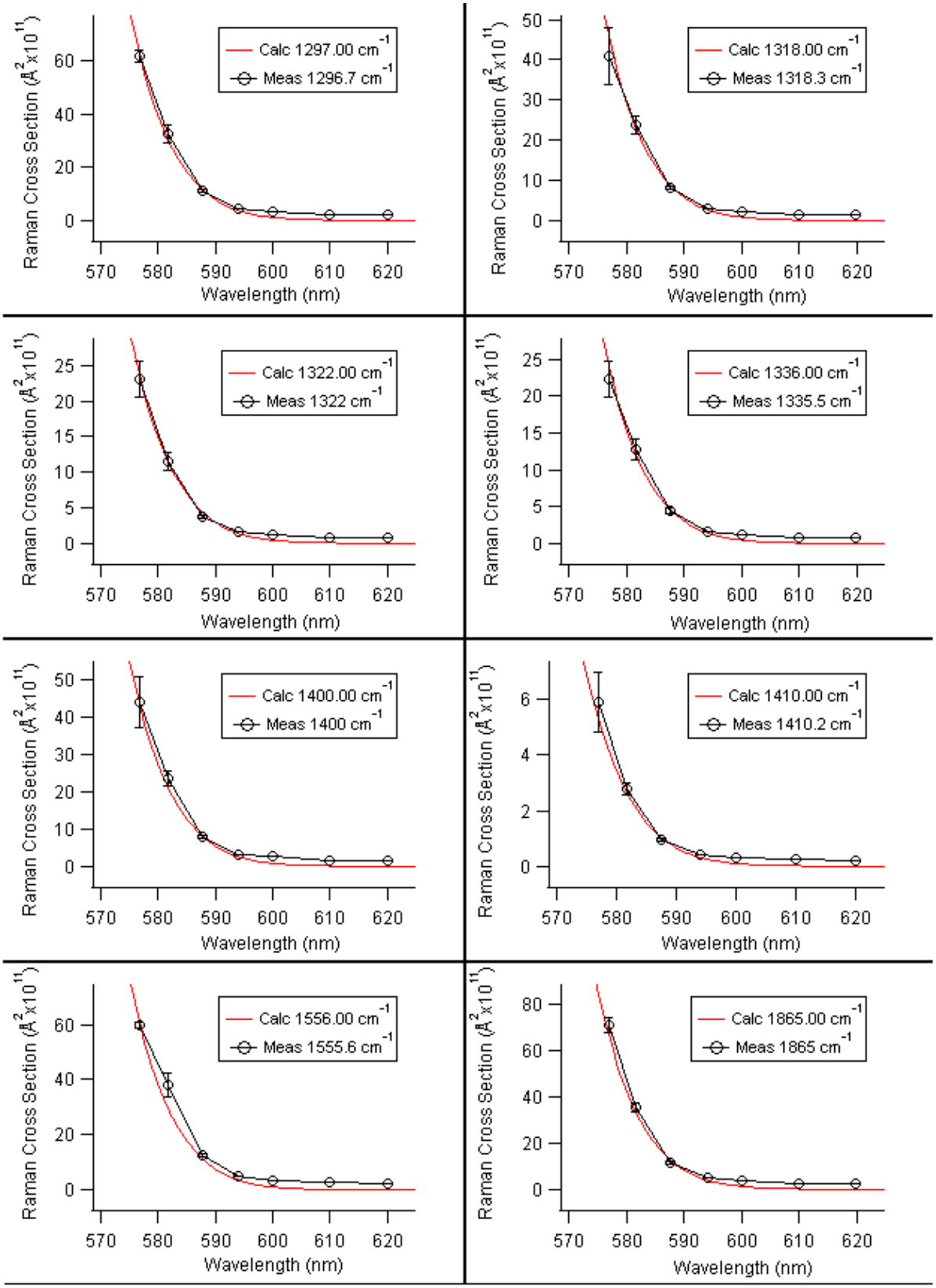

Figure 5.9 (cont.): Raman fits compared with measured Raman cross sections

The best fit parameters are given in Table 5.2.

Table 5.2: Raman model fit parameters of APMDA: Δ_j is the excited state displacement, λ_i the reorganization energy of phonon i. A and P denote anthracene and PMDA respectively.

Ground state frequency (cm^{-1})	Δ_j	λ_i (meV)	Type
43	0.85	1.9	A/P: libration z-axis
47	0.58	1	A/P: libration z-axis
57	0.47	0.8	P: libration short axis
84	0.21	0.2	P: libration long axis
113	0.27	0.5	A: libration long axis
127.5	0.11	0.1	A: libration long axis
207	0.06	0.04	P: out of plane ring bend/C=O
253.5	0.07	0.08	P: out of plane ring bend/C=O
273.5	0.11	0.2	P: out of plane C=O bend
487	0.2	1.2	P: out of plane ring stretch/C=O bend
632	0.52	10.5	P: out of plane skeletal bend
636	0.62	15.1	P: In-plane C-O-C bend
1169	0.35	8.9	A: C-H out of plane bend
1257	0.43	14.4	A: C-H out of plane bend
1297	0.75	45	P: Skeletal breathing of central benzene ring
1318 (doublet)	0.65	34	P: anharmonic?
1322 (doublet)	0.46	17	P:?
1335.5 (doublet)	0.47	18	P:anharmonic?
1400	0.63	34	A: In-plane C=C and CC stretching
1410	0.23	4.6	A: ?
1555.5 (triplet)	0.75	54	A: In-plane C=C and C-C stretching
1865	0.85	83.5	P: In-plane C=O and C-O-C stretching
Other parameters: 0-0 Energy=18300 cm^{-1}; Homogeneous linewidth=61 cm^{-1}; Inhomogeneous linewidth=485 cm^{-1}; transition dipole strength=0.1936 $Å^2$			

5.5 Discussion of fits

5.5.1 Sensitivity of fits to fitting parameters

As discussed at the end of section 3.4, simultaneously fitting both the absolute absorption and resonance Raman spectra constrains many of the parameters used in the model in the Franck-Condon approximation. Furthermore, the fact that the observed absorption spectrum has clear Franck-Condon vibronic progressions helps provide a highly constrained set of parameters to properly fit the measured spectra. To explore the sensitivity of the fits to the fitting

parameters, I multiplied the displacements by constant factors and re-adjusted the broadening parameters slightly to try and attain the best fit possible for both the Raman and the absorption spectra. For example, a 5% increase in the displacements causes the second vibronic transition of the fit located at 500 nm to be more intense than the highest-wavelength one at 546 nm, which is counter to the observed absorption spectrum. Decreasing the displacements by 5% creates the opposite effect in that the intensity of the 546 nm vibronic transition is too large relative to the 500 nm transition. From these observations it becomes clear that the fit is very sensitive to changes in the magnitude of the parameters. Thus, the constraints imposed on the model by the absolute absorption and Raman spectra are sufficient to create a unique set of parameters to describe the observed spectra.

5.5.2 Absorption spectrum

The calculated absorption spectrum mimics the overall shape of the observed spectrum very well. There are some differences however. The calculated line shape is clearly less broad and intense than the observed lineshape in the low wavelength region. On the high-wavelength side the calculated line shape corresponds to the measured one very well, with a small difference in curvature. These observed differences may arise from a few possible sources. One source is that the absorption data for APMDA were measured at 300K and the resonance Raman data were taken at 80K. Thermal broadening will be less at 80K and since the absolute resonance Raman intensities depend on the amount of homogeneous and inhomogeneous broadening it will not be possible to simultaneously fit both the Raman and absorption spectra due to the temperature difference. Therefore, the calculated absorption spectrum could be what would be observed at 80K. Another reason for the discrepancy between the calculated and observed spectra is that this model considers only one resonant electronic state. At lower wavelengths, namely around 417

nm, there appear to be additional excitations that do not fit well with the rest of the vibronic progression of the CT exciton. In fact, Eckhardt and co-workers[154] discovered the next excited charge transfer exciton at 413 nm. Therefore, a portion of the intensity of the high-frequency shoulder is a convolution of the two lowest CT excitons. Finally, the model uses the Condon approximation and so the presence of non-Condon effects would cause problems in simultaneously fitting both the Raman and absorption spectra. Parameters used for the model calculation, such as the 0-0 electronic transition frequency and the transition dipole strength, which are adjustable parameters, agree well with what has been observed. The 0-0 electronic transition used in the calculation was 18300 cm^{-1} and the observed value from prior studies is 18315 ± 5 cm^{-1} [216]. The transition dipole strength of 0.1937 $Å^2$ also corresponds very well with the observed value of 0.198 $Å^2$ determined by Eckhardt and co-workers[154].

5.5.3 Broadening

Both broadening mechanisms represent fluctuations induced in the electronic transition frequency by either phonons or other types of environmental disorder, dynamic or static. The model separates these fluctuations by their time scale into static (inhomogeneous) and dynamic (homogeneous) broadening with respect to the ground state vibrational linewidth. The line shape of the absorption spectrum cannot distinguish between these two types of broadening mechanisms very well and so absolute resonant Raman intensities are needed to distinguish between the two types. The calculated homogeneous linewidth is 61 cm^{-1} and the inhomogeneous linewidth is 485 cm^{-1}. Much of the breadth of the homogeneous linewidth in this model comes from unaccounted Franck-Condon-active vibrational degrees of freedom. The homogeneous linewidth can be converted to a reorganization energy representing the scale in energy fluctuations of the electronic transition energy due to homogeneous broadening[187]. This

scale is 0.03% of the transition energy. Therefore, the small homogeneous linewidth means that many of the degrees of freedom have been accounted for by the inclusion of both intermolecular and intramolecular phonons into the model. Broadening in this system seems to be primarily from inhomogeneous (static) fluctuations of the electronic transition frequency. It is possible that contributions to the inhomogeneous broadening arise from even lower frequency Franck-Condon active phonons, essentially static compared to the inverse vibrational linewidth, such as acoustic phonons not included in the model. On the other hand the presence of any amount of static disorder, such as changes in molecular orientation, will contribute greatly to the amount of inhomogeneous broadening. Disorder in PMDA based CT compounds has been previously reported. For instance, in pyrene-PMDA[228] an order-disorder transition was observed at 160K. Above 160K the crystal is in a disordered phase where a pyrene molecule can be in one of three different orientations. Additionally, in naphthalene-TCNB[186] (tetracyanobenzene) and anthracene-TCNB[229] order-disorder transitions have been observed in which the naphthalene or anthracene molecules randomly occupy two different orientations in the disordered phase. No order-disorder transition has been observed in APMDA to date, however detailed and rigorous X-ray diffraction studies on the compound using have not been completed to rule out the presence of disorder in APMDA. Therefore, orientational disorder in APMDA is one possibility for the dominant inhomogeneous broadening mechanism. Applying this model to the systems with order-disorder transitions would help determine if this model can accurately account for orientational disorder using the inhomogeneous broadening parameter.

5.5.4 Intermolecular regime: Non-local coupling

As seen in Table 5.2, the relaxation energies calculated for the low frequency intermolecular phonons are much lower than those belonging to intramolecular phonons. They

account for only ~1% of the total reorganization energy. This means that eph interactions that localize charge carrier wavefunctions in APMDA are dominated by intramolecular contributions and charge transport models based solely on intramolecular phonons, such as the Holstein 'polaron' model, 'hopping' model, or Marcus' electron transfer theory, will be good approximations in this system. Charge transport measurements using the time-of-flight technique by Karl and co-workers[162] support this conclusion. They found that transport of both holes and electrons along the c-axis was thermally activated and increased as temperature increased, which is true for 'polaronic'/hopping models of charge transport, but also for trap-limited transport. Karl and coworkers attributed these trends to trap-limited transport, because the electron mobility becomes temperature independent above 353K, which was pointed out to be similar to the trend in naphthacene-doped anthracene[230]. Hopping transport was not considered in their study.

From a resonance Raman standpoint, the main reason for the small reorganization energies of the intermolecular phonons is their small relative intensity compared to that of the intramolecular phonons; in addition the reorganization energy is proportional to the phonon frequency, i.e. $\lambda_i=\hbar\omega_i\Delta_i^2/2$. As described earlier, the intermolecular phonons are the main contributors to non-local coupling. The intermolecular phonons with the highest reorganization energy are the coupled out-of-phase and in-phase anthracene and PMDA librations around the axis connecting the two molecules, at frequencies of 43 and 47 cm^{-1}. Also, the libration of PMDA along its short axis has the next-highest reorganization energy at 57 cm^{-1}; phonons with highest reorganization energies are depicted in Figure 5.100 and Figure 5.111.

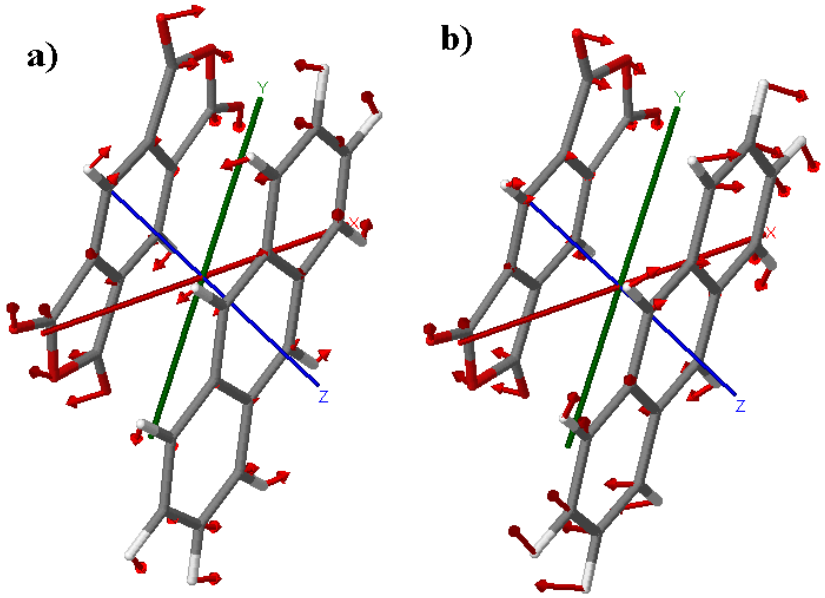

Figure 5.10: Coupled librations of APMDA around axis connecting centers of molecules. A) out-of-phase 43 cm^{-1} and B) in-phase 47 cm^{-1} libration.

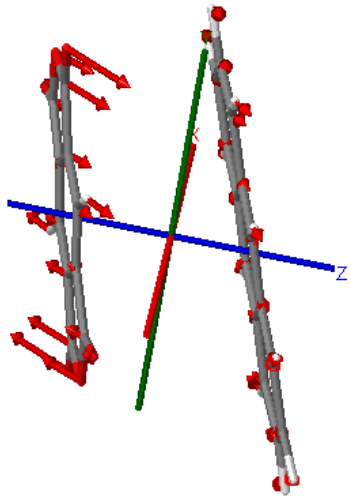

Figure 5.11: PMDA libration at 57 cm^{-1} in APMDA around short axis of PMDA.

In non-local eph coupling, the transfer integral is modulated by intermolecular phonons

$$t_{nm} = t_{nm}{}^{0} + \sum_{i} v_{nmi}\, Q_i \tag{5.8}$$

where the indices 'nm' refer to two adjacent molecular sites and the i^{th} phonon coupling constant v_i is proportional to the derivative of the transfer integral along that phonon i.e. $\partial t/\partial Q_i$. The

transfer integral is defined by the coupling of the HOMO and LUMO of the donor and acceptor molecule respectively. A term used similarly to the reorganization energy[22,23] is

$$L_{DAi} = \frac{v_{DAi}^2}{2\hbar\omega_i} \tag{5.9}$$

where v_{nmi} is the non-local coupling constant between donor and acceptor molecule defined as, $v_{DAi} = \partial t_{DA}/\partial Q_i$. The effect of L (dropping indices) is to lower the energy of a state in which charge has been transferred by an amount L. For instance in a symmetric dimer considering only non-local eph coupling, three electronic eigenstates are formed, a neutral state and a pair of anti-symmetric and symmetric charge transfer states; these are shown in the following energy level diagram.

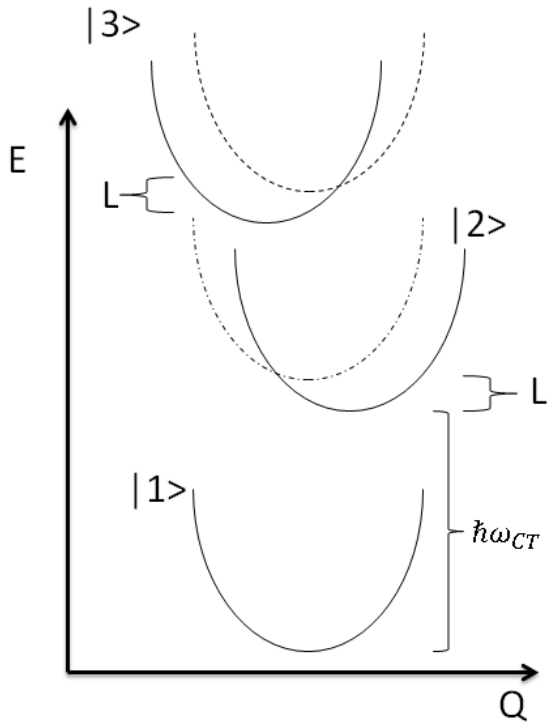

Figure 5.12: Potential energy surface diagram of symmetric dimer electronic eigenstates (|1>, |2>, |3>) perturbed by non-local coupling. The dashed lines represent the unperturbed excited electronic states. Adapted after ref.[23]

As shown in Figure 5.122, the effect of non-local coupling is to introduce displacements and lower the energy of the excited state potential energy surfaces of the electronic eigenstates. Upon vertical electronic excitation into the symmetry-allowed CT state (|2>) that state will relax by energy L. Therefore, the reorganization energy is equivalent to L and so those phonons that modulate the transfer integrals most strongly will have the highest reorganization energy. L has been recently calculated by our collaborators using DFT at three different levels of approximation[139]. In particular, the calculated transfer integrals and eph coupling constants can be affected greatly by the amount of non-local Hartree-Fock (HF) exchange included in the hybrid density functional used in the calculation[28,227]. This is still an ongoing research area and it is unclear what the appropriate % should be and so this further highlights the need for experimental verification of these values. A comparison between our experimentally-determined values and those calculated is displayed in Table 5.3.

Table 5.3: Comparison of non-local coupling (L) between experimental and theoretical calculations at three different levels of non-local Hartree-Fock (HF) exchange %.

Measured freq. (cm^{-1})	L (meV) This work	L_{calc} (meV) 0% HF	L_{calc} (meV) 25% HF	L_{calc} (meV) 35% HF	Type:
43	1.9	0.004	0.09	0.13	L: A/P- z-axis
47	1	1.4	6.8	10.5	L: A/P- z-axis
57	0.8	5.9	7.1	12.4	L: P- short axis
84	0.2	2	4.9	3.7	L: P- long axis
113	0.5	1.5	4	5.6	L: A- long axis
127.5	0.1	0.05	0.08	0.2	L: A- long axis
207	0.04	0.06	1.4	4	P: C=O bend out-of-plane
253.5	0.08	0.03	0.09	0.7	A/P doublet
273.5	0.2	0.01	0.009	0.003	P: C=O bend out-of-plane

Our measured values are lower than the calculated values for most of the phonons. More striking is that the phonon calculated to have the highest L is not the same as the one found from

experiment. According to the experiment, this phonon is the coupled out-of-phase libration at 43 cm^{-1} (Figure 5.6); according to the calculation it is the PMDA libration around its short-axis at 57 cm^{-1} (Figure 5.111). The experimental numbers seem to indicate that a lower amount of HF exchange will better simulate experiment. Despite the other differences, there are some good agreements between the coupling constants of phonons of frequencies ranging between 127-253 cm^{-1}.

Non-local coupling can serve to either increase or decrease the charge carrier mobility. As already pointed out, the total non-local reorganization energy is 1% of the total in the system. This small value means that non-local coupling will have a small effect in decreasing the charge carrier mobility. Thermal fluctuations of the transfer integral result in phonon-assisted transport[22,23]. The variance of the transfer integrals due to thermal fluctuations can be related to the coupling constants L by[23]

$$\sigma^2 = \sum_j \hbar\omega_j L_j \coth\left(\frac{\hbar\omega_j}{2k_B T}\right) \tag{5.10}$$

where σ^2 is the variance and ω_j is the frequency of the j^{th} phonon. Using equation 5.10 on our measured non-local coupling values, the variance in the transfer integral is 80 meV^2 at 80K and increases to 255 meV^2 at 300K. These values represent the scale of thermal fluctuations of the transfer integral projected along the c-axis of APMDA. In a hopping model the mobility is related to the transfer integral and the reorganization energy as follows[25]

$$\mu \propto t^2 \exp[-\lambda_{reorg}/k_B T] \tag{5.11}$$

This equation can be adjusted to account for thermal fluctuations of the transfer integral by[22]

$$\langle t^2 \rangle = t^2 + \sigma^2 \tag{5.12}$$

where $<t^2>$ represents the thermal average of the transfer integral. The transfer integral has been calculated along the stacking axis by our collaborators and is found to be 375 meV[65]. Using the

variance derived from the experimental values for L results in a 0.05% increase in the charge carrier mobility at 80K, compared to 0.2% at 300K. The standard deviation of these fluctuations is ~2% of the total transfer integral at 80K and 4% at 300K. The effect of non-local coupling on the transfer integral of APMDA is thus very small. It is worth noting that infrared-active phonons are also allowed by symmetry to modulate the charge transfer integral. However, the smallness of the coupling constants of the Raman active modes most likely means the effects of IR-active modes are equally small, thus not changing any conclusions arrived at in this project.

5.5.5 Intramolecular regime

In the intramolecular region the reorganization energy primarily comes from the higher-frequency in-plane C=C and C-C stretching phonons of anthracene and the C=O, C=C, and C-C stretching phonons of PMDA. These are also the same type of phonons (minus the C=O) that have the highest reorganization energies in the PnT1 system described in chapter 4. Polaron binding energies are determined for both anthracene and PMDA by $E_{pol}=\lambda_{reorg}/2$. E_{pol} for holes on anthracene was determined to be 58 meV and for electrons on PMDA to be 113 meV. The polaron binding energy has been studied in the past for anthracene by fitting gas-phase UPS spectra. There are multiple models available to fit the UPS spectra and each results in different E_{pol} values. A three-vibrational-mode fit to the UPS spectra using a Franck-Condon analysis gave an E_{pol} of 87 meV[124]. A more in-depth model using DFT that takes into account all of the Franck-Condon active modes gave a value of 68 meV[124]. This value agrees well with the value determined here using resonance Raman spectroscopy.

Table 5.4: Comparison of modes with the highest reorganization energies (λ_{reo}) between this work and prior work

Freq. (cm^{-1})	λ_{reorg} This work (meV)	λ_{reorg} Prior work[124] (meV)
1169	9	7
1257	14	11
1400	34	44
1555	54	64
E_{pol} (meV)	58	68

It should be noted that E_{pol} was computed in this work for the APMDA complex and not the gas phase anthracene molecule, as for the UPS data. It is unclear how E_{pol} changes between the free molecule and a complex with another type of molecule. There are certainly some geometry differences between the two situations which can lead to re-distribution of charge density on the molecule and therefore changes in eph coupling constants. Furthermore, due to the lower symmetry of the crystal other non-negligible anthracene active modes are present, such as the mode at 1410 cm^{-1}, that will alter the total reorganization energy. More likely, the closeness in the two reported values stems from the relatively weak nature of the intermolecular van der Waals forces. A study of other anthracene charge transfer compounds and mono-molecular anthracene using this model would help determine if the differences in E_{pol} values are solely model dependent or are a function of solid state and charge transfer perturbation. The E_{pol} value for PMDA of 113 meV obtained in this project is the first-ever determination of this quantity and is similar to that of TCNQ of 128 meV[64]. As stated earlier (chapter 2), the electron mobility in APMDA is higher than the measured hole mobility[162] by at least two orders of magnitude at 473K. Assuming a hopping model, because of the low relative magnitude of the intermolecular reorganization energy the higher E_{pol} of PMDA would mean an electron mobility lower than the hole mobility. However, the measurements show that the electron mobility is much greater than the hole mobility. The effective transfer integrals for both holes and electrons have been

calculated to be about the same in APMDA (t_{hole}~$t_{electron}$~50 meV).[139] Therefore, the observed hole mobility must indeed be dominated by the presence of deep hole traps as discussed by Karl and coworkers[162].

5.6 Conclusions

Using a time-dependent resonant Raman model to fit the experimental resonant Raman and absorption spectra of the CT exciton in APMDA the eph coupling constants, both local and non-local, were determined and compared with available theoretical and experimental estimates. It was found that there is likely some form of orientational disorder in APMDA at 80K due to the inhomogeneous broadening of the CT absorption lineshape. The non-local eph coupling constants were determined to be much lower in magnitude than the local eph constants; about 1% of the total eph coupling. Also, phonon-assisted charge transport via thermal fluctuations of the transfer integral was shown to also be very modest; having a standard deviation of 2% of the transfer integral. Theoretical estimates of the non-local coupling constants tended to overestimate the experimentally-derived parameters. Furthermore, the derived non-local constants showed that the most strongly coupled intermolecular phonons were the coupled librations of A-PMDA about the axis connecting the two molecules. This is in disagreement with the theoretical prediction. This is the first time that non-local coupling constants have been determined by experiment in mixed-stack charge transfer compounds.

Local eph constants were shown to be dominated by high-frequency in-plane double-bond stretching of the donor and acceptor molecules. The polaron binding energy of anthracene derived from the resonance Raman experiments was compared with values determined by other authors and shown to be similar. Also, the polaron binding energy of PMDA was determined for the first time and was shown to be greater in magnitude than that of anthracene.

This work is a major step forward in understanding the role of non-local electron-phonon coupling in CT compounds. Experiment is now able to determine the same non-local coupling constants that theory can predict. Having this ability will help guide current models to better describe charge transport in organic semiconductors. There is still a lot of work to be done, in particular, applying the time dependent resonance Raman model to either other PMDA- or anthracene-based CT compounds in order to compare the effect of acceptor and donor molecules on non-local coupling. It would be interesting to know if there are other charge transfer compounds with much larger non-local coupling and if so, to identify the determining factor for large or small non-local coupling.

CHAPTER 6: CONCLUSIONS

In this project the electronic and electron-phonon coupling have been successfully determined using Raman spectroscopy in various organic semiconducting charge transfer compounds. These experimental results have been compared with theoretical predictions and have been shown to agree well in the case of local electron-phonon coupling, but not in the case of non-local electron-phonon coupling. The need for experimental verification of theoretical predictions is essential for the development of accurate models to describe and better understand charge transport in organic semiconductors. This project sought to bridge the gap in the organic semiconducting charge transfer compounds world between theoretical development and what experiment can determine. In recent years there have been major theoretical developments in the understanding of the effects of electronic and electron-phonon coupling on intrinsic charge transport. Using Raman spectroscopy many of these parameters can be determined and studied alongside theory in order to improve our understanding of charge transport in charge transfer organic semiconductors, so that we can move towards the goal of a general model for charge transport in these important materials.

Chapter 4 focused on the effect of structure on the transfer integrals and local electron-phonon coupling in the PnT1 charge transfer compound system. It was found that as the number of donors increases the degree of charge transfer increases. Temperature-dependent measurements of the degree of transfer showed that it increased as temperature decreases. These results were corroborated by an increase in the transfer integral versus temperature as calculated by our collaborators. The increase in the degree of charge transfer was found to be due to a

decrease in the donor-acceptor distance. As the number of donor molecules increased, the donor-acceptor distance decreased. The decreased donor-acceptor distance enhanced the frontier orbital overlap of the donor and acceptor molecules. This was also corroborated by theoretical calculations of the transfer integral in PnT1, where it was shown to increase with number of donors in the compound. A larger transfer integral does not necessarily mean a larger mobility, because of the presence of electron-phonon coupling. Using resonance Raman spectroscopy the local electron-phonon coupling constants were determined for each resonant phonon. A redistribution of the magnitudes of the mode-specific electron-phonon coupling constants was observed due to changes in solid state environment between P1T1 and P3T1.The polaron binding energy was determined for both holes on perylene and electrons on TCNQ in PnT1. The perylene polaron binding energy was shown to be smaller in P3T1 than in P1T1. This was attributed to delocalization of the hole over the two perylene molecules in the stack. For TCNQ, the polaron binding energy was determined to be similar in each compound of the PnT1 system and is two times larger than the binding energy of perylene. Theoretical calculations of the polaron binding energy of TCNQ agreed with those determined in this system. However, an effort to connect the local electron-phonon coupling constants and the degree of charge transfer with the observed transport characteristics proved futile. The large polaron binding energy of TCNQ compared to perylene did not prevent P1T1 from being n-type. Also, the mobility of P1T1 was larger than those of the other two compounds despite it having the lowest degree of charge transfer and amount of electronic coupling. Only in P3T1 did our simplified picture of charge transport based on hopping transport yield results consistent with the observed hole mobility. Clearly, our understanding of charge transport based solely on these parameters is not sufficient. The inclusion of non-local electron-phonon coupling is one avenue forward.

In chapter 5, the focus turned to using resonance Raman spectroscopy more in depth to extract both local and non-local electron-phonon coupling constants in APMDA. Using measured resonance Raman spectra, a time-dependent resonance Raman model usually applied to excited states of molecules in solution was successfully utilized in order to determine the electron-phonon coupling constants. This was the first time that the non-local coupling constants were determined experimentally for mixed-stack charge transfer compounds. The calculated resonance Raman and absorption spectra of the resonance model fit well with the observed spectra. It was shown that non-local coupling in APMDA accounts for only ~1% of the total reorganization energy of the charge transfer exciton, despite displacements of excited state potential energy surfaces similar to those of high frequency intramolecular phonons. These values were compared with theoretical predictions, which were shown to overestimate the values of the coupling constants. Furthermore, experiment and theory identify different intermolecular phonons as having the largest non-local coupling constant. These results highlight that the theoretical framework for understanding non-local electron-phonon coupling is still under development. Polaron binding energies of anthracene and PMDA were determined and in the case of PMDA this appears to be the first determination of this material-specific constant. The polaron binding energy and mode-specific reorganization energies of anthracene were compared with previous studies and shown to agree.

Overall, in both studies on the charge transport microscopic parameters in PnT1 and APMDA, local electron-phonon coupling and electronic coupling derived by experiment and theory agree very well with one another. Evidence for this in this project is seen in the increase of the transfer integral and degree of charge transfer in PnT1 as donor-acceptor distance decreases and also in the agreement between the polaron binding energies of TCNQ and

anthracene in PnT1 and APMDA respectively. Although experimental results for local coupling agreed well with theory, non-local results did not agree particularly well. Besides the agreement in magnitude of a few non-local coupling constants of some weakly coupled phonons, major discrepancies exist, such as the identity of the phonon with the largest coupling constant and the overall magnitude of the coupling constants. Development in both our theoretical and experimental understanding in extracting non-local coupling constants is needed. On the theoretical side, there are significant deviations in results depending on specific DFT functional parameters such as the amount of non-local Hartree-Fock exchange. For experiment, additional measurements are needed for similar systems and further exploration into whether or not the reorganization energy measured for intermolecular phonons is necessarily equal to the non-local L parameter. The equality was based on a symmetric dimer system with no local electron-phonon coupling present, thus developing a more accurate model based on an asymmetric dimer system with both non-local and local electron-phonon coupling included will help identify if this equality indeed holds. Despite the developments needed, this project has helped move forward the goal of fully including non-local coupling into charge transport models by adding experimental constraints to the theoretical predictions of non-local coupling. Finally, once all of these intrinsic microscopic parameters are well understood, connecting them to explain and predict the observed charge carrier mobility in an organic charge transfer compound will help in the creation of cheap, superior, and efficient organic electronic devices tailored to any need.

REFERENCES

1. Dass, R. & Harrop, P. *Printed, Flexible And Organic Electronics Report*. (2014).

2. Sheats, J. R. Manufacturing and commercialization issues in organic electronics. *J. Mater. Res.* **19,** 1974–1989 (2011).

3. Shokaryev, I. *et al.* Electronic band structure of tetracene-TCNQ and perylene-TCNQ compounds. *J. Phys. Chem. A* **112,** 2497–502 (2008).

4. Hoth, C. N., Schilinsky, P., Choulis, S. A., Balasubramanian, S. & Brabec, C. J. in *Applications of Organic and Printed Electronics* 27–56 (Springer US, 2013).

5. Hösel, M., Søndergaard, R., Jørgensen, M. & Krebs, F. Fast Inline Roll-to-Roll Printing for Indium-Tin-Oxide-Free Polymer Solar Cells Using Automatic Registration. *Energy Technol.* **1,** 102–107 (2013).

6. Cantatore, E. in *Applications of Organic and Printed Electronics* vi (Springer US, 2013).

7. Fukuda, K. *et al.* Fully-printed high-performance organic thin-film transistors and circuitry on one-micron-thick polymer films. *Nat. Commun.* **5,** 4147 (2014).

8. Anthony, J. Functionalized acenes and heteroacenes for organic electronics. *Chem. Rev.* **106,** 5028–5048 (2006).

9. Himmelberger, S. *et al.* Role of Side-Chain Branching on Thin-Film Structure and Electronic Properties of Polythiophenes. *Adv. Funct. Mater.* (2015). doi:10.1002/adfm.201500101

10. Zan, H. W., Tsai, W. W., Lo, Y. R., Wu, Y. M. & Yang, Y. S. Pentacene-based organic thin film transistors for ammonia sensing. *IEEE Sens. J.* **12,** 594–601 (2012).

11. Sheraw, C. D. *et al.* Organic thin-film transistor-driven polymer-dispersed liquid crystal displays on flexible polymeric substrates. *Appl. Phys. Lett.* **80,** 1088–1099 (2002).

12. Baude, P. F. *et al.* Pentacene-based radio-frequency identification circuitry. *Appl. Phys. Lett.* **82,** 3964–3966 (2003).

13. Yuan, Y. *et al.* Ultra-high mobility transparent organic thin film transistors grown by an off-centre spin-coating method. *Nat. Commun.* **5,** 3005 (2014).

14. Takeya, J. *et al.* Very high-mobility organic single-crystal transistors with in-crystal conduction channels. *Appl. Phys. Lett.* **90,** 102120 (2007).

15. Podzorov, V. *et al.* Intrinsic Charge Transport on the Surface of Organic Semiconductors. *Phys. Rev. Lett.* **93,** 086602 (2004).

16. Lifshitz, N. & Luryi, S. Enhanced Channel Mobility in Polysilicon Thin Film Transistors. *IEEE Electron Device Lett.* **15,** 274 (1994).

17. Canali, C., Jacoboni, C., Nava, F., Ottaviani, G. & Alberigi-Quaranta, A. Electron drift velocity in silicon. *Phys. Rev. B* **12,** 2265–2284 (1975).

18. Ottaviani, G., Reggiani, L., Canali, C., Nava, F. & Alberigi-Quaranta, A. Hole drift velocity in silicon. *Phys. Rev. B* **12,** 3318–3329 (1975).

19. Kang, I., Yun, H., Chung, D. S., Kwon, S. & Kim, Y. Record High Hole Mobility in Polymer Semiconductors via Side-Chain Engineering. (2013).

20. Tseng, H. R. *et al.* High-mobility field-effect transistors fabricated with macroscopic aligned semiconducting polymers. *Adv. Mater.* **26,** 2993–2998 (2014).

21. Chabinyc, M. L. *et al.* Printing methods and materials for large-area electronic devices. *Proc. IEEE* **93,** 1491–1499 (2005).

22. Sánchez-Carrera, R. S., Paramonov, P., Day, G. M., Coropceanu, V. & Brédas, J.-L. Interaction of charge carriers with lattice vibrations in oligoacene crystals from naphthalene to pentacene. *J. Am. Chem. Soc.* **132,** 14437–46 (2010).

23. Coropceanu, V., Sánchez-Carrera, R. S., Paramonov, P., Day, G. M. & Brédas, J.-L. Interaction of Charge Carriers with Lattice Vibrations in Organic Molecular Semiconductors: Naphthalene as a Case Study. *J. Phys. Chem. C* **113,** 4679–4686 (2009).

24. McMahon, D. P. & Troisi, A. Evaluation of the external reorganization energy of polyacenes. *J. Phys. Chem. Lett.* **1,** 941–946 (2010).

25. Coropceanu, V. *et al.* Charge transport in organic semiconductors. *Chem. Rev.* **107,** 926–52 (2007).

26. Martinelli, N. G. *et al.* Influence of Structural Dynamics on Polarization Energies in Anthracene Single Crystals. *J. Phys. Chem. C* **114,** 20678–20685 (2010).

27. Coropceanu, V., Li, H., Winget, P., Zhu, L. & Brédas, J.-L. Electronic-Structure Theory of Organic Semiconductors: Charge-Transport Parameters and Metal/Organic Interfaces. *Annu. Rev. Mater. Res.* **43,** 63–87 (2013).

28. Fonari, A., Sutton, C., Brédas, J.-L. & Coropceanu, V. Impact of exact exchange in the description of the electronic structure of organic charge-transfer molecular crystals. *Phys. Rev. B* **90,** 1–6 (2014).

29. Smith, J. *et al.* Solution-processed small molecule-polymer blend organic thin-film transistors with hole mobility greater than 5 cm 2/Vs. *Adv. Mater.* **24,** 2441–2446 (2012).

30. Shirakawa, H., Louis, E. J., MacDiarmid, A. G., Chiang, C. K. & Heeger, A. J. Synthesis of electrically conducting organic polymers: halogen derivatives of polyacetylene, (CH)x. *J. Chem. Soc., Chem. Commun.* **1977,** 578–580 (1977).

31. Holliday, S., Donaghey, J. E. & McCulloch, I. Advances in charge carrier mobilities of semiconducting polymers used in organic transistors. *Chem. Mater.* **26,** 647–663 (2014).

32. Chen, H. *et al.* Highly π-extended copolymers with diketopyrrolopyrrole moieties for high-performance field-effect transistors. *Adv. Mater.* **24,** 4618–4622 (2012).

33. Fukuda, K., Takeda, Y., Mizukami, M., Kumaki, D. & Tokito, S. Fully solution-processed flexible organic thin film transistor arrays with high mobility and exceptional uniformity. *Sci. Rep.* **4,** 3947 (2014).

34. Usta, H. & Facchetti, A. in *Large Area and Flexible Electronics* (eds. Caironi, M. & Noh, Y.-Y.) 3–99 (Wiley-VCH Verlag GmbH and Co., 2015).

35. Zhou, J. *et al.* Solution-processed and high-performance organic solar cells using small molecules with a benzodithiophene unit. *J. Am. Chem. Soc.* **135,** 8484–8487 (2013).

36. Lin, Y., Li, Y. & Zhan, X. Small molecule semiconductors for high-efficiency organic photovoltaics. *Chem. Soc. Rev.* **41,** 4245 (2012).

37. Scriven, L. E. Physics and Applications of DIP Coating and Spin Coating. *MRS Proc.* **121,** 717 (1988).

38. Krebs, F. C. Polymer solar cell modules prepared using roll-to-roll methods: Knife-over-edge coating, slot-die coating and screen printing. *Sol. Energy Mater. Sol. Cells* **93,** 465–475 (2009).

39. Soeda, J. *et al.* Inch-Size Solution-Processed Single-Crystalline Films of High-Mobility Organic Semiconductors. *Appl. Phys. Express* **6,** 076503 (2013).

40. Welch, G. C. *et al.* A modular molecular framework for utility in small-molecule solution-processed organic photovoltaic devices. *J. Mater. Chem.* **21,** 12700 (2011).

41. Walker, B., Kim, C. & Nguyen, T. Q. Small molecule solution-processed bulk heterojunction solar cells. *Chem. Mater.* **23,** 470–482 (2011).

42. Sun, Y. *et al.* Solution-processed small-molecule solar cells with 6.7% efficiency. *Nat. Mater.* **11,** 44–48 (2011).

43. Sekine, C., Tsubata, Y., Yamada, T., Kitano, M. & Doi, S. Recent progress of high performance polymer OLED and OPV materials for organic printed electronics. *Sci. Technol. Adv. Mater.* **15,** 034203 (2014).

44. Aizawa, N. *et al.* Solution-processed multilayer small-molecule light-emitting devices with high-efficiency white-light emission. *Nat. Commun.* **5,** 5756 (2014).

45. Pope, M. & Swenberg, C. E. *Electronic Processes in Organic Crystals*. (Oxford University Press, 1982).

46. Silnish, E. & Capek, V. *Organic Molecular Crystals: Interaction, Localization, and Transport Phenomena*. (American Institute of Physics, 1997).

47. Hains, A. W., Liang, Z., Woodhouse, M. a. & Gregg, B. a. Molecular semiconductors in organic photovoltaic cells. *Chem. Rev.* **110,** 6689–6735 (2010).

48. Bässler, H. & Köhler, A. Charge transport in organic semiconductors. *Top. Curr. Chem.* **312,** 1–65 (2012).

49. Dougherty, T. J. & Pucci, M. J. in *Antibiotic Discovery and Development* 801–802 (2012).

50. London, F. Zur Theorie und Systematik der Molekularkräfte. *Zeitchrift für Phys.* **63,** 245–279 (1930).

51. Silinsh, E. A. & Capek, V. *Organic Molecular Crystals: Their Electronic State*. (Springer-Verlag Berlin Heidelberg, 1980). doi:10.1007/978-3-642-81464-8

52. Wolf, H. C. Die niedersten elektronischen Anregungszustände des Anthracen-Kristalls. *Zeitschrift für Naturforsch. A* **13,** 414–419 (1958).

53. Schein, L., Duke, C. & McGhie, A. Observation of the Band-Hopping Transition for Electrons in Naphthalene. *Phys. Rev. Lett.* **40,** 197–200 (1978).

54. Karl, N. & Marktanner, J. Electron and Hole Mobilities in High Purity Anthracene Single Crystals. *Mol. Cryst. Liq. Cryst.* **355,** 149–173 (2001).

55. Sze, S. M. *Physics of Semiconductor Devices*. (John Wiley & sons, Inc, 1969).

56. Hubbard, J. Generalized Wigner lattices in one dimension and some applications to tetracyanoquinodimethane (TCNQ) salts. *Phys. Rev. B* **17,** 494 (1978).

57. Schowerer, M. & Wolf, H. C. *Organic Molecular Solids*. (Wiley-VCH Verlag GmbH and Co., 2007).

58. Jerome, D., Mazaud, A., Ribault, M. & Bechgaard, K. Superconductivity in a synthetic organic conductor (TMTSF)2PF6. *J. Phys. Lett.* **41,** 95–98 (1980).

59. Torrance, J., Vazquez, J., Mayerle, J. & Lee, V. Discovery of a Neutral-to-Ionic Phase Transition in Organic Materials. *Phys. Rev. Lett.* **46,** 253–257 (1981).

60. Hasegawa, T., Mattenberger, K., Takeya, J. & Batlogg, B. Ambipolar Field-Effect Carrier Injections in Organic Mott Insulators. *Phys. Rev. B* **69,** 245115 (2004).

61. Wu, H. D., Wang, F. X., Xiao, Y. & Pan, G. B. Perparation and Ambipolar Transistor Characteristics of Co-Crystal Microrods of Dibenzotetrathiafulvalene and Tetracyanoquinodimethane. *J. Mater. Chem. C* **1,** 2286–2289 (2013).

62. Park, S. K. *et al.* Tailor-Made Highly Luminescent and Ambipolar Transporting Organic Mixed Stacked Charge-Transfer Crystals: An isometric Donor-Acceptor Approach. *J. Am. Chem. Soc.* **135,** 4757–4764 (2013).

63. Vermeulen, D. *et al.* Charge Transport Properties of Perylene-TCNQ Crystals : The Effect of Stoichiometry. *J. Phys. Chem. C* **118,** 24688–24696 (2014).

64. Zhu, L. *et al.* Prediction of remarkable ambipolar charge-transport characteristics in organic mixed-stack charge-transfer crystals. *J. Am. Chem. Soc.* **134,** 2340–2347 (2012).

65. Zhu, L. *et al.* Electronic properties of mixed-stack organic charge-transfer crystals. *J. Phys. Chem. C* **118,** 14150–14156 (2014).

66. Zaumseil, J. & Sirringhaus, H. Electron and Ambipolar Transport in Organic Field-Effect Transistors. *ChemInform* **38,** 1296–1323 (2007).

67. Sakai, M. *et al.* Ambipolar Field-Effect Transistor Characteristics of (Bedt-TTF)-TCNQ Crystals and Metal-like Conduction Induced by a Gate Electric Field. *Phys. Rev. B* **76,** 045111–045115 (2007).

68. Takahashi, Y. *et al.* Tuning of Electron Injections for N-Type Organic Transistor Based on Charge-Transfer Compounds. *Appl. Phys. Lett.* **86,** 063504–063506 (2005).

69. Takahashi, Y., Hasegawa, T., Abe, Y., Tokura, Y. & Saito, G. Organic Metal Electrodes for Controlled P- and N-Type Carrier Injections in Organic Field-Effect Transistors. *Appl. Phys. Lett.* **88,** 073504–073506 (2006).

70. Hasegawa, T. & Takeya, J. Organic field-effect transistors using single crystals. *Sci. Technol. Adv. Mater.* **10,** 024314 (2009).

71. Mulliken, R. S. & Person, W. B. Donor-Acceptor Complexes. *Annu. Rev. Phys. Chem.* **13,** 107–126 (1961).

72. Cohen, M. J., Coleman, L. B., Garito, a. F. & Heeger, a. J. Electrical conductivity of tetrathiofulvalinium tetracyanoquinodimethan (TTF) (TCNQ). *Phys. Rev. B* **10,** 1298–1307 (1974).

73. Coleman, L. B. *et al.* Superconducting fluctuations and the Peierls instability in an organic solid. *Solid State Commun.* **12,** 1125–1132 (1973).

74. Tomkiewicz, Y., Taranko, A. R. & Torrance, J. R. Role of the Donor and Acceptor Chains in the Metal-Insulator Transition in TTF-TCNQ (Tetrathiafulvalene Tetracyanoquinodimethane). *Phys. Rev. Lett.* **36,** 751–754 (1976).

75. Torrance, J. B. An Overview of Organic Charge-Transfer Solids: Insulators, Metals, and the Neutral-Ionic Transition. *Mol. Cryst. Liq. Cryst.* **126,** 55–67 (1985).

76. Mitani, T. *et al.* Electric Conductivity and Phase Diagram of a Mixed-Stack Charge-Transfer Crystal: Tetrathiafulvalene-p-Chloranil. *Phys. Rev. B* **35,** 427 (1987).

77. Torrance, J. B. The difference between metallic and insulating salts of tetracyanoquinodimethone (TCNQ): how to design an organic metal. *Acc. Chem. Res.* **12,** 79–86 (1979).

78. Soos, Z. & Mazumdar, S. Neutral-ionic interface in organic charge-transfer salts. *Phys. Rev. B* **18,** 1991–2003 (1978).

79. Girlando, A., Pecile, C. & Painelli, A. VIBRATIONAL SPECTROSCOPY OF MIXED STACK ORGANIC SEMICONDUCTORS: COMPARISON WITH SEGREGATED STACK SYSTEMS. *Le Journal de Physique Colloques* **44,** C3–1547–C3–1550 (1983).

80. Soos, Z. G. Molecular energies in partly charged organic solids. *Chem. Phys. Lett.* **63,** 179–183 (1979).

81. Torrance, J., Scott, B. & Kaufman, F. Optical properties of charge transfer salts of tetracyanoquinodimethane (TCNQ). *Solid State Commun.* **88,** 971–975 (1975).

82. Lipari, N. O. *et al.* Electron-intramolecular vibration coupling in TTF-TCNQ systems. *Int. J. Quantum Chem.* **12,** 583–594 (1977).

83. Kistenmacher, T. J. *et al.* DBTTF-TCNQ: A fractionally-charged organic salt with a mixed-stack crystalline motif. *Solid State Commun.* **39,** 415–417 (1981).

84. Matsuzaki, S., Kuwata, R. & Toyoda, K. Raman spectra of conducting TCNQ salts; estimation of the degree of charge transfer from vibrational frequencies. *Solid State Commun.* **33,** 403–405 (1980).

85. Chappell, J. S., Bloch, A. N., Bryden, W. A. & Maxfield, M. Degree of charge transfer in organic conductors by infrared absorption spectroscopy. *J. Am. Chem. Soc.* 2442–2443 (1981). at <http://pubs.acs.org/doi/abs/10.1021/ja00399a066>

86. Tanaka, M., Shimizu, M., Saito, Y. & Tanaka, J. Raman spectra of radical ion DBTTF complexes; relation between raman frequency and formal charge. *Chemical Physics Letters* **125,** 594–596 (1986).

87. Meneghetti, M. & Pecile, C. Charge–transfer organic crystals: Molecular vibrations and spectroscopic effects of electron–molecular vibration coupling of the strong electron acceptor TCNQF4. *J. Chem. Phys.* **84,** 4149 (1986).

88. Bozio, R. & Pecile, C. *Spectroscopy of Advanced Materials: Advances in Spectroscopy Volume 19*. (1991).

89. Painelli, a. & Girlando, a. Electron–molecular vibration (e–mv) coupling in charge-transfer compounds and its consequences on the optical spectra: A theoretical framework. *J. Chem. Phys.* **84,** 5655 (1986).

90. Painelli, a. & Girlando, a. Mixed regular stack charge–transfer crystals: Fundamental microscopic parameters from optical spectra. *J. Chem. Phys.* **87,** 1705–1711 (1987).

91. Zhu, L., Kim, E., Yi, Y. & Brédas, J. Charge Transfer in Molecular Complexes with 2, 3, 5, 6-Tetrafluoro-7, 7, 8, 8-tetracyanoquinodimethane (F4-TCNQ): A Density Functional Theory Study. *Chem. Mater.* **23,** 5149–5159 (2011).

92. Kistenmacher, T. J., Emge, T. J., Bloch, A. N. & Cowan, D. O. Structure of the Red, Semiconducting Form of 4, 4', 5, 5'-Tetramethyl-Δ2, 2'-bi-1, 3-diselenole-7, 7, 8, 8-Tetracyano-p-quinodimethane, Tmtsf–Tcnq. *Acta Crystallogr. Sect. B Struct. Crystallogr. Cryst. Chem.* **38,** 1193–1199 (1982).

93. Flandrois, S. & Chasseau, D. Longueurs de liaison et transfert de charge dans les sels du tetracyanoquinodimethane (TCNQ). *Acta Crystallogr. Sect. B …* **33,** 2744–2750 (1977).

94. Weyl, C., Engler, E. M., Bechgaard, K., Jehanno, G. & Etemad, S. Diffuse X-Ray Scattering in the Metallaic State of TSeF-TCNQ and HMTSeF-TCNQ. *Solid State Commun.* **19,** 925–930 (1976).

95. Girlando, A., Marzola, F., Pecile, C. & Torrance, J. B. Vibrational spectroscopy of mixed stack organic semiconductors: Neutral and ionic phases of tetrathiafulvalene–chloranil (TTF–CA) charge transfer complex. *J. Chem. Phys.* **79,** 1075 (1983).

96. Rice, M. J. Towards the experimental determination of the fundamental microscopic parameters of organic ion-radical compounds. *Solid State Commun.* **31,** 93–98 (1979).

97. Wong, K. Y. Charge-transfer-induced IR absorptions in mixed-valence compounds. *Inorg. Chem.* **23,** 1285–1290 (1984).

98. Lipari, N. O. Electron–vibration interactions in benzene and deuterobenzene. *J. Chem. Phys.* **65,** 1165 (1976).

99. Duke, C., Lipari, N. & Pietronero, L. The interaction of electrons with the molecular vibrations of benzene. *Chem. Phys. Lett.* **30,** 415–420 (1975).

100. Girlando, A., Bozio, R., Pecile, C. & Torrance, J. Discovery of vibronic effects in the Raman spectra of mixed-stack charge-transfer crystals. *Phys. Rev. B* **26,** 2306–2309 (1982).

101. Bozio, R., Feis, a., Zanon, I. & Pecile, C. Resonance Raman scattering of a Peierls–Hubbard dimer. *J. Chem. Phys.* **91,** 13 (1989).

102. Bozio, R. Resonance Raman scattering of Peierls Hubbard systems. *Synth. Met.* **42,** 1899–1902 (1991).

103. Pedron, D., Speghini, a., Mulloni, V. & Bozio, R. Coupling of electrons to intermolecular phonons in molecular charge transfer dimers: A resonance Raman study. *J. Chem. Phys.* **103,** 2795 (1995).

104. Tanase, C., Meijer, E. J., Blom, P. W. M. & de Leeuw, D. M. Unification of the Hole Transport in Polymeric Field-Effect Transistors and Light-Emitting Diodes. *Phys. Rev. Lett.* **91,** 216601 (2003).

105. Jurchescu, O. D., Bass, J. & Palstra, T. T. M. Effect of impurities on the mobility of single crystal pentacene. *Appl. Phys. Lett.* **84,** 3061 (2004).

106. Karl, N. in *Crystals (Growth, Properties, and Applications)* (Springer-Verlag Berlin Heidelberg, 1980).

107. Schein, L. Electron drift mobilities over wide temperature ranges in anthracene, deuterated anthracene and As 2 S 3. *Chem. Phys. Lett.* 571–575 (1977). at <http://www.sciencedirect.com/science/article/pii/0009261477850951>

108. Cheng, Y. C. *et al.* Three-dimensional band structure and bandlike mobility in oligoacene single crystals: A theoretical investigation. *J. Chem. Phys.* **118,** 3764–3774 (2003).

109. Holstein, T. Studies of Polaron Motion. *Ann. Phys. (N. Y).* **8,** 343–389 (1959).

110. Holstein, T. Studies of Polaron Motion. *Ann. Phys. (N. Y).* **8,** 325–342 (1959).

111. Lipari, N. O. Electron–vibration interactions in benzene and deuterobenzene. *J. Chem. Phys.* **65,** 1165 (1976).

112. Conwell, E. Band transport in quasi-one-dimensional conductors in the phonon-scattering regime and application to tetrathiofulvalene-tetracyanoquinodimethane. *Phys. Rev. B* **22,** 1761–1780 (1980).

113. Hubbard, J. Electron Correlations in Narrow Energy Bands. *Proc. R. Soc. A Math. Phys. Eng. Sci.* **276,** 238–257 (1963).

114. Schultz, T. D. in *The Physics and Chemistry of Low Dimensional Solids* (ed. Alcâcer, L.) 1–30 (D. Reidel Publishing Company, 1980).

115. Singleton, J. Why do physicists love charge-transfer salts? *J. Solid State Chem.* **168,** 675–689 (2002).

116. Conwell, E. in *Semiconductors and Semimetals Vol. 27* (ed. Conwell, E.) 215–292 (Academic Press, INC., 1988).

117. Ashcroft, N. W. & Mermin, D. N. *Solid State Physics*. (Thomson Learning Inc., 1976).

118. Chadi, D. J. & Cohen, M. L. Tight binding calculations of the valence bands of diamond and zincblende crystals. *Phys. Status Solidi* **68,** 405–419 (1975).

119. Dresselhaus, G. & Dresselhaus, M. S. Fourier expansion for the electronic energy bands in silicon and germanium. *Phys. Rev.* **160,** 649–679 (1967).

120. Tomboulian, D. & Bedo, D. Absorption and Emission Spectra of Silicon and Germanium in the Soft X-Ray Region. *Phys. Rev.* **1196,** (1956).

121. McGarry, K. a. *et al.* Rubrene-based single-crystal organic semiconductors: Synthesis, electronic structure, and charge-transport properties. *Chem. Mater.* **25,** 2254–2263 (2013).

122. Huang, K. & Rhys, a. Theory of Light Absorption and Non-Radiative Transitions in F-Centres. *Proc. R. Soc. A Math. Phys. Eng. Sci.* **204,** 406–423 (1950).

123. Duke, C. B., Malik, F. B. & Firk, F. W. K. Boson-Broadened Photonuclear Reactions in Light Nuclei. *Phys. Rev.* **157,** 879 (1967).

124. Malagoli, M., Coropceanu, V., Da Silva Filho, D. a. & Brédas, J. L. A multimode analysis of the gas-phase photoelectron spectra in oligoacenes. *J. Chem. Phys.* **120,** 7490–7496 (2004).

125. Champion, P. M. & Albrecht, A. C. On band shapes of electronic transitions in the multimode weak coupling limit. *J. Chem. Phys.* **72,** 6498 (1980).

126. Marcus, R. a. & Sutin, N. Electron transfers in chemistry and biology. *Biochim. Biophys. Acta - Rev. Bioenerg.* **811,** 265–322 (1985).

127. Coropceanu, V., Li, Y., Yi, Y., Zhu, L. & Brédas, J.-L. Intrinsic charge transport in single crystals of organic molecular semiconductors: A theoretical perspective. *MRS Bull.* **38,** 57–64 (2013).

128. Norton, J. E. & Brédas, J. L. Polarization energies in oligoacene semiconductor crystals. *J. Am. Chem. Soc.* **130,** 12377–12384 (2008).

129. Girlando, A. *et al.* Peierls and Holstein carrier-phonon coupling in crystalline rubrene. *Phys. Rev. B* **82,** 035208 (2010).

130. Hasegawa, S. *et al.* Intermolecular energy- band dispersion in oriented thin films of bis (1, 2, 5-thiadiazolo)-p-quinobis (1, 3-dithiole) by angle-resolved photoemission. *J. Chem. Phys.* **100,** 6969–6974 (1994).

131. Kera, S., Yamane, H. & Ueno, N. First-principles measurements of charge mobility in organic semiconductors: Valence hole-vibration coupling in organic ultrathin films. *Prog. Surf. Sci.* **84,** 135–154 (2009).

132. Duhm, S. *et al.* Charge Reorganization Energy and Small Polaron Binding Energy of Rubrene Thin Films by Ultraviolet Photoelectron Spectroscopy. *Adv. Mater.* **24,** 901–905 (2012).

133. Gruhn, N. & Filho, D. da S. The vibrational reorganization energy in pentacene: molecular influences on charge transport. *J. …* **1347,** 7918–7919 (2002).

134. Li, Y., Coropceanu, V. & Brédas, J. L. Thermal narrowing of the electronic bandwidths in organic molecular semiconductors: Impact of the crystal thermal expansion. *J. Phys. Chem. Lett.* **3,** 3325–3329 (2012).

135. Cheng, Y.-C. & Silbey, R. J. A unified theory for charge-carrier transport in organic crystals. *J. Chem. Phys.* **128,** 114713 (2008).

136. Beratan, D. N. *et al.* Steering electrons on moving pathways. *Acc. Chem. Res.* **42,** 1669–1678 (2009).

137. Troisi, A. & Orlandi, G. Dynamics of the intermolecular transfer integral in crystalline organic semiconductors. *J. Phys. Chem. A* **110,** 4065–4070 (2006).

138. Li, Y., Coropceanu, V. & Brédas, J.-L. Nonlocal electron-phonon coupling in organic semiconductor crystals: the role of acoustic lattice vibrations. *J. Chem. Phys.* **138,** 204713 (2013).

139. Fonari, A. *et al.* The impact of exact exchange in the description of vibrational properties of organic charge-transfer molecular crystals. In preparation (2015).

140. Pedron, D. & Lavina, S. Coupling of charge-transfer transitions to low wavenumber phonons in quasi-one-dimensional radical ion salts: resonance Raman study of tetraethylammonium. *J. Raman …* **913,** 907–913 (1998).

141. Tickle, I. & Prout, C. Molecular complexes. Part XVII. Crystal and molecular structure of perylene–7, 7, 8, 8-tetracyanoquinodimethane molecular complex. *J. Chem. Soc. Perkin Trans. 2* **2,** 720–723 (1973).

142. Hanson, A. W. 7, 7, 8, 8-Tetracyanoquinodimethane (perylene) 2-perylene. *Acta Crystallogr. Sect. B Struct. Crystallogr. Cryst. Chem.* **34,** 2339–2341 (1978).

143. Laudise, R. A., Kloc, C., Simpkins, P. G. & Siegrist, T. Physical Vapor Growth of Organic Semiconductors. *J. Cryst. Growth* **187,** 449–454 (1998).

144. Prout, C. K. & Mayoh, B. Molecular Complexes. Part 13.-Influence of charge transfer interactions on the structures of π-π* electron donor-acceptor molecular complexes. *J. Chem. Soc. Faraday Trans. 2* **68,** 1072–1082 (1972).

145. Bandrauk, A. Optical and Raman spectra of single crystals of perylene-TCNQ charge transfer complexes. *Can. J. Chem.* **60,** 588–595 (1982).

146. Doan Truong, K. & Bandrauk, A. D. A new TCNQ complex: (Perylene)3 TCNQ. *Chem. Phys. Lett.* **44,** 232–235 (1976).

147. Bandrauk, A. & Truong, K. Raman spectra of solid perylene–TCNQ complexes. *J. Raman Spectrosc.* **8,** 5–10 (1979).

148. Bandrauk, A., Truong, K. & Carlone, C. Temperature dependence of single crystal raman spectra of the complex (perylene) 3 TCNQ. *Chem. Phys.* **66,** 293–301 (1982).

149. Ishii, K., Yakushi, K., Kuroda, H. & Inokuchi, H. Reflection and Photoconduction Spectra of the Single-Crystals of Perylene-Tcnq 1-1 and 3-1 Molecular-Complexes. *B. Chem. Soc. Jpn* (1984). at <http://pdf.lookchem.com/pdf/22/5a78eafd-9499-496d-a07a-c39e4e58fca2.pdf>

150. Ida, T., Yakushi, K. & Kuroda, H. Pressure dependence of the polarized reflectance spectrum of the solid charge-transfer complex, perylene–TCNQ: Estimation of microscopic parameters. *J. Chem. Phys.* **91,** 3450 (1989).

151. Sato, N., Inokuchi, H. & Silinsh, E. a. Reevaluation of electronic polarization energies in organic molecular crystals. *Chem. Phys.* **115,** 269–277 (1987).

152. Chen, E. C. M. & Wentworth, W. E. A comparison of experimental determinations of electron affinities of pi charge transfer complex acceptors. *J. Chem. Phys.* **63,** 3183 (1975).

153. Boeyens, J. C. A. & Herbstein, F. H. Molecular Compounds and Complexes. III. The Crystal Structures of the Equimolar π-Molecular Compounds of Anthracene and Perylene with Pyromellitic Dianhydride. *J. Phys. Chem.* **169,** 2160–2176 (1964).

154. Eckhardt, C. J. & Merski, J. Piezomodulation spectroscopy of molecular crystals. II. The pyromellitic dianhydride anthracene electron donor – acceptor complex. *J. Chem. Phys.* **75,** 3705–18 (1981).

155. Haarer, D. & Karl, N. Charge-transfer-absorption, CT-emission- and ESR-spectroscopy with zone-refined crystals of anthracene-pyromellitic dianhydride. *Chemical Physics Letters* **21,** 49–53 (1973).

156. Brillante, A. & Philpott, M. R. Reflection and absorption spectra of singlet charge transfer excitons in anthracene–PMDA crystals. *J. Chem. Phys.* **72,** 4019 (1980).

157. Haarer, D. Zero-phonon lines in the singlet spectrum of the charge transfer crystal anthracene-PMDA: Experimental evidence and model calculations. *J. Chem. Phys.* **67,** 4076 (1977).

158. Haarer, D. Electric field induced transition in the charge-transfer exciton band of anthracene-PMDA. *Chem. Phys. Lett.* **31,** 192–194 (1975).

159. Syme, R. W., Morawitz, H. & Macfarlane, R. M. Raman scattering from the molecular charge transfer crystal anthracene-PMDA. *Solid State Commun.* **32,** 1059–1063 (1979).

160. Munn, R. W. & Phillips, R. J. Dielectric Theory of Weak charge-Transfer Crystals II. Polarization Energies. *Chem. Phys.* **135,** 15–26 (1989).

161. Karl, N., Sato, N., Seki, K. & Inokuchi, H. UV photoelectron spectroscopy of several one- and two-component organic photoconductors. *J. Chem. Phys.* **77,** 4870 (1982).

162. Karl, N. & Ziegler, J. Generation and Transport of Charge Carriers in the Charge-Transfer Complex Anthracene-Pyromellitic-Dianhydride. *Chem. Phys. Lett.* **32,** 438–442 (1975).

163. Raman, C. V. & Krishnan, K. S. The Optical Analog of the Compton Effect. *Nature* **121,** 711 (1928).

164. Kramers, H. a. & Heisenberg, W. Über die Streuung von Strahlung durch Atome. *Zeitschrift für Phys.* **31,** 681–708 (1925).

165. Dirac, P. A. M. The Quantum Theory of Dispersion. *Proc. R. Soc. A Math. Phys. Eng. Sci.* **114,** 710–728 (1927).

166. Albrecht, A. C. On the Theory of Raman Intensities. *J. Chem. Phys.* **34,** 1476 (1961).

167. Loudon, R. The Raman Effect in Crystals. *Adv. Phys.* **13,** 423–482 (1964).

168. Cardona, M. & Yu, P. *Fundamentals of Semiconductors*. (Springer Berlin Heidelberg, 2010).

169. Jackson, J. D. *Classical Electrodynamics*. (Wiley, 1999).

170. Kelley, A. M. *Condensed-Phase Molecular Spectroscopy and Photophysics*. (Wiley, 2013).

171. Heller, E. J. The Semiclassical Way to Molecular Spectroscopy. *Acc. Chem. Res.* **14,** 368–375 (1981).

172. Heller, E. J., Sundberg, R. L. & Tannor, D. Simple Aspects of Raman-Scattering. *J. Phys. Chem.* **86,** 1822–1833 (1982).

173. Herzberg, G. & Teller, E. No Title. *Z. Phys. Chem. B.* **21,** 410 (1933).

174. Tannor, D. J. & Heller, E. J. Polyatomic Raman scattering for general harmonic potentials. *J. Chem. Phys.* **77,** 202 (1982).

175. Lee, S.-Y. & Heller, E. J. Time-Dependent Theory of Raman Scattering. *J. Chem. Phys.* **71,** 4777–4788 (1979).

176. Myers, a B. 'Time-dependent' resonance Raman theory. *J. Raman Spectrosc.* **28,** 389–401 (1997).

177. Myers, A. B. Resonance Raman Intensities and Charge-Transfer Reorganization Energies. *Chem. Rev.* **96,** 911–926 (1996).

178. Myers, A. B. Resonance Raman Intensity Analysis of Excited-State Dynamics. *Acc. Chem. Res.* **30,** 519–527 (1997).

179. Myers, A. B., Mathies, R. a., Tannor, D. J. & Heller, E. J. Excited state geometry changes from preresonance Raman intensities: Isoprene and hexatriene. *J. Chem. Phys.* **77,** 3857–3866 (1982).

180. Myers, A. B. & Mathies, R. a. in *Biological Applications of Raman Spectroscopy* (ed. Spiro, T. G.) 1–58 (Wiley-Interscience, 1987).

181. Egolf, D. S., Waterland, M. R. & Kelley, A. M. Resonance Raman Intensity Analysis of the Carbazole / Tetracyanoethylene Charge-Transfer Complex: Mode-Specific Reorganization Energies for a Hole-Transport Molecule. *J. Phys. Chem. B* **104,** 10727–10737 (2000).

182. Doorn, S. K. & Hupp, J. T. Preresonance Raman studies of metal-to-ligand charge transfer in (NH3)4Ru(2,2'-bipyridine)2+. In situ bond length changes, force constants, and reorganization energies. *J. Am. Chem. Soc.* **111,** 4704–4712 (1989).

183. Giokas, P. G. *et al.* Spectroscopy and Dynamics of Phosphonate-Derivatized Ruthenium Complexes on TiO 2. *J. Phys. Chem. C* **117,** 812–824 (2013).

184. Hupp, J. T. & Williams, R. D. Using resonance Raman spectroscopy to examine vibrational barriers to electron transfer and electronic delocalization. *Acc. Chem. Res.* **34,** 808–817 (2001).

185. Goetz, K. P. *et al.* Freezing-in orientational disorder induces crossover from thermally-activated to temperature-independent transport in organic semiconductors. *Nat. Commun.* **5,** 5642 (2014).

186. Macfarlane, R. M. & Ushioda, S. Raman study of orientational disorder in the molecular charge-transfer crystals naphthalene–TCNB and naphthalene–PMDA. *J. Chem. Phys.* **67,** 3214 (1977).

187. Mukamel, S. *Principles of Nonlinear Optical Spectroscopy*. (Oxford University Press, 1995).

188. Myers Kelley, A. Resonance Raman Intensity Analysis of Vibrational and Solvent Reorganization in Photoinduced Charge Transfer. *J. Phys. Chem. A* **103,** 6891–6903 (1999).

189. Cardona, M. *Light Scattering in Solids II: Basic Concepts and Instrumentation*. (Springer-Verlag, 1982).

190. Grimsditch, M. & Ramdas, A. Brillouin scattering in diamond. *Phys. Rev. B* **11,** 3139–3148 (1975).

191. Grimsditch, M. & Ramdas, A. Elastic and elasto-optic constants of rutile from a Brillouin scattering study. *Phys. Rev. B* **14,** (1976).

192. Richter, W. *Resonant Raman scattering in semiconductors*. (1976). at <http://link.springer.com/chapter/10.1007/BFb0121253>

193. Ray, K. & McCreery, R. Simplified calibration of instrument response function for Raman spectrometers based on luminescent intensity standards. *Appl. Spectrosc.* **51,** (1997).

194. Fryling, M., Frank, C. & McCreery, R. Intensity calibration and sensitivity comparisons for CCD/Raman spectrometers. *Appl. Spectrosc.* **47,** 1965–1974 (1993).

195. Mathies, R. a. Biological Applications of Resonance Raman Spectroscopy in the Visible and Ultraviolet: Visual Pigments, Purple Membrane, and Nucleic Acids. *Chem. Biochem. Appl. Lasers* **4,** 55–99 (1979).

196. Fateley, W. G. & Dollish, F. R. *Infrared and Raman Spectroscopy Rules for Molecular and Lattice Vibrations*. (Wiley-Interscience, 1972).

197. Harris, D. C. & Bertolucci, M. D. *Symmetry and spectroscopy: an introduction to vibrational and electronic spectroscopy*. (Oxford University Press, 1978).

198. Pennelly, R. & Eckhardt, C. Quasi-metallic reflection spectra of TCNQ single crystals. *Chem. Phys.* **12,** 89–105 (1976).

199. Lowitz, D. a. Pople-like SCF—LCAO—MO Treatment of 77′,88′-Tetracyanoquinodimethan and Its Univalent Anion. *J. Chem. Phys.* **46,** 4698 (1967).

200. Hochstrasser, R. The Crystal Spectrum of Perylene. *Can. J. Chem.* **39,** (1961).

201. Tanaka, J., Tanaka, M. & Kawai, T. Electronic spectra and electronic structure of TCNQ complexes. *Bull. Chem. Soc. Jpn.* **49,** 2358 (1976).

202. Jiang, X., Li, Z., Sun, C. & Zhang, X. Study of electron transfer process of TCNQ under external electric field. *Int. J. Phys. Sci.* **7,** 901–905 (2012).

203. Chi, C. & Nixon, E. Resonance Raman studies of RbTCNQ and KTCNQ. *Spectrochim. Acta Part A Mol. Spectrosc.* **319,** 1739–1747 (1975).

204. Hoekstra, a., Spoelder, T. & Vos, a. The crystal structure of rubidium–7,7,8,8-tetracyanoquinodimethane, Rb–TCNQ, at –160°C. *Acta Crystallogr. Sect. B Struct. Crystallogr. Cryst. Chem.* **28,** 14–25 (1972).

205. Khatkale, M. S. & Devlin, J. P. The vibrational and electronic spectra of the mono-, di-, and trianon salts of TCNQ. *J. Chem. Phys.* **70,** 1851 (1979).

206. Vermeulen, D. *et al.* Charge transport properties of perylene-TCNQ crystals : The effect of stoichiometry SI.

207. Davydov, A. S. The Theory of Molecular Excitons. *Sov. Phys. Uspekhi* **82,** 145–178 (1964).

208. Ong, K. K., Jensen, J. O. & Hameka, H. F. Theoretical studies of the infrared and Raman spectra of perylene. *J. Mol. Struct. THEOCHEM* **459,** 131–144 (1999).

209. Hochstrasser, R. M. & Nyi, C. a. Dynamical effects from resonance Raman and fluorescence studies of the molecular exciton system perylene. *J. Chem. Phys.* **72,** 2591 (1980).

210. White, K., Brose, K. & Eckhardt, C. Assignment of the lattice modes in TCNQ0 single crystals. *J. Chem. …* **0304,** 5551–5559 (1986).

211. Fuke, K., Kaya, K., Kajiwara, T. & Nagakura, S. The polarized reflection and absorption spectra of perylene crystals in monomeric and dimeric forms. *J. Mol. Spectrosc.* **63,** 98–107 (1976).

212. Tanaka, J., Kishi, T. & Tanaka, M. Electronic Spectra of Perylene Crystals. *Bull. Chem. Soc. Jpn.* **47,** 2376–2381 (1974).

213. Markel, F., Ferris, N. S., Could, I. R. & Myers, A. B. Mode-Specific Vibrational Reorganization Energies Accompanying Photoinduced Electron Transfer in the Hexamethylbenzene/Tetracyanoethylene Charge-Transfer Complex. 6208–6219 (1992).

214. Rice, M. J., Pietronero, L. & Brüesch, P. Phase phonons and intramolecular electron-phonon coupling in the organic linear chain semiconductor TEA(TCNQ)2. *Solid State Communications* **21,** 757–760 (1977).

215. Painelli, A., Girlando, A. & Pecile, C. Accurate electron-molecular vibration coupling constants from powders optical spectra: TCNQ and TTF. *Solid State Commun.* **52,** 801–806 (1984).

216. Haarer, D. Zero-phonon transitions and vibronic coupling in the 1:1 charge-transfer crystal anthracene-pyromellitic-acid-dianhydride. *Chem. Phys. Lett.* **27,** 91–95 (1974).

217. Bree, a. Vibrational Assignment of Anthracene-d10 from the Fluorescence and Absorption Spectra. *J. Chem. Phys.* **44,** 1788 (1966).

218. Roessler, D. M. Kramers-Kronig analysis of reflection data. *Br. J. Appl. Phys.* **16,** 1119–1123 (1965).

219. Merski, J. & Eckhardt, C. Piezomodulation spectroscopy of molecular crystals. I. Methods and principles. *J. Chem. Phys.* **75,** 3691 (1981).

220. Meneghetti, M. & Pecile, C. Charge–transfer organic crystals: Molecular vibrations and spectroscopic effects of electron–molecular vibration coupling of the strong electron acceptor TCNQF4. *J. Chem. Phys.* **84,** 4149 (1986).

221. Delley, B. From molecules to solids with the DMol3 approach. *J. Chem. Phys.* **113,** 7756 (2000).

222. Delley, B. An all-electron numerical method for solving the local density functional for polyatomic molecules. *J. Chem. Phys.* **92,** 508 (1990).

223. Perdew, J. P. *et al.* Atoms, molecules, solids, and surfaces: Applications of the generalized gradient approximation for exchange and correlation. *Phys. Rev. B* **46,** 6671 (1992).

224. Metzger, R. M. Crystal Coulomb Energies. II. The Electrostatic Binding Energy of Four Organic Donor-Acceptor Crystals by Ewald's Method and Charge Transfer in Organic Lattices. *J. Chem. Phys.* **57,** 1876 (1972).

225. Szczepanski, J., Vala, M., Talbi, D., Parisel, O. & Ellinger, Y. Electronic and vibrational spectra of matrix isolated anthracene radical cations - Experimental and theoretical aspects. **4494,** (1993).

226. Negri, F. & Zgierski, M. Z. On the vibronic structure of the absorption spectra of radical cations of some polycyclic aromatic hydrocarbons. *J. Chem. Phys.* **100,** 1387 (1994).

227. Sánchez-Carrera, R. S. *et al.* Vibronic coupling in the ground and excited states of oligoacene cations. *J. Phys. Chem. B* **110,** 18904–18911 (2006).

228. Herbstein, F. H. & Samson, S. X-ray diffraction study of the disorder-to-order transition at approximately 160 K in the pi-molecular compound pyrene ... pyromellitic dianhydride. *Acta Crystallogr. B.* **50,** 182–191 (1994).

229. Boeyens, J. C. a. & Levendis, D. C. Static disorder in crystals of the anthracene–tetracyanobenzene charge transfer complex. *J. Chem. Phys.* **80,** 2681 (1984).

230. Hoesterey, D. C. & Letson, G. M. The trapping of photocarriers in anthracene by anthraquinone, anthrone, and naphthacene. *J. Phys. Chem. Solids* **24,** 1609–1615 (1963).